Error analysis of the long term Mg II index from SCIAMACHY, GOME and GOME-2

By:

Asher Riaz

Supervisors:

Prof John Burrows

Dr Mark Weber

Acknowledgements

I would like to acknowledge and thank everyone who has directly or indirectly supported me to complete this work. Firstly, I express my gratitude to Prof John Burrows, who showed confidence in me in the first place. I really appreciate the motivation and all valuable advice given time after time. I am thankful for the support, patience and guidance of Dr Mark Weber. His supervision broadened my scientific understanding of solar physics.

I thank Ruediger Lang [EUMETSAT] and Patricia Liebing [IUP, Bremen] for providing GOME-2 and SCIAMACHY data products that were used to enhance the results of this master's thesis. All the technical support provided by Dr Thomas Krings is greatly appreciated. I would like to thank Stefan Botel for all the proofreading.

I am thankful to Dr Faiza Azam for motivating me throughout my stay at IUP, Bremen. She provided me a wonderful opportunity to talk to her in my mother tongue that always gave me a home feeling. I would like to thank all my PEP colleagues especially Sven Krautwurst, Layal Safadi and Syed-ul-haque for being a source of help and assistance. A special thanks to my dearest friend Aimuamwosa Igbinosa, whom I met the very first day when I arrived in Bremen. Ever since every moment shared with him at work or outside is a great memory. I thank him for his kindness, love, care and being a continuous support. I thank Martin Budde, Stefan Botel and Dr Thomas Krings for being such friendly office colleagues. It was a pleasure to work alongside. A special thanks to PEP administration and examination office for everything.

I would like to thank particularly Wissam Chehade and Dr Faiza azam, for the inspiration and motivation. I cannot thank both of them, for the continuous feedback regardless of day and night (specifically last three days of this research project). Their efforts have significantly improved this work.

I thank all my friends that have kept in good contact despite being at distance, especially Aneel Pervaiz (Pakistan), Asif Gulzar (Norway), Sunil Rafique (Pakistan), Arif Nazar (Pakistan), Shalem Sultan (USA), Salman Daniel (Finland) and Milcah Augustine (England). Furthermore I would like to thank Milcah for introducing me to the world of life outside physics. I thank all friends from (my work place) team El-Mundo and the radio activity lab at IUP for their understanding and flexible behavior.

I thank Mr Azhar Syed and his family (Switzerland) for supporting me while I applied for this master's program from Pakistan. My greatest gratitude goes to my old teachers Dr Ronald McCartney (Ireland), Susan Sylvan (USA), Dr Sadia Zaheer (USA) and Dr Monas Shahzad (Pakistan). Without their guidance and support I would have never been able to get this far.

My heartfelt thanks to my grandfather (late) for all the financial support and trusting me that enabled me to come to Germany.

I thank God almighty for being kind to me and enabling me to finish this work. Additionally I thank my family in Germany Mr and Mrs Ilyas Bhatti and my two little sisters for being there for me. I would like to thank my grandmother, my parents, brother and sister for their continuous love and encouragement that always filled my heart with joy and peace.

When I think of my younger sister (my best friend), Komal Riaz (late) it leaves a vacuum in my heart that is hard to be filled or replaced. But one thing which keeps me going is that she always wanted me to study abroad. I dedicate this thesis to her and her presence will be missed as long as I live.

Table Of Contents

Abstract 1

Introduction/Motivation 2

Chapter 1: The sun as a star 4

1.1 The sun 4

1.2 Size and rotation of the sun 4

1.3 Configuration of the sun 5

1.4 Interior of the sun 7

1.5 Core 7

1.6 Radiative zone 9

1.7 Convective zone 10

1.8 Atmosphere of the sun 11

1.9 Photosphere 11

1.10 Chromosphere 12

1.11 Corona (inner and outer corona) 13

Chapter 2: Solar activity 15

2.1 Sunspots 15

2.2 Sunspot solar cycle 16

2.3 Solar irradiance and sunspots 18

2.4 Solar spectrum 20

2.5 Solar activity UV emissions & the stratosphere 21

2.6 Latest solar cycle and prediction techniques 21

Chapter 3: Mg II index and error estimation 25

3.1 Importance of Fraunhofer lines 25

3.2 Mg and Mg II (Magnesium Doublet) 27

3.3 Mg II Index 28

3.4 Other solar proxies 31

3.4.1 Lyman alpha 31

3.4.2 Daily sunspots 32

3.4.3 The F10.7 cm solar flux 32

3.5 Error analysis 32
3.5.1 Accuracy and Precision 33
3.5.2 Systematic and Random errors and Gaussian distribution 34
3.6 Errors caused by optical degradation 35
3.7 Errors and Signal to Noise ratio [SNR] 36
Chapter 4: The Instruments 39
4.1 GOME on ERS-2 39
4.1.1 Solar measurements by GOME 40
4..1.2 Sun diffuser and degradation 41
4.2 SCIAMACHY on ENVISAT 41
4.2.1 ENIVSAT 41
4.2.2 SCIAMACHY 41
4.2.3 Schematic & observational modes of SCIAMACHY 42
4.2.4 Sun observations and M-Factor 42
4.3 GOME -2 on MetOp 43
Chapter 5: The Scientific Method 44
5.1 Overview 45
5.2 Solar spectral irradiance calibrations and corrections 46
5.2.1 Solar spectrum calibrations 47
5.2.2 Degradation correction 47
5.2.3 Etalon correction 48
5.3 Retrievals of Mg II index 49
5.4 Error model for the Mg II index 53
Chapter 6: Results 57
6.1 Mg II index, solar proxies and filtering 57
6.2 Mg II index from GOME, SCIAMACHY and GOME-2 61
6.3 Degradation rate of GOME, SCIAMACHY and GOME -2 63
6.4 Simple error model applied to Mg II index 65
6.5 Validation of GOME-2 results 70
Chapter 7: Conclusions and Outlook 57
7.1 Summary and Discusions 72
7.2 Outlook 73

Reference:…… 79

Abstract

The Mg II index is a (core to wing) ratio of the chromspheric emission core at 280 nm to the wing absorption of the photospheric radiation [Viereck et al., 2004]. The Mg II index is a commonly used proxy of solar variability owing to the fact that it is just one number and simple to measure. It also correlates very well with the spectral solar irradiance at many ultra-violet (UV) wavelengths. This proxy, composed of many satellite data-sets; has a long record reaching back to the late 1970s. Furthermore, it is not possible to have a consolidated long term record of the solar spectrum available at all wavelengths since the satellite instruments are sparse in time and wavelength coverage from extreme UV to near infrared (NIR) . The objective of this study is to determine the errors for the daily Mg II indices of the satellite instruments SCanning Imaging Absorption spectroMeter for Atmospheric CHartographY, “SCIAMACHY”, Global Ozone Monitoring Experiment, “GOME” and Global Ozone Monitoring Experiment-2, “GOME-2”. This work is the very first attempt to provide an error estimation of the Mg II indices for the above mentioned instruments. We provide the error analysis by taking into account the optical degradation of the instrument over time. Such errors enable us to estimate the uncertainties caused by the degradation of the instrument due to exposure to the harmful radiation in space. The simple error calculation model built in this study uses the error propagation technique. The model is applied on the datasets from GOME for the time span 1995-2011, SCIAMACHY for 2002-2012 and GOME-2 from 2007 till present. The calculated errors for all the three instruments are not constant but vary over time (magnitude of the errors increase as sensor ages). These results have enabled us to provide an estimate of the long term stability of the Mg II index time series.

Introduction/Motivation

In the early 17th century; scientists opened a new phase of our understanding of the sun, by establishing the telescope. The telescopes were the first authentic source providing the existence of sunspots on the sun's surface (although the sunspots were known before the 17th century they had no convincing source to claim it). This discovery brought a revolution, it was learnt that the sun is a rotating variable star, which exhibiting a periodic 11 years cycle in its activity. This raised another question, "Is there any relationship between the solar terrestrial climate and the solar cycle?" Many theories were presented, predictions about the sun mostly proved to be inaccurate.

When the satellite era began, the scientists realized that our understanding of the sun is not complete enough to forecast. The sun was monitored from space, on a time scale of minutes to decades, at almost all emission wavelengths of the sun and different solar proxies were derived for the solar variability. A clearer picture of the sun was put forward and the understanding about the sun improved. As the basic physical processes on the sun's surface were observed i.e., luminance, solar magnetism, solar flares, solar plages, sunspots, sun controlled solar winds and many other parameters, their systematic studies on a long term basis began.

An important solar parameter, the total solar irradiance, has been measured from several satellite missions dating back to late 1970s. The 11 year solar cycle and the solar variability have been studied. The effect of the solar variability on the earth's climate has been investigated.

The solar radiation traverses the space and reaches our atmosphere [Viereck et al., 2004]. 30% of the solar radiation is reflected back to space, mainly by clouds (20%), by atmosphere (6%) and by the earth's surface (4%), the remaining 70% is absorbed, specifically by the earth's surface (50%), the atmospheric constituents (e.g. ozone and green house gases) (16%) and by clouds (4%). Earth absorbs the shortwave radiations and re-emits them back to space as long wave (thermal infrared) radiations. Ozone, in the stratosphere, is the main absorber of the short wave radiation ($\lambda \leq 310$ nm). The green house gases absorb the infrared radiation emitted by the surface. The radiative balance of the earth's atmosphere has been disturbed by manmade activities leading to global warming. The solar variability influences the global ozone production which shields the earth from the biologically harmful UV radiation, total ozone changes by 2-3% during a solar cycle [World Meteorological Organization, WMO, 1999]. It has been observed that when the sun activity reaches its maximum, the ozone production dominates ozone destruction [Dikty et al., 2010]. Long term as well as short term variations in the earth's climate, e.g. temperature variations in the stratosphere, ozone depletion and production, the green house effect, cloud formation over the pacific ocean, response of phytoplankton to UV radiations (uptake and release of carbon dioxide) etc. have been linked to the solar activity [Benestad, 2002].

Heath and Schlesinger (1986) suggested a unique index of solar UV activity called the Mg II index and defined it as the core to wing ratio of the unresolved h and k absorption feature in the emission core of ionized Mg at 279.9 nm. The Mg II absorption is overlaid by a narrow doublet line of emissions that actually evaluate the UV flux variations of the sun's chromosphere. Variability of the sun's spectrum can be observed from short to long time scales (from days to decades) e.g. 9, 13.5, and 27 days (sun's rotational period) and 11 years (solar cycle), respectively. The pivotal importance of Mg II index lies in its ability to reconstruct the solar spectral irradiance (SSI). The advantage of the Mg II index over other indices is that it is a ratio of irradiances which cancels out attenuation in the received signal over time. As the instrument ages, the Mg II index gets unstable. This instability is caused by the optical degradation. Degradation is a phenomena bound to happen on the sun observing instruments exposed to the solar radiation. By taking optical degradation of the instrument in account; this thesis presents a first attempt of the error calculations of the Mg II indices from SCanning Imaging Absorption spectroMeter for Atmospheric CHartograpHY “SCIAMACHY”, Global Ozone Monitoring Experiment “GOME” and Global Ozone Monitoring Experiment-2 “GOME-2”.

Chapter 1: The sun as a star

1.1 The sun

The sun is the nearest star to the earth, located at a distance of 93 million miles. It takes 8 minutes 20 seconds for the solar radiation to travel from the sun's surface through space to the earth. The sun is mainly made up of plasma.

The stars are classified as O, B, A, F, G, K to M on the basis of their temperature, where “O” is the highest temperature and “M” being lowest respectively. Numerical numbers are assigned to these classes e.g., G2, indicating a further subdivision based on size. Among a host of 100 billion other stars, the sun is categorized as a G2 star [see Benestad, 2002 for details].

1.2 Size and rotation of the sun

The mass of the sun is about 1.989×10^{30}kg. Compared to the earth's mass of 5.897×10^{24}kg, it is 332,900 times as massive as the earth. The sun contains around 99% of the mass of our solar system [Tapia, 2005]. The sun is 4.6 billion years old and it is believed to live for 5 more billion years. As the sun is getting older, its mass decreases due to fusion reactions taking place in the core that convert hydrogen to helium and release energy. The reduction in mass is fairly small and could only be observed over millions of years.

The diameter of the sun is 1.39×10^{9}m, the earth's diameter is 109 times smaller and the volume of the sun is 1,299,400 times the volume of our earth [Zell, 2012].

The sun is made up of self gravitating plasma which pulls itself together and gradually spins up. The plasma does not have a regular magnetic field. Instead, it has a very complex and twisted magnetic structure. The magnetic field of the sun is therefore a tangled web where each magnetic structure has its own North and South Pole unlike the earth which has only two magnetic poles. Moreover, the sun has a differential rotation which gives rise to an even more complex magnetic field.

Figure 1.1 [Zell, 2012], illustrates the differential rotation of the sun. The equator of the sun moves faster than the poles. At 0° latitude, the sun rotates around in 25.6 days while close to equatorial regions it rotates around in 26 days. At about 60° latitude, this rotation around its own axis has a period 31 days and at the poles, it takes 35 days. The sun rotates counterclockwise as the earth does whereas it's tilt is 7.25°. Generally, the solar rotational period is taken to be 27 days. The sun orbits around the Milky Way galaxy and it takes 230 billion years to complete a revolution around our home galaxy [Zell, 2012].

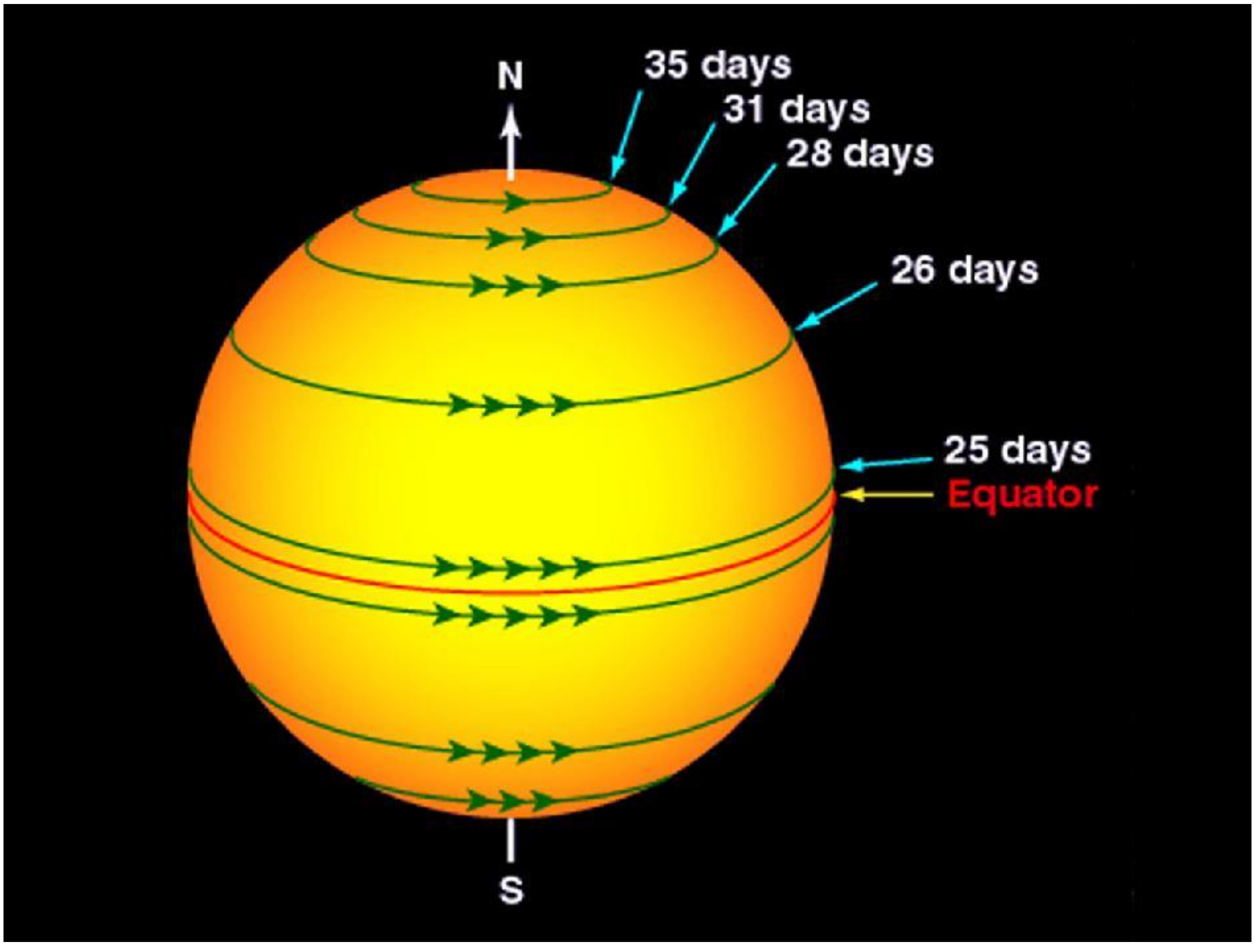

Figure 1.1: An illustration of the sun's differential rotation [Zell, 2012].

1.3 Configuration of the sun

As stated earlier, the solar material is composed of plasma. The plasma contains positive and negative ions, charged particles and electrons. Plasma is a peerless conductor because of the excess of free charges. According to the electromagnetic theory, conductors do not possess a steady electric field since the charges cancel each other's effect [Benestad, 2002]. The sun's plasma does not hold an electric field. Nevertheless, the magnetic field of the sun is a consequence of an electric current present in the solar interior. A pronounced feature of the sun is its magnetic field. The sun's configuration mainly consists of three parts (Fig. 1.2) [Barnes, 2006].

- Interior of the sun including the core, radiative zone and convective layer
- Atmosphere of the sun including the photosphere and chromosphere
- The inner and outer corona

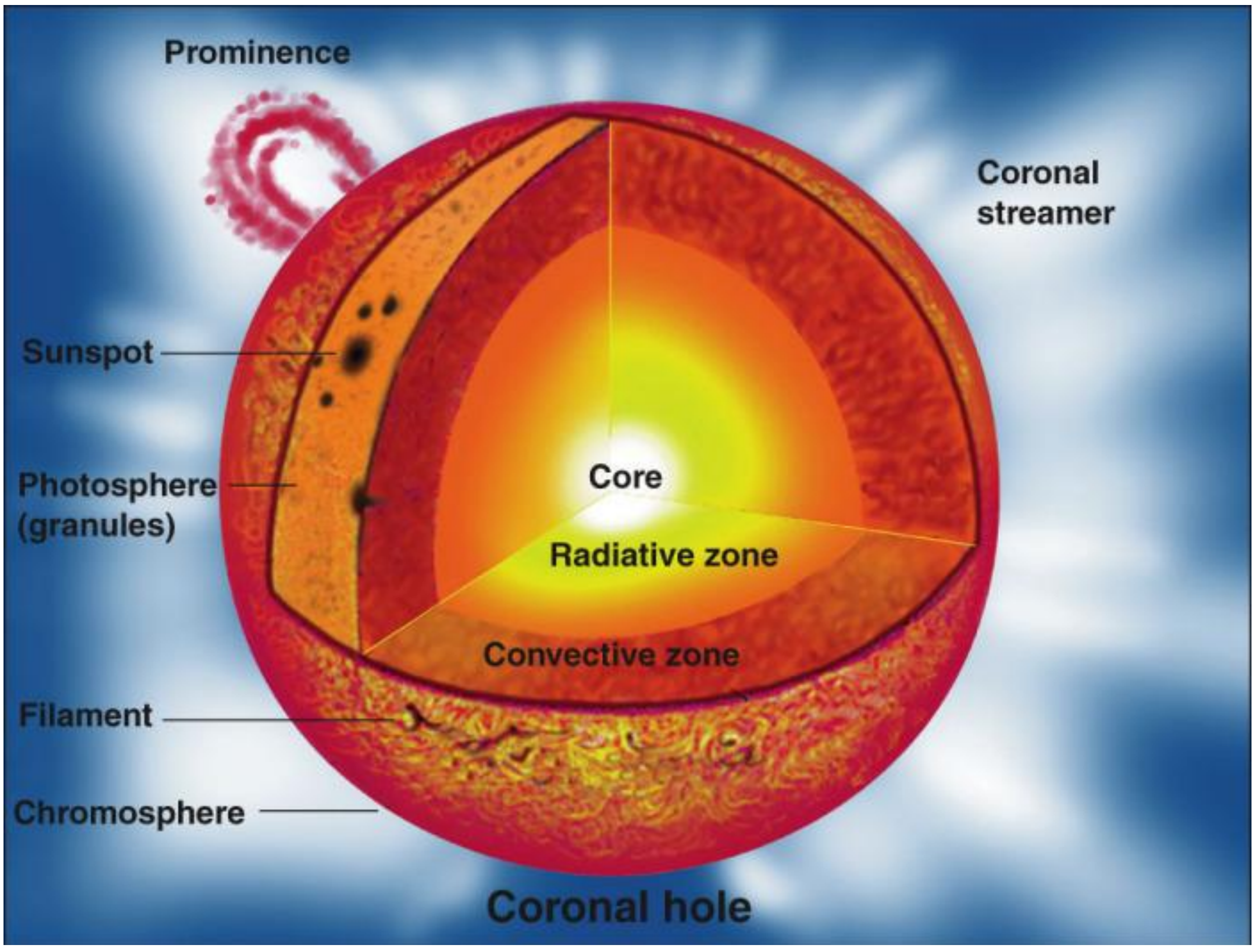

Figure 1.2: Different parts of the sun [Barnes, 2006]

1.4 Interior of the sun

The sun is is mainly made up of hydrogen (71.0%) and helium (27.1%). About 98.1% of the sun's total mass is the sum of these two elements with the remaining 1.9% being made up of Oxygen (0.97%), Carbon (0.40%), Nitrogen (0.096%), Silicon (0.099%), Magnesium (0.076%), Neon (0.058%), Iron (0.014%) and others (0.040%) [Benestad, 2002]. The conversion of hydrogen to helium fuels the sun. At present the sun has 5 more billion year's worth of fuel, after that it will run out of hydrogen [Liou, 2002].

The interior of the sun starts at the core, extends to the radiative zone and ends at the convective layer. These three components constitute almost 99% of the sun's volume. These regions are characterized by very high temperatures and pressures and are responsible for the production and transport of energy. The environment in the interior of the sun is ideal for a nuclear fusion. Two hydrogen atoms fuse together, to form helium (a heavier element) and energy. Mass is converted to energy; E = mc^2 , where E = energy, m = mass and c = speed of light per second.

In the sun's core, about 700 million tons of H_2 are being fused to 695 million tons of He and the rate of conversion of mass to energy is 5 million tons of mass per second.

1.5 Core

The inner 25% of the sun's radius is considered the core. This part is of extreme importance as in this region most of the energy production takes place. Temperatures here are of the order of millions of Kelvin (1.56×10^7K) [Liou, 2002], the corresponding pressure is 2.5×10^{11} atm. It has a density of 150 g/cm³ which is 8 times the density of gold. At such high density, it should be solid. But, very high temperatures transform it into plasma creating a perfect environment for the thermonuclear energy production [Barnes, 2006]. The high temperature, pressure and density compel protons to overcome their electric repulsion and fuse to form heavier elements and emit energy as gamma rays.

Figure 1.3 [Jefferson, 2011] illustrates the nuclear fusion taking place at the sun's core. The reaction takes place in three steps.

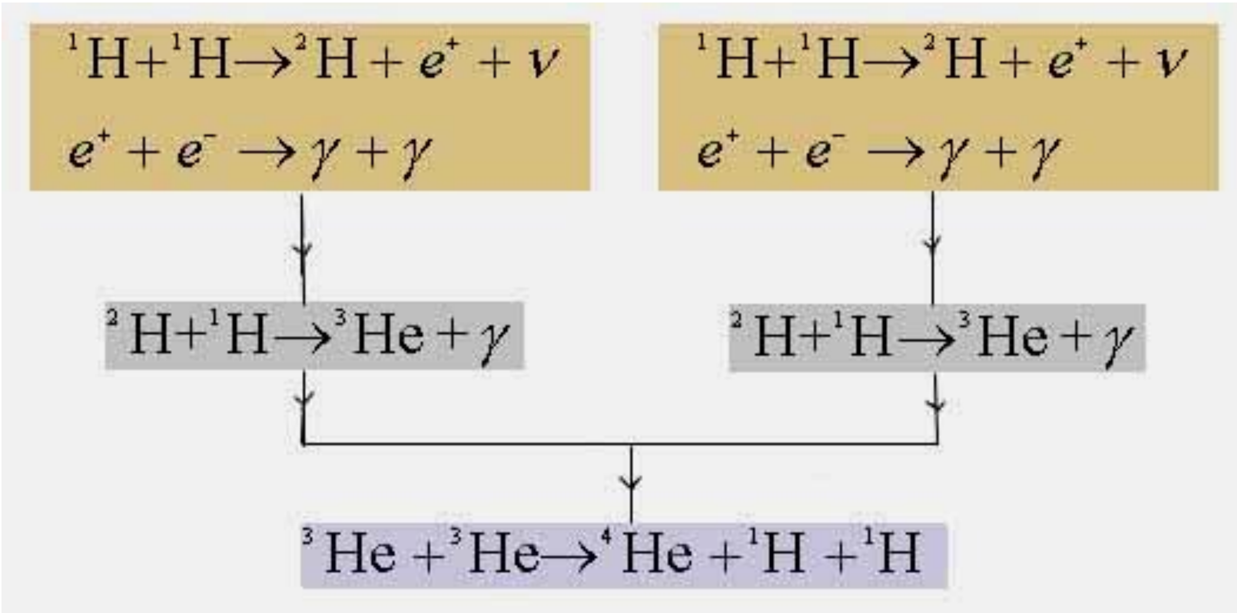

Figure1. 3: Fusion reaction in the sun's core [Jefferson, 2011]

First, the formation of deuteron [^{2}H] takes place by the reaction two protons of hydrogen [^{1}H] + [^{1}H] which collide thermally. In this step, a positron [e^+] and a neutrino [ν] is also produced. The positron reacts with an electron and annihilates into two gamma [γ] rays photons. Energy is produced in the first step.

In the second step, the deuteron [^{2}H] produced in the previous step collides thermally with a proton [^{1}H] and fuses to form [^{3}He] Helium-3 emitting a gamma ray [γ]. Energy is produced again [Jefferson, 2011].

In the third and final step of the chain, the helium-3 takes tens of thousands of years to find another Helium-3 to eventually fuse into helium-4. This final step gives away two hydrogen protons as well.

This multistep reaction behind the sun's fusion cycle is responsible for the releases of power of about 3.9×10^{26} W.

Overall, the reaction can be summarized as follows.

$4(^1H) + 2(e^-) \rightarrow {}^4He + 6(\gamma) + 2(\nu)$ --- (1)

This over all reaction gives off 26.7 MeV of energy and is accountable for 85% of the total nuclear fusion happening in the sun's core. The remaining 15% can be attributed mainly to the formation of berilium-7 and lithium-7, see the reaction chain in Fig. 1.4 [Zabludoff, 2011] showing the possibilities of nuclear fusion that could happen in the sun's core.

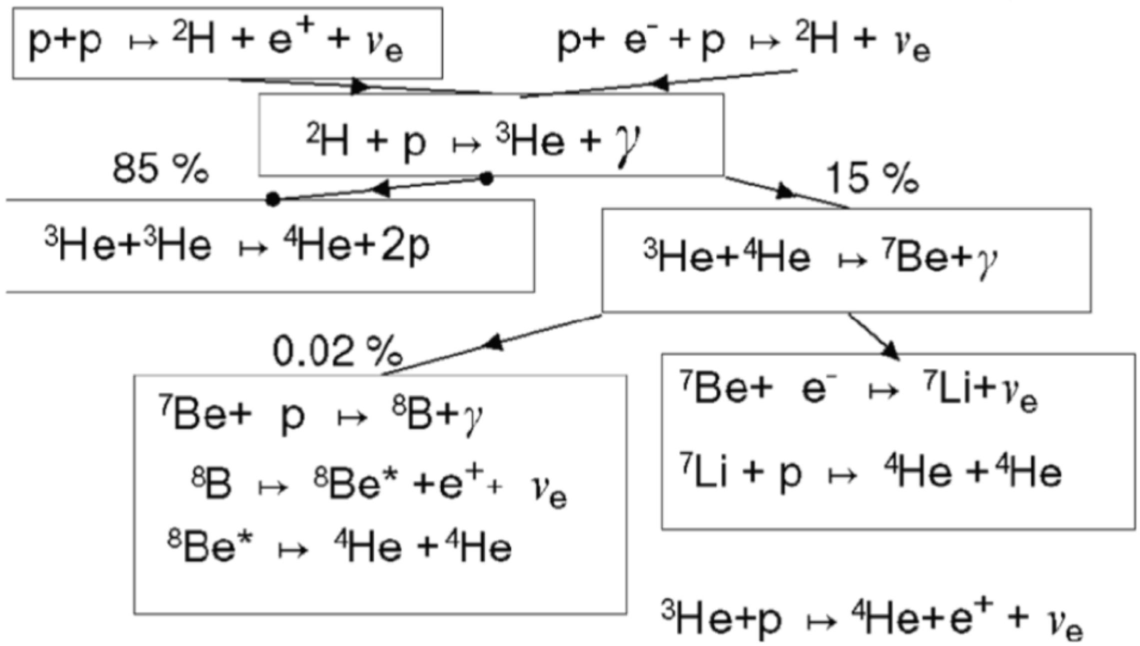

Figure 1.4: Fusion possibilites in the sun's core [Zabludoff, 2011]

1.6 Radiative zone

The radiation zone stretches out of the core of the sun (0.25 of the solar radius) to the convection zone (0.70 of the solar radius). This part contributes to 45% of the sun's total radius and to around 32.7% of the sun's volume. This section is responsible for the transport of radiation. Energy created in the core gets absorbed in this region and is re-emitted many times. Around 10^{25} absorptions and re-emission happen before a photon can reach the surface. Though, photons move at the speed of light, the extremely high density at the core influences the motion of individual photons which consequently exhibit a random motion. As a result, it takes them millions of years to escape through the core and reach the radiative zone. The density falls, dramatically from 150 g/cm³ to 0.2 g/cm³ (less than the density of water), decreasing all the way to the top of the radiative zone. Figure 1.5 depicts the density profile for different regions of the sun [Hathaway, 2012].

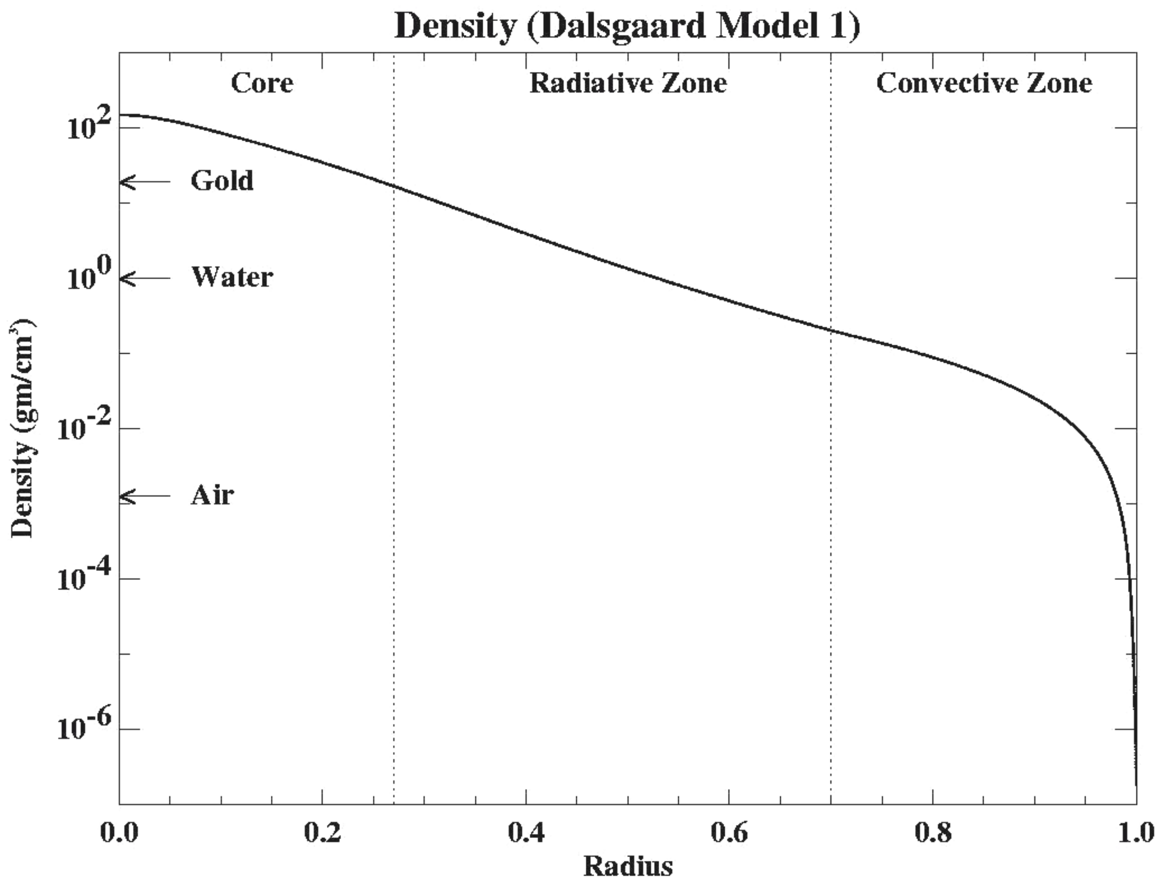

Figure 1.5: Density profile of the sun's interior [Hathaway, 2012]

1.7 Convective zone

The convective zone is the external portion of the sun's interior. Here, the energy is transported by convection. This region comprises the outer 30% of the sun's radius. Here, the temperature is less and the density is smaller compared to the inner zones. At the surface of this zone, the density is 2×10^{-7}gm/cm³, which is 1/10,000th of the density of air at sea level. The density rapidly decreases from core to convective zone. The cooler temperature and low density allows heavier ions of carbon, nitrogen, iron and calcium to have a hold on their electrons. These conditions make this region opaque, which is very resistive to let the radiation passing through. The hot solar material at the bottom of the convection zone (or at the top of the radiation zone) travels upwards and cooler material consequently descends. Hot material reaches the surface, loses its energy, cools down and sinks continuing the cycle. These vertical convective cells are fast heat carriers. It just takes one and a half weeks to carry energy to the surface (the features that support these cells are; low density and sudden drop in temperature). As the convection current establishes itself in the convective zone, granulation happens which is a visible boiling effect on the surface [Benestad, 2002].

1.8 Atmosphere of the sun

The atmosphere of the sun is located above the convective zone. Like the earth, the sun also has an atmosphere. It has many unique features which are observable from our home planet, e.g., sunspots, granules, super-granules sunspot pores, bright faculae, large scale flows, solar flares, post-flare loops. The atmosphere of the sun can be divided into three further sub-classes:

- Photosphere
- Chromosphere
- Corona

Corona will be discussed as an individual branch.

1.9 Photosphere

The photosphere is a well known segment of the sun. The reason is that we can see this portion (luminous visible surface), directly from the earth. Energy or light we receive on earth mainly comes from the photosphere. The photosphere contains sunspots (regions with strong magnetic fields), granules, faculae etc. It is the coolest part of the sun; with a mean temperature of about 5770 K (the number mostly agreed upon in the scientific community). Such a low temperature is the reason why only 0.1% of gas exists here in plasma state.

This portion of the sun is almost 100 km in depth below the chromosphere. The density reaches up to 2×10^{-7} gm/cm³. The temperature of the photosphere can be derived assuming the properties of a black body, this character is very important regarding the solar spectral irradiance. The sun does not only radiate energy in the visible region; but also in different wavelength ranges, which directly or indirectly affect our climate. Consequently, it is essential to observe the solar emission spectrum and a good understanding of the processes in the photosphere is essential.

1.10 Chromosphere

The chromosphere is the layer of the sun above the photosphere. This region is not as bright as the photosphere, has a high temperature (20,000 K), and is less dense than the photosphere. At such high temperatures hydrogen starts emitting reddish light which is called the "H-alpha emission". Owing to this reason, it is called the chromo-sphere, meaning color-sphere. During a total solar eclipse, when the moon passes between the earth and the sun and blocks the light coming from the photosphere, colorful light emissions can be observed as prominences (suspended material like dense clouds on top of the surface of the sun). Chromospheric features include filaments, plage, spicules, chromospheric network and prominences [Morsink, 2011]. Figure 1.6 [Morsink, 2011] shows highlights the prominences and a solar eclipse.

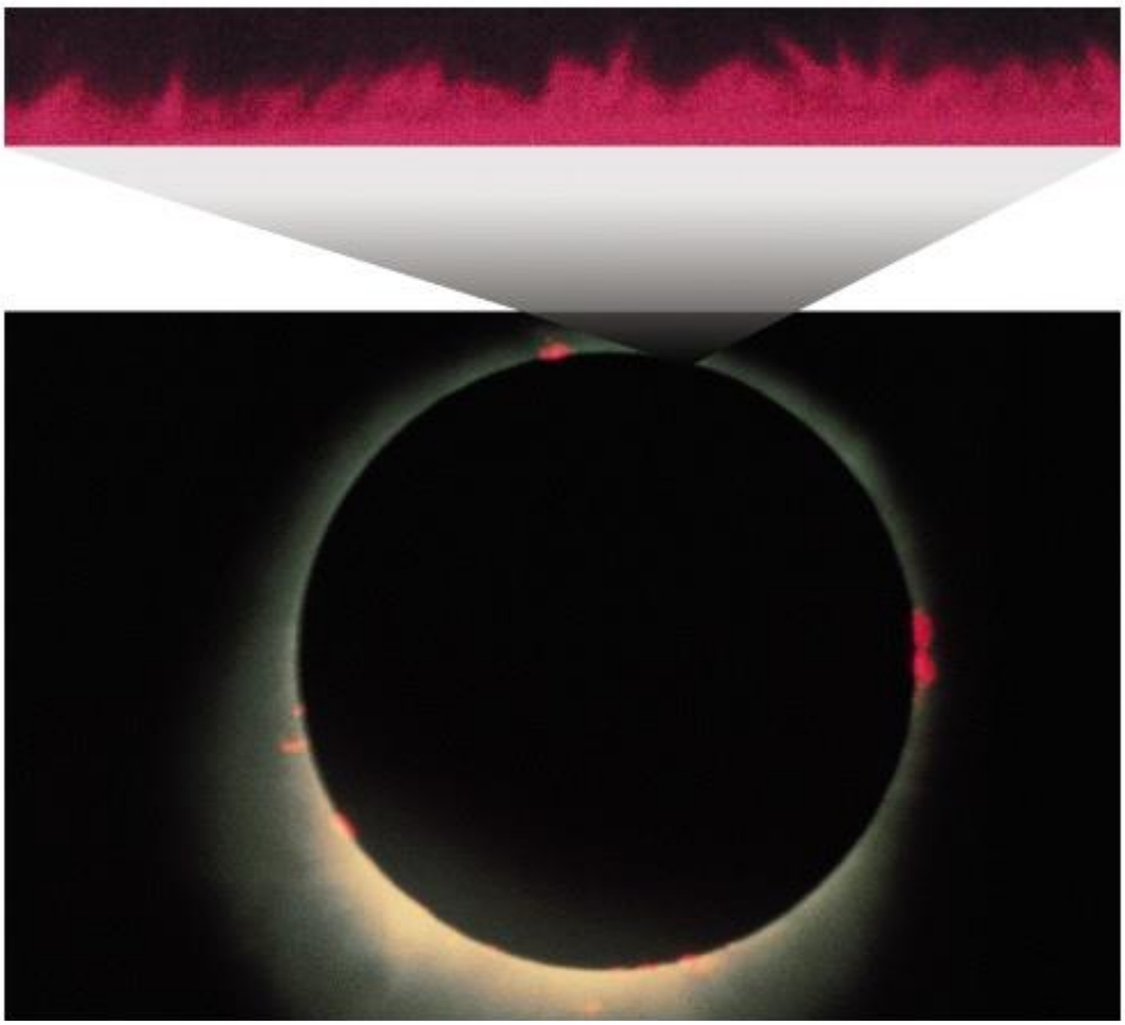

Figure1. 6: Solar prominence during solar eclipse [Morsink, 2011]

1.11 Corona (inner and outer corona)

The outermost region of the sun's atmosphere is called corona. It can be further subdivided into inner corona and outer corona (the outer corona is the outer most part of the exterior of the sun, stretching to our earth and even beyond). This region is also visible during a total solar eclipse as shown in Fig. 1.7 [Morsink, 2011]:

Figure 1.7: Solar corona during solar eclipse [Morsink, 2011]

This layer extends millions of kilometers into the space. It has a higher temperature but less density compared to the photosphere and chromosphere. The temperature can get as high as 10^6 K. The very high temperature causes the x-rays emissions. The important details about the corona can only be observed in the x-ray part of the spectrum. The reason of coronal heating is not very well understood until now. As we move away from the heat source, temperature decreases, according to the second law of thermodynamics. The heating in this region does not follow this law, as corona is far away from the core and has a temperature up to millions of Kelvin. A number of theories are presented to explain the reason of coronal heating (extremely high temperatures). Two of them, ion-cyclotron waves and micro-flare, are well agreed upon and known commonly.

The appearance of corona changes as the sunspot 11 year solar cycle changes. It appears very bright as the sun cycle approaches its maximum activity, and can appear dim as activity becomes minimum. The features that are observed as dark regions, because of their relatively lower density are termed coronal holes. They are mostly found at the poles of the sun and are characterized by open magnetic fields (when a magnetic line of force stretches so far that, before coming back it approaches earth-sun system, is called open). The streams of charged particles (electrons and protons) coming out of these coronal holes give rise to solar winds. Their presence can be seen at North and South Pole of the earth as these winds interact with the earth magnetic field and cause “auroras”. Earth’s magnetosphere is not strong enough to resist the solar winds. Solar particles move along the earth’s magnetic field lines, concentrate in the polar regions and excite the constituents of the earth’s atmosphere whose de-excitation results in the emission of light (aurora).

Features of the corona are polar plumes, coronal loops, helmet streamers, solar winds and coronal mass ejections (CMEs). CMEs are the gigantic bubbles of gas surrounded by very strong magnetic fields. They are produced from the sun’s corona on the time scales of few hours. These ejections are mostly associated to the prominence and solar flares, which can sometimes also happen in their absence. These eruptions contain super heated plasma moving at a speed of 1300 to 1450 kilometers per second and contain enormous amount of material. If it is ejected in the direction of earth, it can be of danger to our planet. Such a big super heated mass, approaching our home planet at such a high speed (could take 16 hours to reach earth) can have serious consequences. It can damage our satellites, destroy our earth’s magnetic field and create extremely bright auroras. It can cause health hazards (strong radiations) to the passengers travelling in airplanes close to the poles. It can also interact with the magnetic field of our power stations and destroy them. CMEs cannot be predicted. We can only monitor the sun and alert the people to minimize the destruction, if the CMEs are approaching the earth [Morsink, 2011].

Chapter 2: Solar activity

Solar activity is the result of the fluctuating solar magnetic field. Solar activity and magnetism of the sun are two connected terms leading the existence of the “sunspots”. Sunspots are photospheric features which are accompanied by prominences, plages, granules, faculae, spicules, chromospheric networks etc. this means that the solar activity is also deeply connected to the chromospheric features. The solar activity can cause solar flares, CMEs (coronal mass ejections), solar winds etc affecting the climate of the earth [Schmitt, 2004].

2.1 Sunspots

Sunspots are regions in the photosphere with dark appearances associated to a very strong magnetic field and are comparatively cooler than the photosphere. The dark regions characterize the central part of the sunspot known as “umbra” where as the outer part of the core is less dark known as “penumbra” as shown in Fig. 2.1 [NASA, 2012]. Generally the diameter of the umbra ranges between 10,000 km to 20,000 km (the largest sunspots can have an umbra with a diameter of up to 50,000 km). A sunspot (penumbra plus umbra) can reach a radius of 20,000 km and 35,000 km [Barnes, 2006].

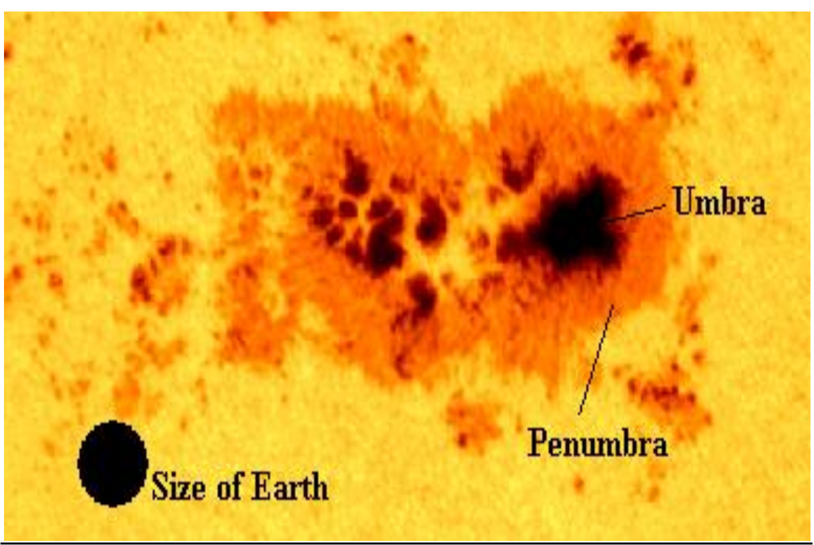

Figure 2. 1: Sunspot along with umbra and penumbra [NASA, 2012]

Sunspots originate as sunspot pores, which later develop penumbral structures around themselves and get bigger to reach their final form. Conversely, when a sunspot is small enough and its penumbral structure is negligibly small, with a diameter smaller than 2500 km, it is no longer a sunspot but rather a sun pore. Pores are associated with a weak magnetic field in comparison to the sunspots. Most of the time, sun pores exist in groups, but sometimes isolated structures of pores are observed. They have life times of a few hours up to several days. On the solar disk, sunspots appear in groups most of the time, and within a group, every sunspot has the same magnetic field structure. The strongest part of the magnetic field is affiliated with the umbra where weaker fields are observed in the outer part of the sunspot i.e. penumbra [Barnes, 2006].

Hale was the first Solar Physicist who found that sunspots are cooler than the photosphere. He studied the solar spectra using a photographic technique and discovered that in contrast to the normal photosphere, the sunspots have low intensity line spectra. The temperature of the photosphere is measured to be 5770 K and from reliable measurements (from different satellite missions) sunspots have temperatures in the range of 3000 to 4000 K [Liou, 2002].

The cooling of the sunspots can be explained on the basis of magnetic theory. The magnetic field emerges as a result of inconsistent or fluctuating motion of the rotating fluid (plasma). The differential motion of the plasma near the solar surface incites turbulent convection. The convection is mobilized by heating from below i.e. the convective zone. The rotating fluid twists the magnetic fields many times in such a way that a gigantic web of magnetic lines of forces bursts out from the surface of the sun. This contains a large number of North and South Poles. The resultant turbulent convection reduces the transfer of radial energy that is responsible for the sunspot heating. With the drop in the radial energy, the temperature of the sunspots is reduced [Benestad, 2002].

As discussed in the previous section (convective zone), granules come into existence as a result of convection. Convection cells bring hot solar material upwards, giving off energy, consequently cooling and sinking down. The sunspots suppress the granules. Observations have shown weak granules inside the sunspot. However convection cannot be suppressed fully. It is concluded in different studies that the suppression of convection can explain the low temperatures of sunspots [NASA, 2012].

2.2 Sunspot solar cycle

Schwabe observed the periodicity of the sunspots over time and discovered after prolonged observations that the number of the sunspots exhibit a continuous cycle of maxima and minima (sometimes, even no sun spot). He explained that over a period of 11 years the number of sunspots fluctuates. This number could reach up to 254 (as observed on October 1957) during the maximum and occasionally no sunspots could be witnessed over the minimum of the solar activity. Hence to honor the discovery of this 11 years sun cycle it is called the "Schwabe cycle" [Benestad, 2002].

According to the latest results, the scientific community agrees that the Schwabe solar cycle is not fixed to 11 years, but can fluctuate between 10 and 12 years. During the 11 year cycle sunspots are most likely to appear in the spot zone (±35° from the equator). There are times when sunspots have been traced at 75°, but this is not usually the case. The sunspot cycle generally is initiated with a small number of the sunspots near 30° latitude. As the solar activity proceeds, they move closer and closer to the equator and have been reported at latitudes of ±15°. Before the cycle ends, sunspots move even closer to the equator (±8°).

On the surface of the sun, the sunspots are observed above or below the equator. Sunspots in both hemispheres have a different polarity i.e. the northern set of sunspots may generate a positive magnetic field, while the southern hemispheres sunspots have a negative magnetic field. This phenomenon is reversed after each solar cycle, meaning that in the next cycle the positive magnetic field will become negative and vice versa. This is the reason why it is called the 22 year cycle. Every 22 years, the magnetic field returns back to its original polarity in the respective hemisphere. Another aspect is that the number of the sunspots is not necessarily identical in both hemispheres. Most of the time, one hemisphere of the sun will have more sunspots than the other hemisphere, hence the one with more sunspots will be the more active region during the solar cycle [Barnes, 2006].

Counting the number of sunspots is not as straightforward as it may seem. To be able to count sunspots we need a telescope by which one can observe the sun's surface. Sunspots often appear in groups. To count the number of sunspots, one has to first count the number of the sunspot groups and later the number of exclusive sunspots. The formula, first introduced by Rudolph Wolf (1848), to count the number of sunspots is given below:

$$\mathrm{R} = \mathrm{k}(10\mathrm{g} + \mathrm{s})$$

Where R is the sunspot number, k denotes the scaling factor (most of the time less than 1), g is the number associated to sunspot group number and s, the number of individual sunspots [Naoj, 2012].

Generally every sunspot group contributes to approximately 10 sunspots. The formula works reliably even when it is hard to decide whether smaller sunspots should be counted as sun pores or sunspots. Figure 2.2 [Naoj, 2012] depicts the sunspot number time series 11 solar cycles for the last 80 years.

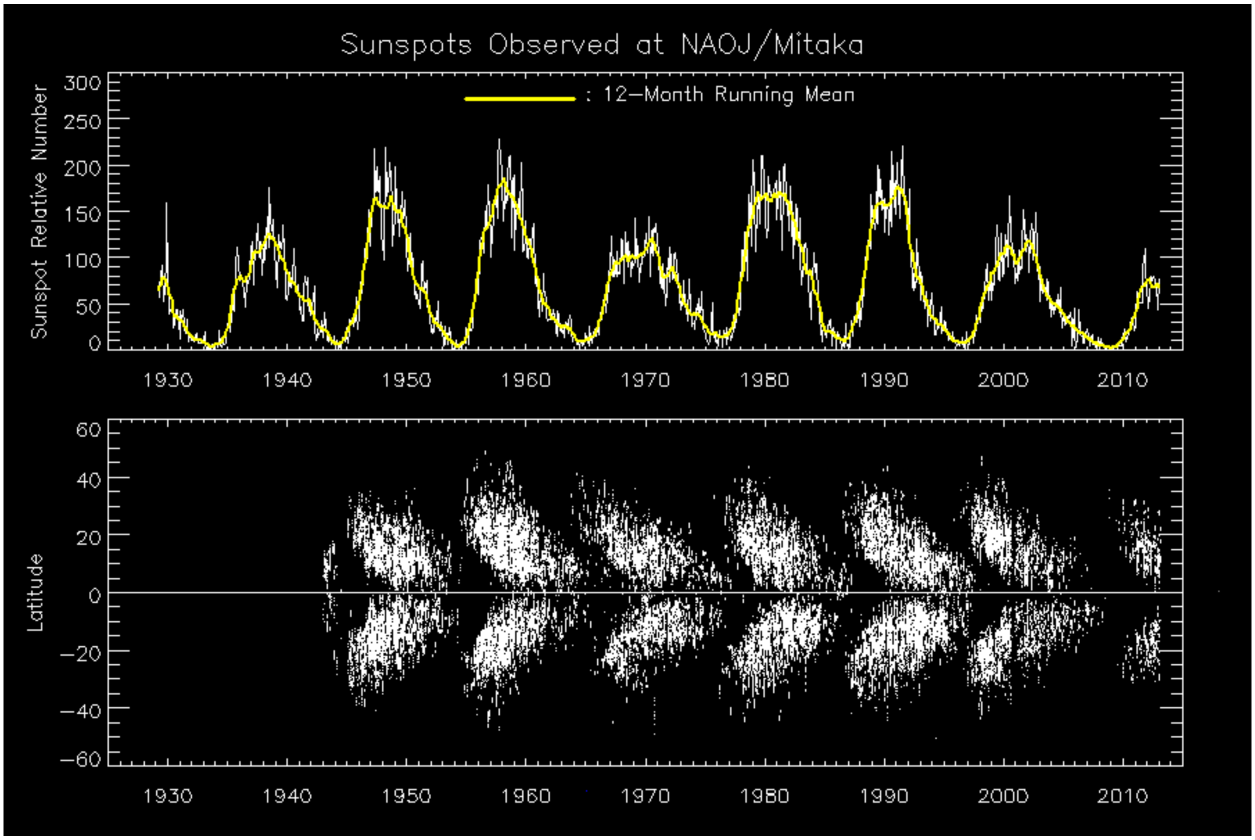

Figure 2. 2: Time series of sunspot numbers from the last 80 years(upper panel) and the Sunspot appearing at different latitudes forming butterfly diagram (lower panel)[Naoj, 2012]

The upper panel of Fig 2.2 presents time series of the sunspot numbers. It is obvious that every cycle has different amplitude and on a closer look one can see that the time period for every solar cycle varies. The lower panel shows the time series of occurrence of the sunspots at different latitudes. It can be seen that during the sun's 11 year cycle most of the sunspots appear close to the equator and up to latitudes of ±60°. The highest density is at ±30°. As the activity goes down, they get dissolved. Due to its shape this time series is often called a butterfly diagram [Naoj, 2012].

2.3 Solar irradiance and sunspots

The solar cycle corresponds to a periodic variation of the sun spots. Periods of low and high solar activity correspond to low and high sunspot numbers respectively. Observations have shown that the luminosity of the sun correlates with the 11-year solar cycle. This leads to a corresponding rise and fall of the total solar irradiance 'TSI' (the total amount of the sun radiant energy integrated over the entire wavelength range, reaching earth's atmosphere per second) [IPCC, 2007].

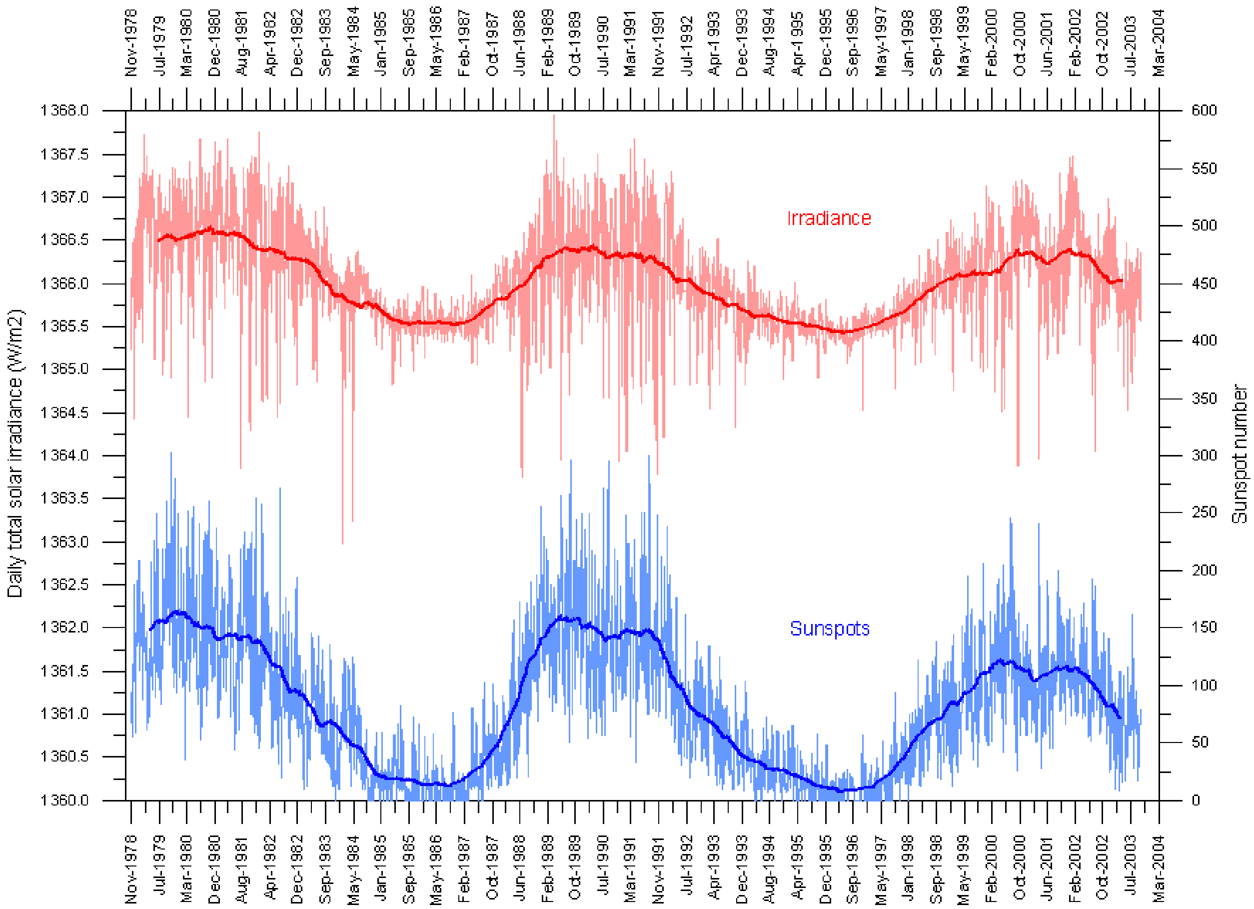

Figure 2. 3: Solar irradiance correlation with the sunspots [Humlum, 2007]

Figure 2.3 [Humlum, 2007] depicts the correlation of the solar radiation with the sun spots. The daily irradiance is plotted in red and the sunspot numbers in blue. The thick lines for both measurements show the annual mean. A correlation between the sunspots and total solar irradiance can be clearly observed.

As the sunspots are the regions that appear dark in comparison to the surroundings, it could be expected that as more sunspots appear on the solar disk; it would get darker and the luminosity of the sun decreases [Pagaran, 2011].

The sunspots are photospheric features. Due to the magnetic lines extending upwards (above sunspots) the above lying chromosphere gets heated (plages, faculae) and they cause brightening (mainly in the UV). This increase corresponds to 0.1% (1.3 W/m^2) of the solar constant S = 1367 W/m^2[Humlum, 2007].

2.4 Solar spectrum

The solar spectrum is similar to that of the black body (perfect absorber and emitter) at a temperature of 5770 K. The sun is an emitter of electromagnetic radiation. The solar electromagnetic spectrum comprises of many different wavelengths. Starting from gamma rays (10^{-5} to 10^{-3} nm), x-rays (10^{-3} to 10^{-1} nm), UV (100-400 nm), visible from violet to red (400-700 nm), near Infrared (780 nm-3 µm), far infrared (3 µm-50µm) and radio waves (up to 100m) [Rieke, 2010].

Figure 2.4 [Lean, 2010] shows the solar spectral irradiance (which provides the TSI or solar constant by integration over all wavelengths) in dark blue, the variability over an 11 year solar cycle in green, and the atmospheric absorption in light blue [Lean, 2010]. Also shown, is the black body spectrum at 5770 K in red. The solar spectrum shown here is measured at the top of atmosphere. Spectral irradiance and the scaled black body curve are in a good agreement (note that the black body curve has been scaled according to the distance of the earth from the sun, the factor is the solar radius squared divided by 1 AU). The light blue curve shows the solar spectrum at sea level, meaning after passing through the earth's atmosphere.

Different absorption bands can be seen. These bands are due to absorption at different wavelengths by the atmospheric constituents like nitrogen, oxygen, ozone, water and carbon dioxide. The green colored curve shows the change in solar radiation trend during the 11 year solar cycle, the dashed line is the changes in TSI which is actually the relative difference between the solar maximum and minimum [Lean, 2010].

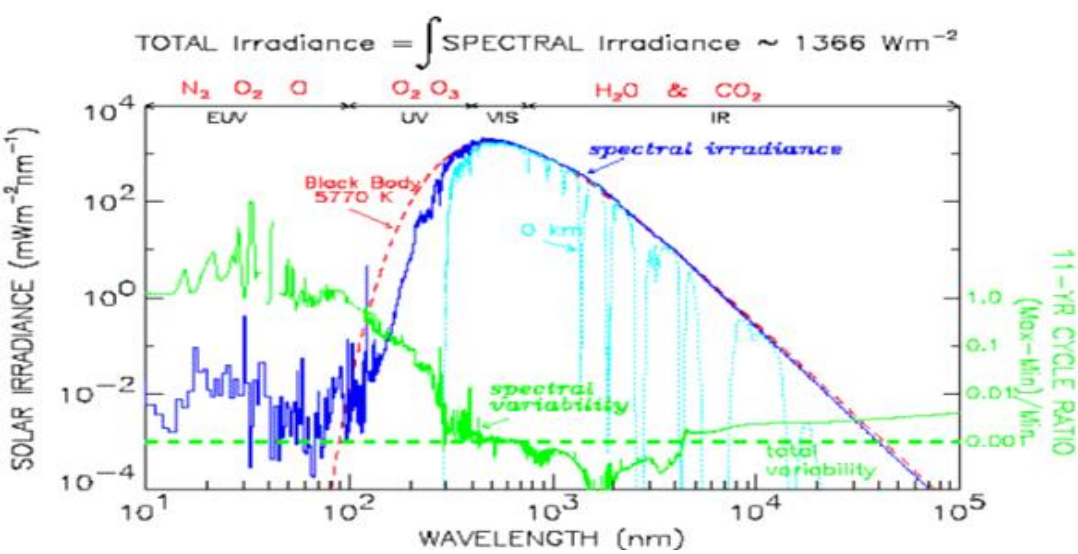

Figure 2.4: Solar spectrum, variabilty and atmospheric absorption [Lean, 2010]

2.5 Solar activity UV emissions & the stratosphere

At the top of the atmosphere the total power of the sun's spectrum is 1367 $\mathrm{W/m^2}$, which is divided into three major wavelength regions: 50% infrared, 40% visible and 10% UV (ultra violet) [Benestad, 2002]. When measured at ground level, 48% of the sun's electromagnetic energy is focused in the visible fraction of the spectrum, around 1% (15.5 $\mathrm{W/m^2}$ out of $1367\ \mathrm{W/m^2}$) comes from the UV and the remaining 51% is associated with the infrared radiation. Wavelengths below 100nm undergo a fractional change ($\frac{\Delta I}{I}$) of 10% to 20% during a solar cycle. The integrated spectral Irradiance ($\Delta I = I_{max} - I_{min}$), however, changes on a very small scale that is 1.3 $\mathrm{W/m^2}$, corresponding to 0.1% [Lean, 1998]. The UV radiation contributes only 9% to the total solar irradiance but over a solar cycle fluctuations of up to 32% have been recorded. This fractional variation in the UV radiation affects the chemical process occurring in the earth's stratosphere. UV radiation affects the local heating as it is absorbed in the stratosphere by ozone and influences its photo chemistry. Another important consequence of the UV radiation in the stratosphere is its influence on the wind circulation [Lockwood et al., 2011].

The main constituents that absorb UV above the troposphere are oxygen, nitrogen and ozone. Hence a small portion of radiation reaches the surface. Different studies have observed the changes in stratospheric ozone as the solar irradiance varies over 11 years. Observations show an increment of 1% to 2% in the total ozone column at solar maxima. A good agreement has been observed between ozone column and the solar activity [Haigh, 2007]. In summary the solar activity has a great influence on the chemistry, circulation and thermal structure of the atmosphere. That is why long term observations of the solar activity are required to set up reliable computer models to estimate the affect of solar variability on our climate.

2.6 Latest solar cycle and prediction techniques

In the middle of the 18Th century, the first attempt to plot the sunspot number against time was made, it is named as the solar cycle number 1. Every solar cycle afterwards was numbered incrementally. The current solar cycle is number 24.

The current solar cycle is unique. In a way it resembles with the solar cycle number 14, which occurred during (1902-1914). The common feature during these two solar cycles is a similar magnitude of maximum solar activity. Cycle 14 reached its maximum in 1906 and had a maximum of 64 sunspots. The cycle 24 has given a smoothed number of sunspots 66 as of February 2013. These two cycles are the lowest recorded solar cycles ever since 1902 [Hathaway, 2013].

Solar cycle 24 lasted 4 years (started peaking in March 2013), since it started at the end of 2008. This cycle will probably reach its maximum during fall 2013 and then descend. Predictions are difficult.

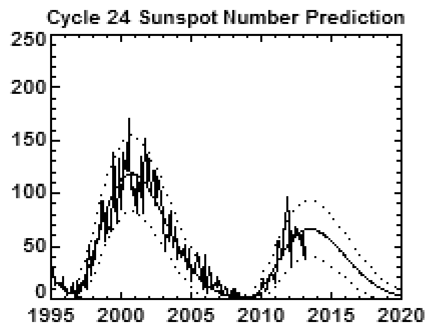

Figure 2.5: Solar cycle no 24 until March 2013 [Hathaway, 2013]

Figure 2.5 [Hathaway, 2013] shows the sunspot numbers during solar cycles 23 and 24. The solid line and the dotted lines show the mean prediction and its possible variation [Hathaway, 2012].

Different techniques are used to predict the 11 year solar cycle [Hathaway et al., 1994]. NASA introduced a technique in which the sun's minimum can be related to a geomagnetic index which is then correlated to the following maximum of the solar cycle. This model also has some shortcomings which scientists are trying to improve [Hathaway, 2013].

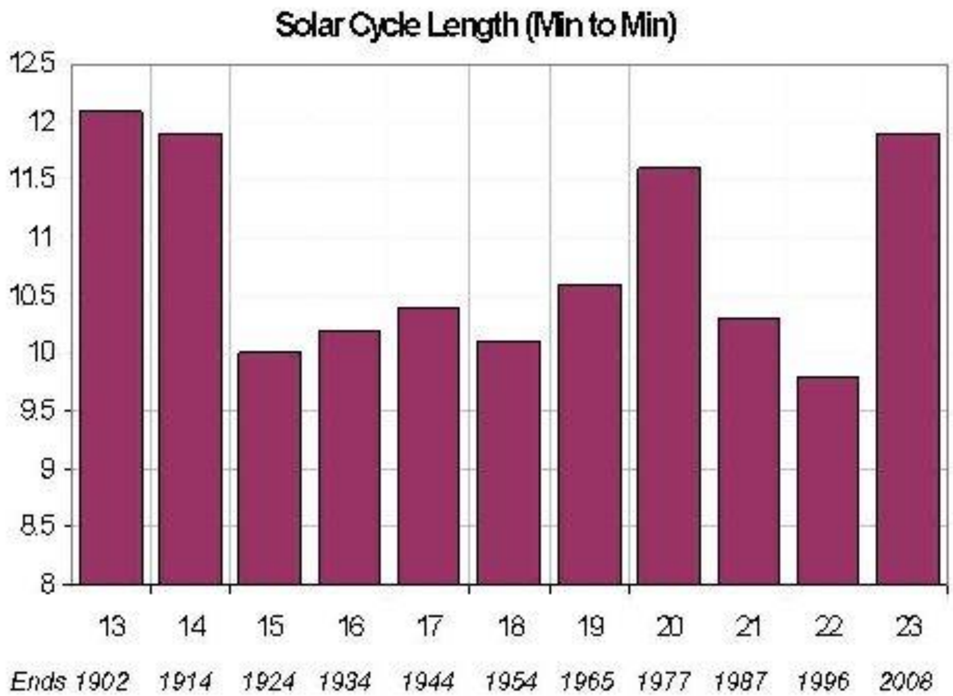

Figure 2. 6: Solar cycle lenthgs altering from 10 to 12 years [Watts, 2012]

Figure 2.6 [Watts, 2012] the length of the solar cycles from 1902-2008 representing about 10 solar cycles. It is apparent that solar cycle does not have a length of exactly 11 years but instead the cycle length varies with a standard deviation of roughly 14 months [Hathaway, 2010].

Large uncertainties are associated with the predictions about a solar cycle. Figure 2.7 [Dikpati et al., 2006] is an illustration of the predictions about the cycle number 24, according to which, the amplitude of the current cycle would have been large but it turns out to be the lowest amplitude over 100 years. Hence making prediction about the solar cycle still remains a challenge.

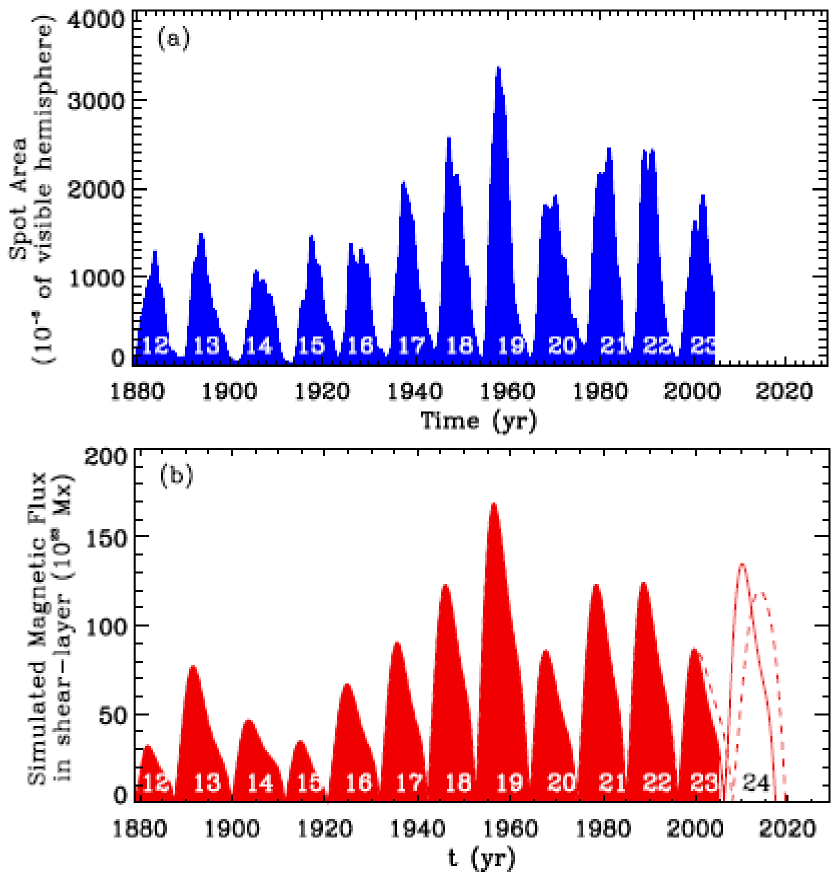

Figure 2. 7: Solar cycles starting from number 12 to 23 shown in the upper panel and solar cycle no. 24 predictions in the lower part [Dikpati et al., 2006]

Chapter 3: Mg II index and error estimation

3.1 Importance of Fraunhofer lines

The series of spectral lines (dark features in the solar spectrum) that are actually absorption lines are known as "Fraunhofer lines". Joseph Fraunhofer, a German physicist, discovered these absorption lines in 1814. He was able to sketch about 570 lines over different wavelength ranges. Satellite based measurements of sunlight revealed thousand of additional spectral lines. He sub-divided absorption features from letter "A" to "K", where A and K corresponds to higher and lower wavelengths respectively. The dominant Fraunhofer absorption lines lettered A to K from the right in the solar spectrum are depicted in Fig. 3.1 [Coffey, 2010].

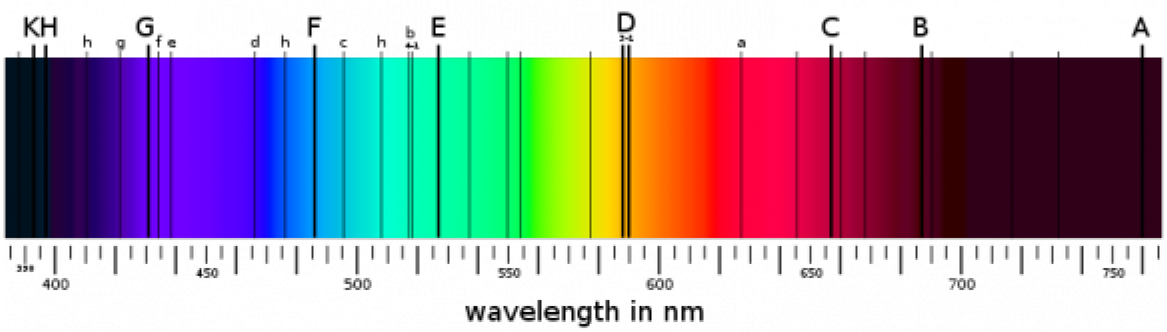

Figure 3. 1: Fraunhofer lines showing different absorption lines from A to K [Coffey, 2010]

Forty-five years later Kirchhoff extended the work of Fraunhofer and found out that these dark lines in the solar spectrum were caused by the absorption of different chemical elements present in the sun's atmosphere. These absorption features (dark lines depicting light loss) are acquired as a result of a cold and dilute gas being in between the photon source (the source of broad spectrum) and the detector. Photons are absorbed and light is re-emitted in different directions. This leaves a prominent decrease in the intensity of light in the frequency range and the direction of the incident photon.

A typical temperature profile of the solar atmosphere and for the altitude range where Fraunhofer line absorption occurs is displayed in Fig. 3.2 [Liou, 2002].

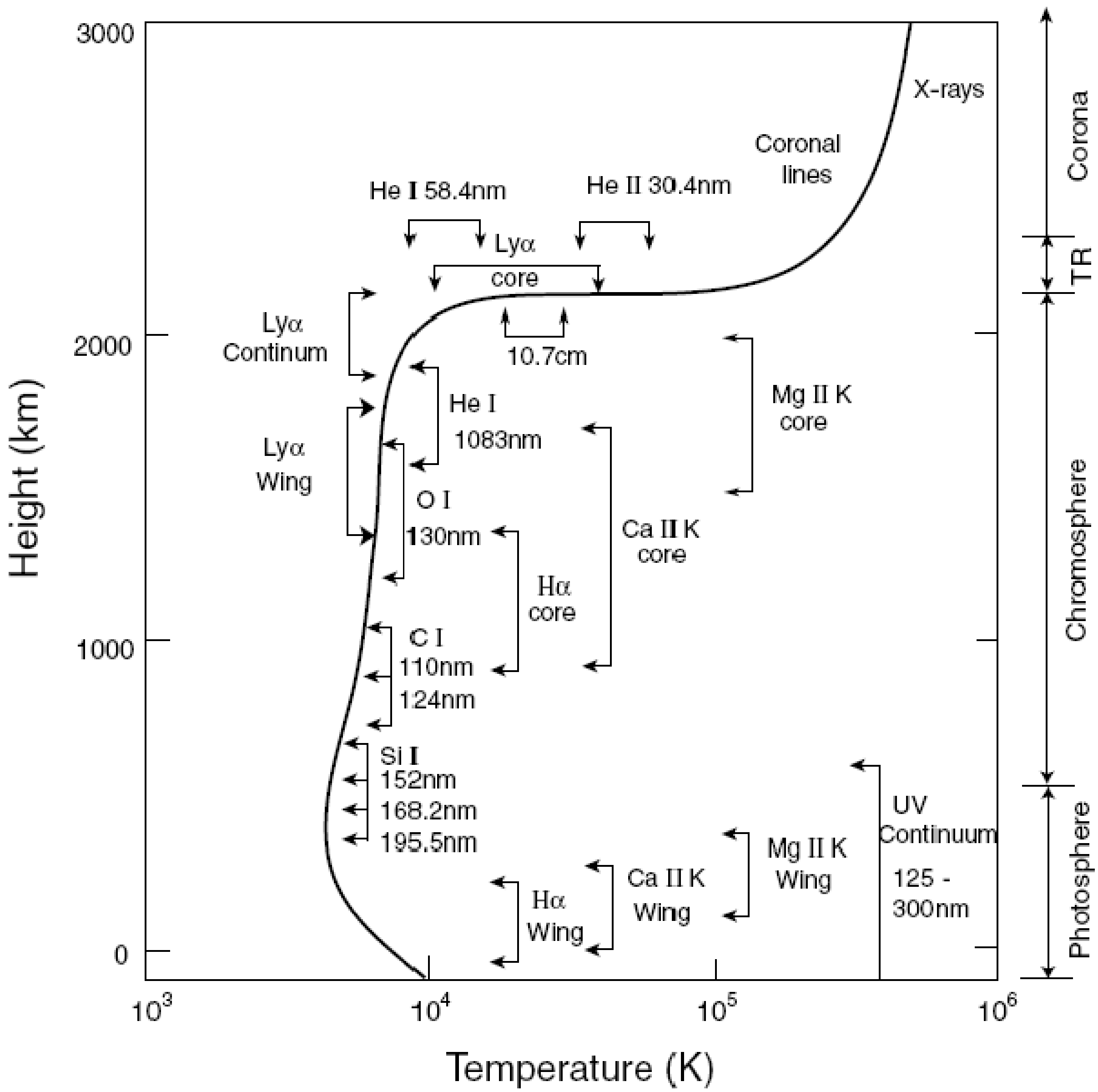

Figure 3.2: Temperature profile of solar atmosphere and Fraunhofer absorption lines at different altitudes [Liou, 2002]

As discussed in chapter 1, the copiously found element in the sun is hydrogen. This abundance makes it special as it can absorb in neutral as well as in the ionic state. All other elements, e.g. H, He, C, Si, Ca, Mg. etc., which are shown in Fig. 3.2 are also present in the sun's atmosphere, absorbing at different wavelengths, altitudes and temperatures. The Roman numbers I and II stand for neutral and single ionized atoms, respectively [Liou, 2002].

3.2 Mg and Mg II (Magnesium Doublet)

Magnesium (Mg) is the 8th most abundant element in the Earth's crust and making up 13% of the earth's mass. Ions of Mg are highly soluble in water. It is the 9th most commonly found element in Universe. In fact the sun contains one Mg atom for every 28,000 atoms of $\mathrm{H_2}$ [Armstrong, 2006]. Mg has an atomic number of 12 and its atomic mass is 24.305 amu, its core consists of 12 protons and 12 neutrons. Mg has an oxidation number of +2 and can therefore lose two electrons. Hence the magnesium cation is represented by $\mathrm{Mg^{+2}}$. It has a density of 1.738 g/cm³ and a melting point and boiling point of 923K and 1380K, respectively [Bandyopadhyay, 2013].

The main reasons for the existence of Mg in stellar atmospheres are its high boiling and melting point. Magnesium has three isotopes; their abundances are 78.98% for $^{24}\mathrm{Mg}$, 10.03% of $^{25}\mathrm{Mg}$ and 11% of $^{26}\mathrm{Mg}$ [Catanzaro et al., 1966].

From Fig. 3.2 it is evident that some lines exist in pairs which are called "doublets". Each line in that doublet has its own individual identity, given by specific letters. The Fraunhofer spectrum encompasses the Ca II (Ionized calcium or calcium doublet) emission lines termed by "H" and "K". Mg II emission doublet lines are designated by "h" and "k". In order to keep the distinction between Ca II and Mg II authors have used "h" and "k" for the ionized magnesium emission lines where h represent emission at 280.27 nm and k at 279.55 nm [Anderson et al., 1988].

Mg II is more sensitive to chromospheric heating than Ca II, the reason is that the Mg II h and k lines are higher in altitude than the Ca II H and K doublet hence more sensitive to temperature [Skumanich et al., 1973]. The magnesium doublet is a result of its unique electronic configuration. This produces two closely packed emission lines at 280 nm. The atomic number of Mg is 12, as stated above, and its electron configuration is written as $1\mathrm{s}^2, 2\mathrm{s}^2, 2\mathrm{p}^6, 3\mathrm{s}^2$. To get to a stable state, Mg can lose the two outer most electrons and achieve the stable state of $1\mathrm{s}^2, 2\mathrm{s}^2, 2\mathrm{p}^6$. The other process is rather difficult and occurs when an electron from the 3s shell is excited and moves to the higher energy shell 3p. The electric field of the nucleus and spin motion of electron interacts with each other electromagnetically causing "spin-orbital-interaction" which is responsible for two splitting energy states within the orbit of 3p. This reforms new sets of the quantum numbers. Total angular momentum is represented as "j" and in the same way "$\mathrm{m_j}$" represents total angular momentum, $\mathrm{m_I}$ represents magnetic quantum number and $\mathrm{m_s}$ represents projection quantum number.

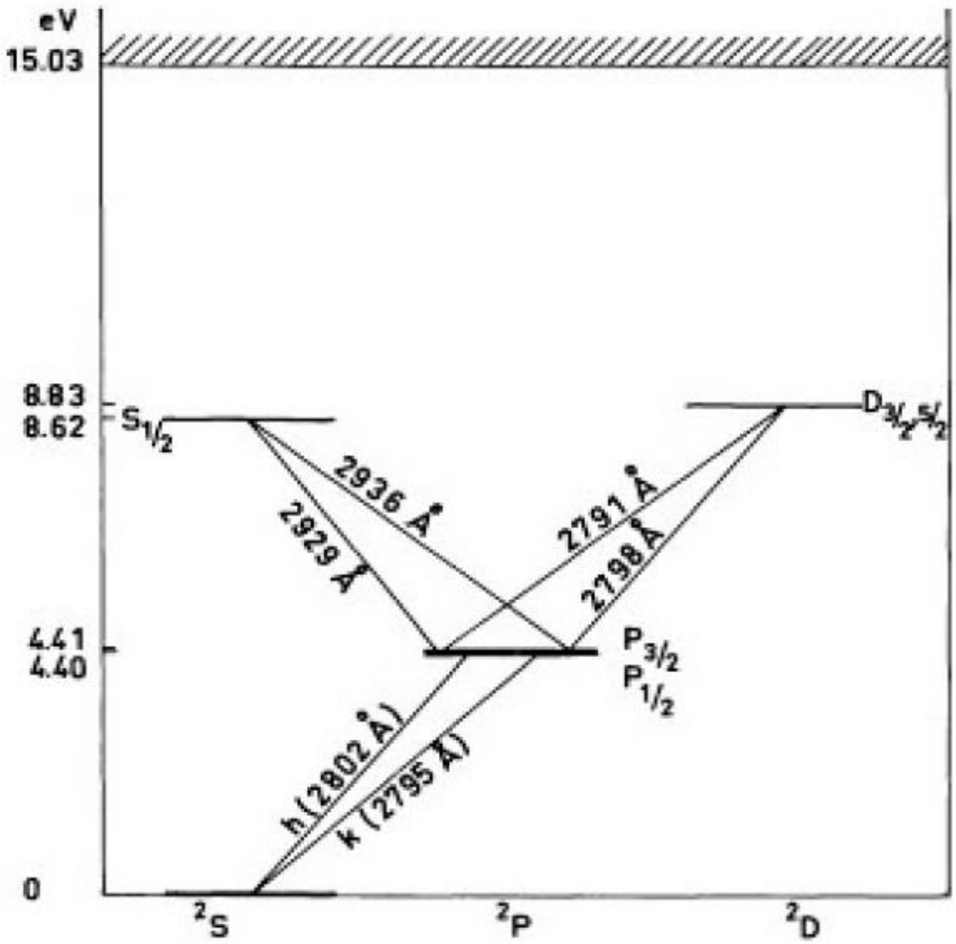

Figure 3.3: Energy diagram of Magnesium doublet [Skumanich et al., 1973]

The newly formed two different energy states in the 3p orbit (Fig. 3.3) will have different values of m_j that are $\frac{1}{2}$ and $\frac{3}{2}$, at the same time quantum number of 3s state is $\frac{1}{2}$, see Fig. 3.3 [Skumanich et al., 1973]. This way, the transition from 3p to 3s will have two probabilities. Those are $3p_{1/2}$ to $3s_{1/2}$ and $3p_{3/2}$ to $3s_{1/2}$. These transitions yield emission lines at 4.40ev with 0.01ev spacing. This is the main principle of the two emission lines at 280 nm by ionized magnesium.

3.3 Mg II Index

From the preceding discussions it could be expected that, the Mg II will have two distinctive lines of absorption. But this is not the case since these lines overlap quite well with each other and appear to be a single line. The origin of these absorption lines is the photosphere of the sun. The Mg II emission lines are narrower as they originate in the less dense chromosphere [Skumanich et al., 1973].

Absorption happens when radiation comes out from the radiative and convective zone and is trapped by the photosphere and by the upper atmosphere of the sun. The chromosphere is the source of emission as it gives rise to faculae. They are responsible for temperature variations in the chromosphere. These emission lines appear at the exact same central position of the absorption line.

The absorption feature emerging from the photosphere is less variable than the emission lines emerging from the chromsphere. These emission lines (h and k) are more variable because these are highly related to temperature fluctuations in the chromosphere. As more sunspots appear on the surface of the photosphere at the maximum of the solar activity, more faculae appear in the chromosphere above, hence raising the temperature. As a result of this, more visible and strong Mg II emission lines appear in the solar UV spectrum [Skumanich et al., 1973].

“The Mg II core-to-wing index is a ratio of the Mg II chromospheric emission at 280 nm to the photospheric radiation in the line wings, and is used as an indicator of solar activity” [de Toma Giuliana et al., 1997]. The Mg II index is a monitor of solar chromospheric variability [Viereck et al., 2004]. The chromospheric activity of the sun is highly influenced by the appearances of plages and faculae, accountable for increases in UV radiation [Weber et al., 2013]. Mg II time series are available from satellite measurements since 1978 [Viereck et al., 2004, Weber et al., 2013]. There are several different instruments at different spectral resolution measuring solar irradiance at 280 nm. From Mg II indices derived from different instruments it is fairly straightforward to create a long term single time series called the Mg II composite index. As this proxy correlates extremely well with UV solar irradiance changes, it is a convenient proxy for solar activity and has been successfully linked to atmospheric changes in ozone and temperature. Also, spectral solar models have been derived from this proxy that can be used in climate models to investigate the solar impact on climate and ozone [Viereck et al., 2004].

Figure 3.3 shows the Mg II absorption and emission cores. As the solar cycle proceeds towards its maximum activity and more sunspots appear on the photosphere appear consequently, hot regions of plages and faculae erupt producing an emission core at Fraunhofer lines [Weber, 1999]. Hence, strong signals will be measured for the core of Mg II while at the same time the wings remain almost unchanged (less variable photosphere). As a ratio (Mg II index), the magnitude will increase towards the solar maximum. The balloon measurements at very high spectral resolution nicely show the doublet structure of the Mg II absorption and emission [Anderson, 1988, see Fig. 3.4].

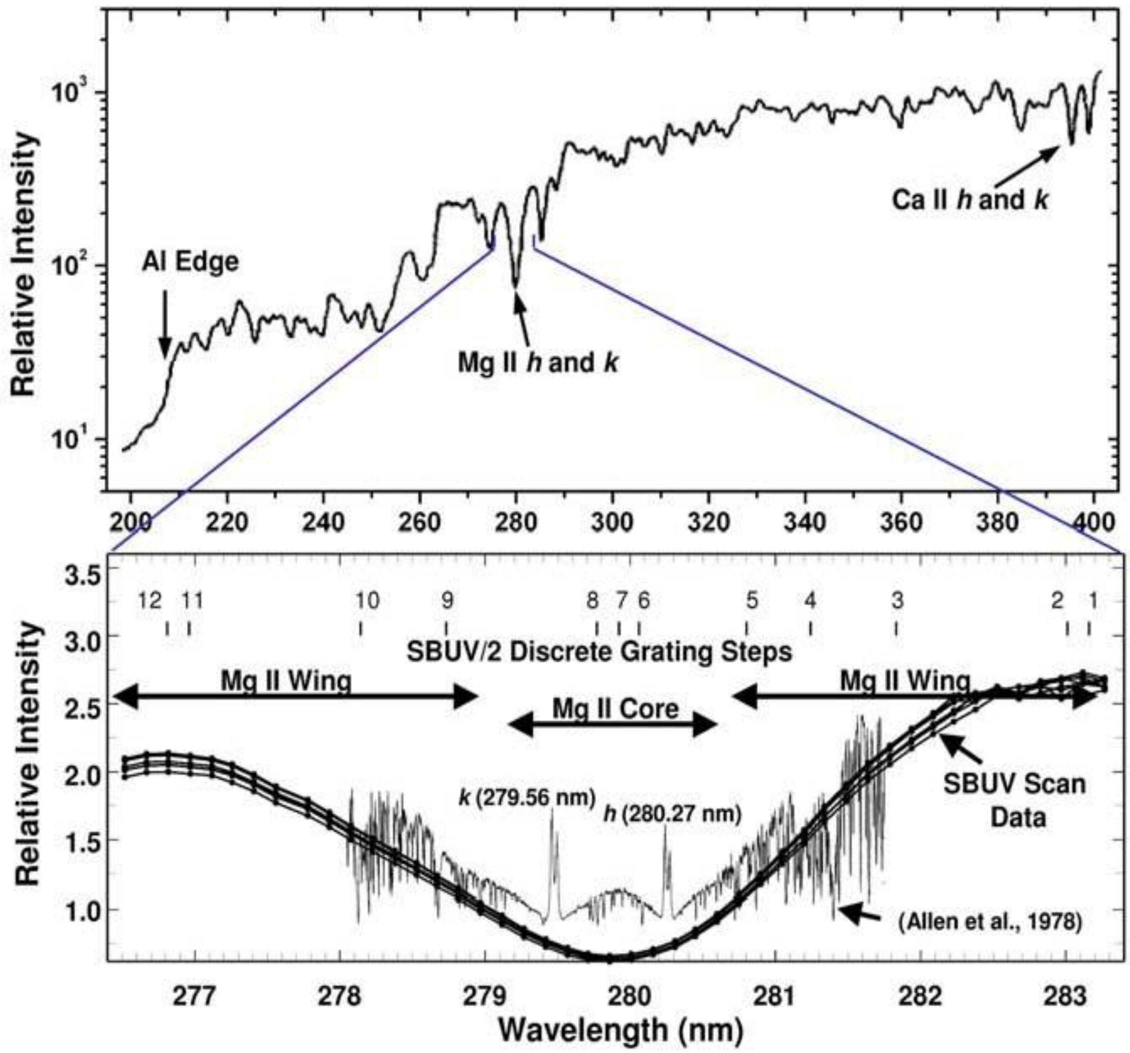

Figure 3.4: Satellite measurements from SBUV of Mg II index from ballon measurments at very high spectral resolution [Anderson, 1988]

In the same way as the solar activity goes down, the chromospheric temperature reduces and emission lines get weaker, hence Mg II index (as a ratio) decreases. The Mg II index derived form the core-to-wing ratio has the advantage that it cancels out to first order optical degradation effects that many UV instruments in the space and also spectral solar irradiance measurements suffer from.

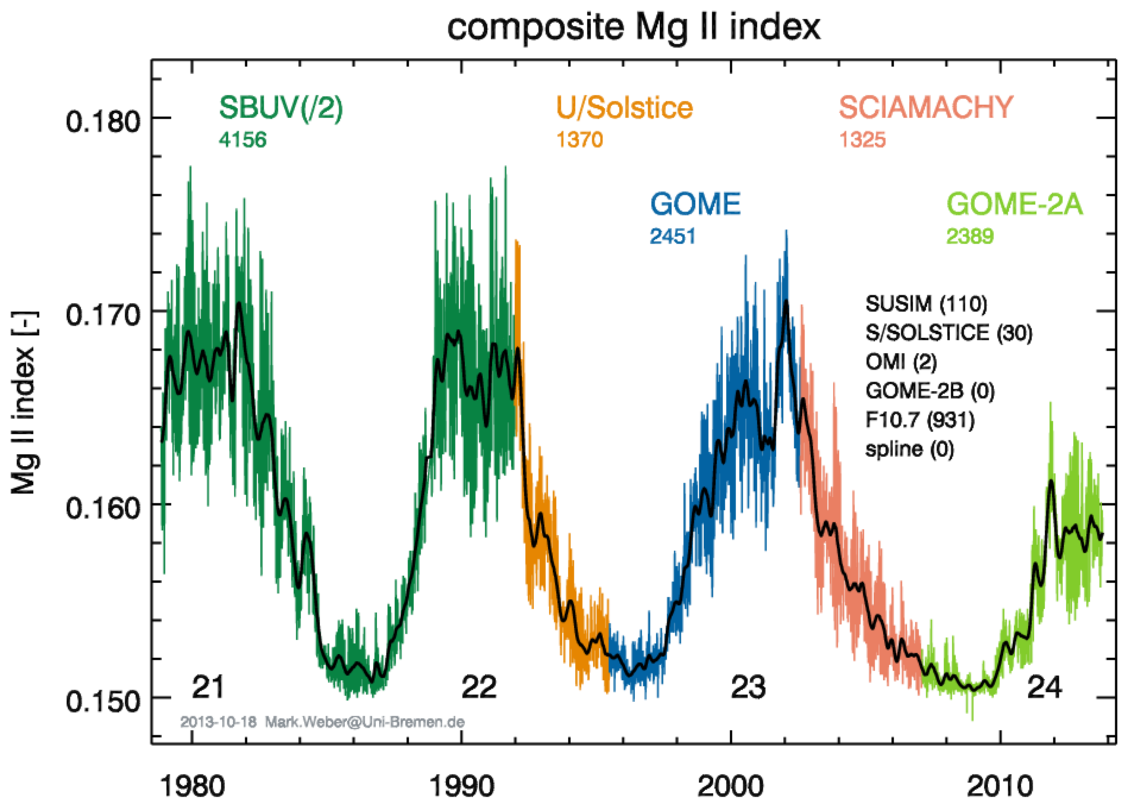

Figure 3.5: Mg II Composite Index [Weber et al., 2013]

The composite Mg II index has been retrieved from several different satellites over 32 years and from solar cycle number 21 to 24. Figure 3.5 shows the University of Bremen composite Mg II index as updated from Weber et al, (2013) and available at <<www.iup.uni-bremen.de/UVSAT/research/solarradiation>>. Different colors are representative of the different satellites that dominate the composite time series in any given time period. e.g., dark green color shows SBUV(/2), yellow for U/Solstice, blue for GOME, light red for SCIAMACHY and light green for GOME-2. The black line shows the smoothed Mg II index time series.

3.4 Other solar proxies

Three different solar proxies are to be compared with the Mg II index: Lyman alpha, the international sunspot number, and the F10.7 solar flux.

3.4.1 Lyman alpha

The Lyman alpha is a pronounced emission feature at 121.6nm. It is produced in the upper part of the chromosphere, passing through corona and space and finally reaching our atmosphere.

This line strongly contributes to ionization in the ionosphere. It changes up to 50% during the 11 year solar cycle. It is a good proxy of the sun cycle in the far UV range (120-200 nm).

Composite Lyman alpha is available from the LASP Interactive Solar Irradiance Data Center (http://lasp.colorado.edu/lisird/lya/ last access date: 12.03.2013).

3.4.2 Daily sunspots

This is one of the oldest techniques to obtain a record of sun activity over a long period of time. This is just a calculation of number of sunspots appearing on the face on the sun which are observed by using authentic and advance optical devices. There are two international sunspot publishers using the same formula for the measurements. The first one is the "Boulder Sunspot Number" provided by NOAA (http://www.ngdc.noaa.gov/stp/solar/ssndata.html) in the United States and second one is the "International Sunspot Number" by SIDC (http://sidc.oma.be/sunspot-data/) in Belgium.

In this study, the daily sunspots are taken from (http://sidc.oma.be/sunspot-data/ last access date: 12.03.2013).

3.4.3 The F10.7 cm solar flux

The F10.7 cm solar flux is one of the longest and oldest records of solar cycle observations. Measurements by radio telescope started by the Dominion Radio Astrophysical Observatory, Canada. The record is available since 1947 and it is a good indicator of changes in the solar cycle over 11 years and it correlates with other proxies very well.

In this study the F10.7 cm solar flux is taken from National Oceanic Atmospheric Administration under(ftp://ftp.ngdc.noaa.gov/STP/SOLAR_DATA/SOLAR_RADIO/FLUX/Penticton_Observed/daily/DAILYPLT.OBS last access date: 12.03.2013).

3.5 Error analysis

All measurements have uncertainties known as errors. This must be reduced by improving the measurement techniques (or by repeating the experiment/measurement). An error can be defined as a deviation between the measured value (results) and the real value, it is nothing but the difference between observed and true value. Such errors still exist after improving the measurement techniques and have to be estimated well to ensure the quality of results.

The main challenge faced in the scientific results is the error generally introduced by random fluctuations (random errors). On the other hand, accuracy and precision are always constrained by systematic errors. These uncertainties in measurements are called errors and different ways to estimate them are referred to as error analysis [Robinson, 2003].

3.5.1 Accuracy and Precision

Accuracy and precision are two different quantities and it is very important to distinguish these two terms. An accurate measurement is always very close to the true value, this helps to define accuracy as, the measure of closeness of measured results to the true value. While a precise measurement of an experiment, produces results that are well determined. It is not necessary for a precise measurement to be in a agreement with the true value. This illustrates the repeatability of an experiment in unchanged conditions, yielding the same results. Mostly, it is defined or described by using the standard deviation. Figure 3.6 provides a good description of precision and accuracy [NOAA, 2013] showing different cases where measurements that are precise but not accurate and vice versa are not suitable/acceptable scientifically. Accuracy and precision in an experiment must be considered simultaneously [Robinson, 2003].

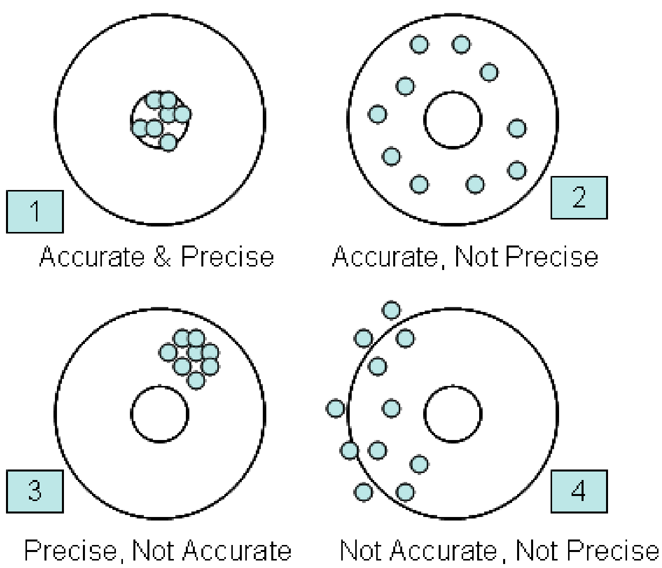

Figure 3.6: Concept of Precision vs Accuracy [NOAA, 2013]

3.5.2 Systematic and Random errors and Gaussian distribution

The different steps considered for analyzing measurements are illustrated in Fig. 3.7 [Stephen, 2013]. They represent the different scientific tools worthwhile to utilize, to evaluate the quality of measurements. Most of the emphasis of this section is placed on systematic and random errors.

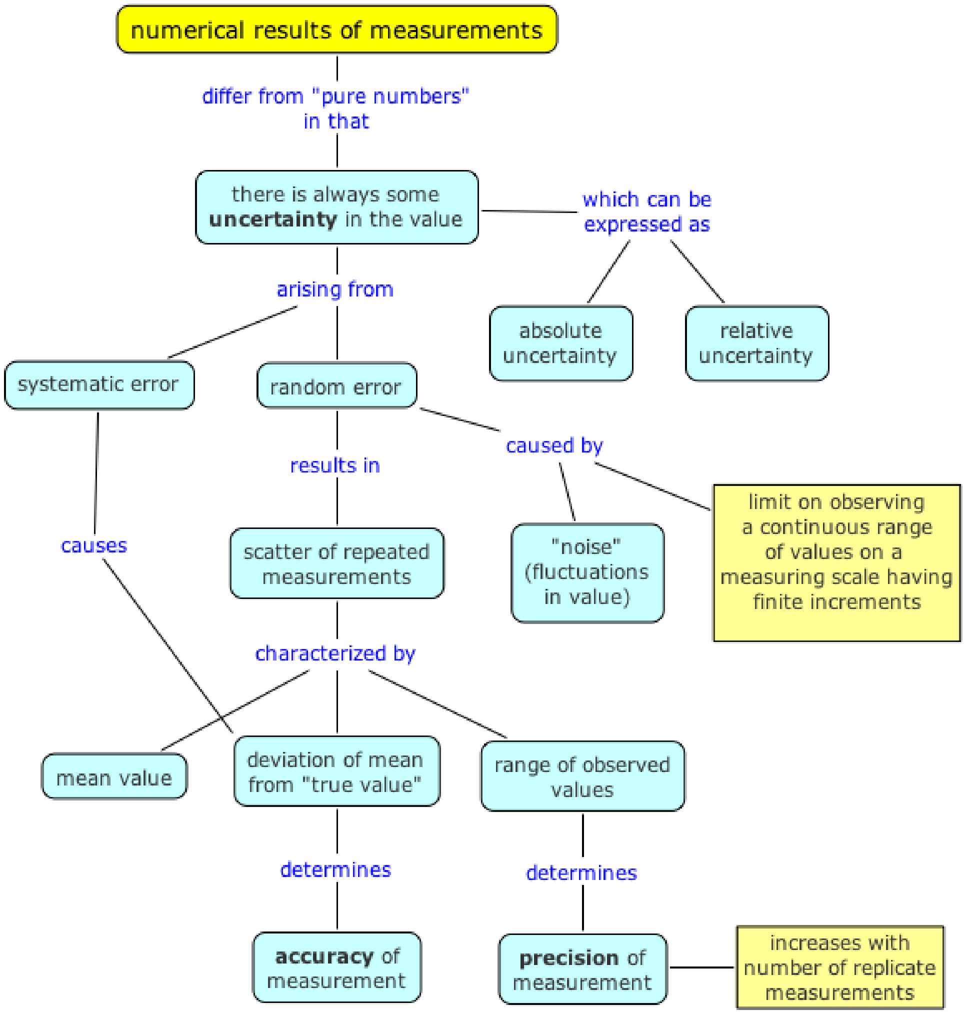

Figure 3.7: Discription of data handling [Stephen, 2013]

Systematic errors are caused by factors that are systematically affecting the patterns of measurements. Following are some possible causes of systematic errors.

1) Imperfect calibration of instrument
2) Changing environment in which sensor operates
3) Variability in the experimental conditions

Systematic errors are mostly constant as in the case of imperfect calibration, while in the cases 2 and 3, they are found to be changing over time. Constant errors are difficult to remove; they cannot be removed by averaging rather reviewing the calibration is a way to remove them. Variable systematic errors cannot be removed properly as they cannot be predicted or measured. Random errors bring inconsistency in the experiment as measurements are performed. This repeated inconsistency is unpredictable but has zero expected value. This error cause fluctuations in the data set and scatter the measurements. High precision reduces the fluctuation. Accuracy up to some extent also depends upon random errors [NOAA, 2013].

Poisson, Binomial and Gaussian are the three distributions mostly used to analyze experimental data. The Gaussian distribution, also called normal distribution, can be derived from the Poisson as well as the Binomial distributions. The Gaussian distribution is the most important one as it describes random errors, it helps to characterize the randomly distributed errors [Robinson, 2003].

3.6 Errors caused by optical degradation

Sun observing instruments usually operate in the harsh space conditions which are the main cause of the optical degradation. The optical elements on the sensor possess vulnerable characteristics as they operate in the Vacuum ultra violet (VUV), Extreme ultra violet (EUV) and UV spectral regions. This part of the solar spectrum, being shortwave and highly energetic, has a tendency to harm the satellite and cause uncertainties and errors in the measured data. As instruments ages and are exposed to these harsh solar radiation, degradation increases with time. The calculation of expected degradation and then its correction are two crucial parts of data analysis and scientific investigation.

Degradation is a combination of the harsh solar irradiance and instrumental contamination. This contamination causes polymerization of organic material and subsequently can irreversible deposition of this material to the optical surface of the instrument. The contamination layer is built up by the out gassing of spacecrafts. A certain amount of hydrocarbons stick to the optical surfaces and polymerize. Later the polymerized hydrocarbons are stiffed by the UV radiation coming from the sun. This layer grows with time and signals coming from the sun are strongly attenuated. EUV light creates positive charges at the interface between the silicon and silicon oxide that thickens the dead layer and enhance degradation. In addition ice layers can form on the detector when cooling the detector. This causes an etalon patterns in the solar spectrum.

As an instrument operates and ages, chances to recover the instrument from degradation are become slim. The contaminated layer can be heated with the electrical power supply. However the strength of this supply is limited and can never be assured that it can melt the layer and clean the instrument properly. That is why the assessment and monitoring of the instrumental degradation is a very important step to reach a better level of understanding of "degradation". This can also be assured by taking in account these few steps:

1) Careful selection of the following components: optics, coating, imagers, photo detectors, spectrometers, sun observing telescopes, electronics, etc.

2) Stability of radiometric calibration monitoring by using advanced methods.

3) Cleanliness control prior to the launch and by using minimum organic material.

3.7 Errors and Signal to Noise ratio [SNR]

Signal is a quantity that carries information about the measurement of interest.

Noise is an unwanted information which interferes with the signal and alter the precision and accuracy of the measured signal.

Signal to Noise is a random quantity and cannot be removed completely but can be minimized. The magnitude of the noise is also known as the standard deviation of the measurement while signal is known as the mean of the measurement. Instead of addressing noise alone, it is scientifically more useful to describe the signal to noise ratio [Thomson, 2013]. Mathematically it is represented as follows;

$$\frac{\mathrm{S}}{\mathrm{N}} = \frac{\mathrm{mean}}{\mathrm{standard\ deviation\ (S.D)}} = \frac{\overline{\mathrm{X}}}{\mathrm{S}}$$

This is proportional to the inverse of standard deviation.

Causes of Noise Two major causes are well document: the "chemical noise" and the "instrumental noise". There are certainly other factors that produce noise in the data. As it is a random quantity, it is very hard to measure those unknown factors producing fluctuations in the data [Thomson, 2013].

Chemical noise is caused by the un-detective variations, the sources of these variations are mostly observed in the power supply variations, changes in pressure and temperature, changes in the light intensity and chemical equilibrium etc.

Instrumental Noise is associated with the instrument and is a combination of all noises caused by every individual component taking part in the measurement, that is why it is very complex to quantify or to characterize the instrumental noise. Instrumental noise is further categorized as follows: "Thermal Noise", "Flicker Noise", "Shot Noise" and "Environmental Noise".

Thermal Noise is a flow of electrons and other charged particles in electrical circuits and is considered as the main cause of the increase in thermal resistance. Cooling or lowering down the temperature can help to keep thermal noise at a minimum level.

Shot Noise is reported when the charged particles and electrons are leaving their orbital path and cross the junctions and cause inconsistencies in measurements.

Flicker Noise follows an inverse trend (inverse relation) to the signal's frequency that is measured. For frequency less than 100 HZ it is important to be taken into account [Thomson, 2013].

Environmental Noise is observed as the environment of the experimental set up changes e.g., a sun observing instrument degrades as a result of harsh space environment and continuous exposure to the dangerous short wave UV radiation. This aging effect known as degradation brings environmental noise in the data sets.

SNR Enhancement These are some of the physical effects that can be improved to enhance the signal to noise ratio. Choosing better optics for the sensor, bigger apertures and anti-reflecting coatings can enhance SNR. Noise can be reduced by averaging several spectra from repeated measurements as shown in Fig. 3.8. "The data is averaged by dividing the sum for each point by the number of scans performed. The SNR is proportional to the square root of the data collected" [Thomson, 2013]. There are also some computational and digital tools used to improve and enhance the signal to noise ratio. These procedures are applied to smooth the inconsistencies, jumps, irregularities, etc. Precisely measured SNR is a good indicator of errors in the data sets and can be used to validate the calculated errors [Thomson, 2013].

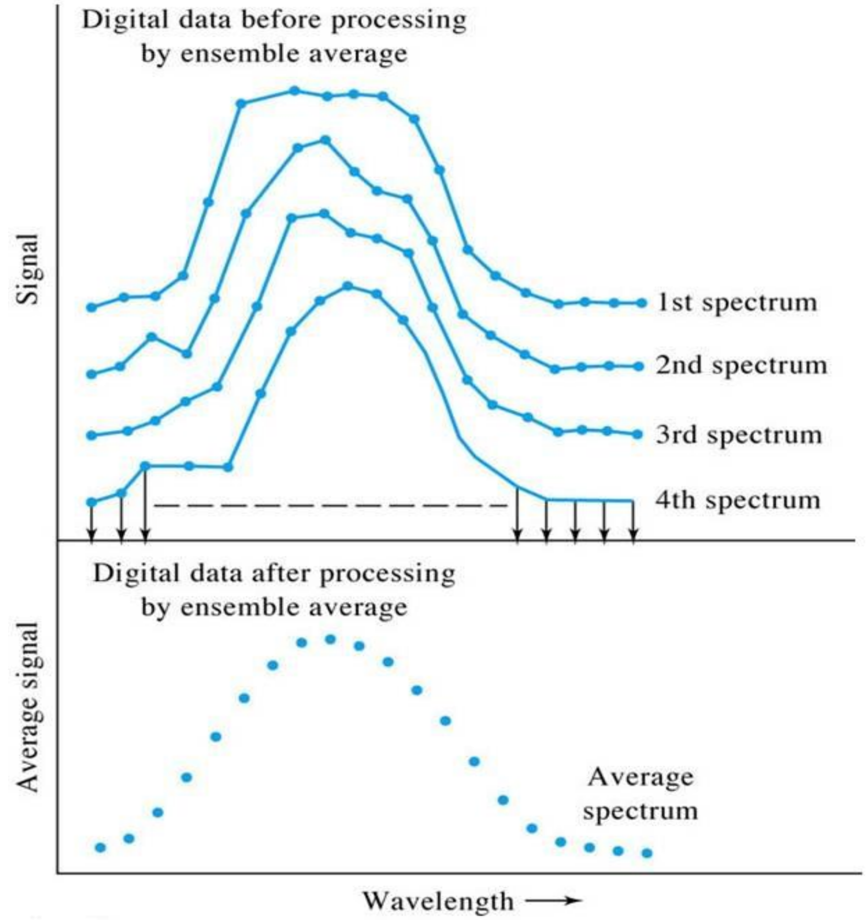

Figure 3.8: Averaging and enhancment of SNR [Thomson, 2013]

Chapter 4: The Instruments

4.1 GOME on ERS-2

Global Ozone Monitoring Experiment (GOME), a nadir viewing instrument is mounted on the European Remote Sensing satellite (ERS-2) launched by the European Space Agency (ESA) in 1995. The main focus of GOME is remote sensing of atmospheric chemistry in Earth's atmosphere, e.g measuring various the concentrations of atmospheric constituents (O_3, NO_2 , H_2O, BrO, NO_3, O_4, O_2, CIO and NO) and provides ozone monitoring. It measures in the spectral range of 240-790 nm with a moderate spectral resolution of 0.2-0.4 nm [Burrows et al., 1999].

GOME measures the solar irradiance and the earthshine signals. In all, the following observations are possible from GOME: aerosols Vertical Optical Depth (VOD), trace gas measurements, surface properties (albedo and spectral reflectance of surface), clouds (clouds optical depth, cloud cover and cloud reflectance), radiance measurements and solar variability (specifically in the UV range of the solar spectrum related to sun 11 year solar cycle) [Burrows et al., 1999]

Figure 4.1 shows the ERS-2 satellite on which GOME is mounted along with other sensors [Cersat, 2005]. The overall height of the satellite is 11.8 m and has a total mass of 2521 kg. ERS-2 carries not only GOME but also several other sensors, Active Microwave instrument (AMI), Radar Altimeter (RA), Along-Track Scanning Radiometer (ATSR), Precise Range and Range Rate Equipment (PRARE) etc.

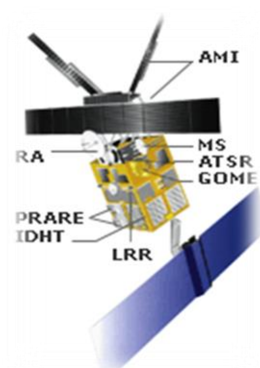

Figure 4. 1: GOME mounted on ERS − 2 with several other instruments [Cersat, 2005]

4.1.1 Solar measurements by GOME

After the launch of ERS-2 in April 1995 it took almost a month for out-gassing until GOME cooled and started regular measurements in June 1995. To measure the solar spectrum by GOME, there are two options. The first one is spectrometric measurements. As GOME is a spectrometer it can measure the earthshine spectra. This means that light from the sun that has been reflected by the earth's atmospheric constituents and by the surface before being measured. The second option is more authentic and reliable where GOME directly measures the sun spectrum, i.e. irradiance. This is done by using a diffuser in the solar light path [Burrows et al., 1993, Weber et al., 1998, Burrows et al., 1999].

Once a day (out of every 14 orbits) GOME measures the solar irradiance. When coming from the night side and crossing the north polar region of earth. The instrument can only passively view the solar disc for about 50 seconds. This measurement of the solar disc helps to build the mean solar spectrum of the sun, which is required to retrieve the Mg II index [Burrows et al., 1999].

Figure 4.2 displays SOLar Stellar Irradiance Comparison Experiment (SOLSTICE) measurements of the solar irradiance together with GOME solar irradiance measurements in the spectral range of 274 to 286 nm, where the Mg II index is retrieved. There is very good agreement seen between these two sensors [Peeters et al., 1997]. SOLSTICE is a sensor very specifically constructed for solar ultraviolet irradiance measurements [Rottman et al., 1993, Woods et al., 1993, Woods et al., 1996].

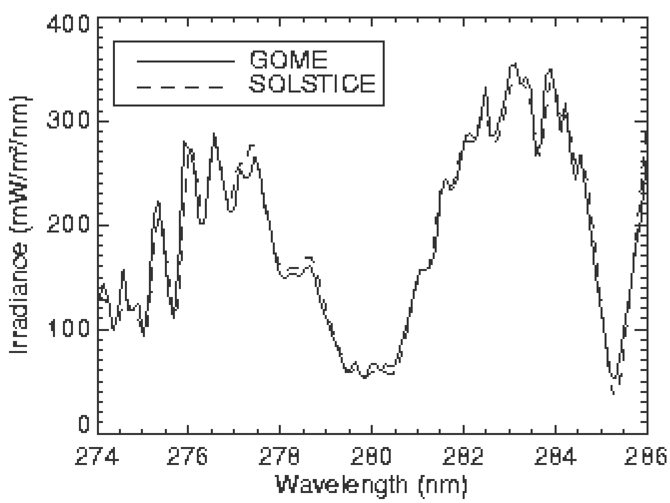

Figure 4.2: GOME and SOLSTICE solar irradiance comparison [Peeters et al., 1997]

This measurement of the solar spectrum shown in Fig. 4.2 has been taken on June 28th 1996, which was a time of solar minimum between cycles 22 and 23. Fig. 4.2 clearly shows that GOME has a better resolved spectrum than SOLSTICE.

4.1.2 Sun diffuser and degradation

The signal received by the instrument from the sun is much more intense compared to the signal coming from the earth and thus is strong enough to saturate the diffuser. A mesh of 20% transmission is placed in front of the diffuser. Stray light is reduced by sandwiching a shutter between the mesh and the diffuser [GOME, 1995, Slijkhuis, 1996]. The major cause of degradation is the scan mirror that picks up the solar light as well as earthshine. It is exposed to the open space environment. Degradation is stronger at smaller wavelengths [Slijkhuis, 2004].

4.2 SCIAMACHY on ENVISAT

4.2.1 ENIVSAT

European ENVIromental SATellite (ENVISAT) is a successor to ESA's satellites ERS 1 and 2 (European Remote Sensing). It orbits in the sun-synchronous polar orbit at an inclination of 98.55°. The mean altitude is approximately 800 km. The mean local solar time (MLST) is 10:00 am in the descending node. The time for one complete orbit by ENVISAT is 100.6 minutes. It completes around 14 orbits around the globe every day. ENVISAT carries a pay load of 10 instruments, SCIAMACHY is one of them. SCIAMACHY is mounted on the upper right corner of the satellite. For the sun observation, it can be seen when the line of sight is directly pointed to the left [Bovensmann et al., 1999].

4.2.2 SCIAMACHY

The SCanning Imaging Absorption spectroMeter for Atmospheric ChartograpHY is the abbreviation of SCIAMACHY on board ENVISAT launched by ESA in March 2002. It is an eight channel spectrometer covering the spectral range of 240 to 2348 nm. It is a passive remote sensing sensor with a reasonable high spectral resolution of 0.2 to 1.5 nm. SCIAMACHY is a instrument with three different observational geometries: Nadir, Limb and sun/lunar occultation [Burrows et al., 1995]. The direct sun and moon observations can also be conducted. The solar irradiance and earthshine radiance enable us to clearly see the reflection, scattering and absorption characteristics of the earth's atmosphere. Earth's surface albedo can be calculated from the ratio of the earthshine radiance and the solar irradiance. Inversion of this ratio gives information about the atmospheric constituents and their abundances. SCIAMACHY provides a larger spectral range (up to 2.4 microns) compared to GOME [Bovensmann et al., 1999]. Similar GOME, a daily Mg II index can be derived from SCIAMACHY.

4.2.3 Schematic & observational modes of SCIAMACHY

SCIAMACHY is a UV-VIS-NIR passive remote sensing spectrometer. The scan mirror is the only part of the instrument that is movable; all other parts of the instrument are fixed. The radiation can enter the instrument, through one of the three ports. The solar spectra ranging from 240-2380 nm can be recorded. All the stray light sources have to be eliminated for the spectrometer to perform measurements in this spectral range. This is done by using gratings, predispersing and a prism [Bovensmann et al., 1999].

The light reaches the spectrometer slit and after the collection of this signal, it is passed to the predispersing prism. Reflective optics are used to split the generated spectrum into four sub-spectra. Short wavelength ranges 240-314 nm and 314-405 nm are passed to channels 1 and 2, respectively. The major parts of the spectrum from 405-1750 nm reach channels 3, 4, 5 and 6 without further reflection. The NIR (near infrared) window from 1940-2380 nm is lead to channels 7 and 8. After all the sub spectrums have arrived at their individual channels the signals are further processed by eight gratings and eight linear 1024 pixels detector array [Bovensmann et al., 1999].

To keep the dark current values low and signal to noise ratio reasonable, every diode array in each individual channel is cooled down. Channels 1, 2 and 6 are kept at 200 K, channels 3, 4 and 5 at 235 K and channels 7 and 8 at 150 K. The whole instrument's temperature is kept at 253 K so as to have a very low probability of infrared emissions from the instrument which could disturb the measurements of channels no 7 and 8 [Burrows et al., 1995, Bovensmann et al., 1999].

4.2.4 Sun observations and M-Factor

Sun observations are performed when (SCIAMACHY is in a position to see directly into the sun. After the ascending node when instrument reaches the North Pole sunrise is occurring. To the left (flight direction) of the earth's limb the sun becomes visible and solar observations are performed [Skupin et al, 2003].

The M factor "It is a ratio of two spectrums, the sun spectrum at a specific time to the calculated spectrum, for the same optical path at a reference time." This is actually a degradation correction (end-to-end) for every single light path [Noël, 2001].

4.3 GOME-2 on MetOp

The Global Ozone Monitoring Experiment (GOME-2) instrument is a nadir viewing spectromenter aboard the Meterological Operational satellite Programe (MetOp-A) operated by Europäische Organisation für imeteorologische Satelliten (EUMETSAT) in co-operation with ESA. In its pay load, MetOp carries a number of instruments dedicated for meteorological and climatological studies. The satellite MetOp was launched October 2008 in a sun-synchronous orbit at a mean altitude of 817 km [Kramer, 2013].

Two additional GOME-2 spectrometers are commissioned for the MetOp program (MetOp-B/C), MetOp-B was launched in September 2012 and MetOp-C is expected to be launched in early 2017. GOME-2 is a successor of GOME and monitors the global coverage of ozone, and other atmospheric constituents and on the daily basis it is observing the solar spectrum irradiance and earthshine spectrum [Richter et al., 2009, Weber et al., 2007].

GOME-2 is a UV-VIS spectrometer is very similar to GOME. All the lessons that have been learnt from GOME and SCIAMACHY projects are taken in account, while designing this new generation instrument (GOME-2 on board MetOp) [Noël et al., 2008, Kramer, 2013].

Figure 4.3 shows the atmospheric constituents measured by GOME-2.

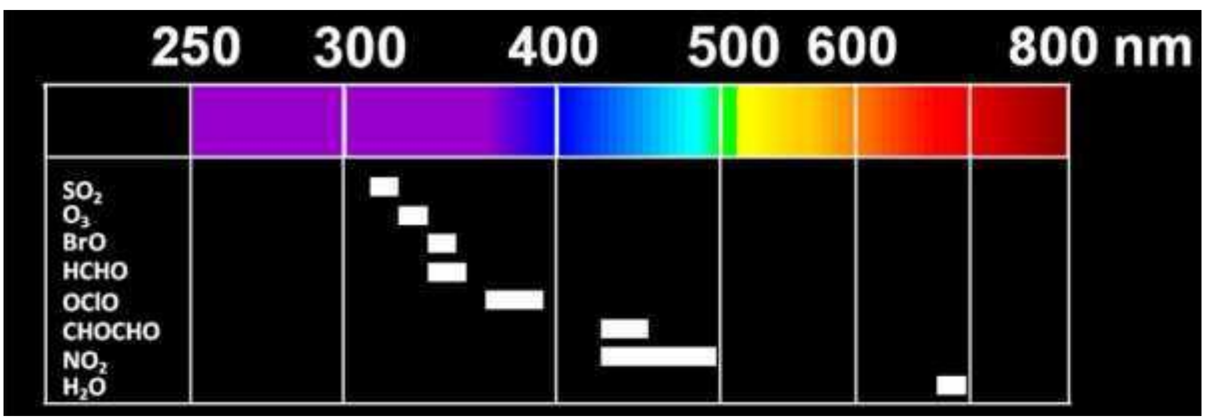

Figure 4.3: Spectral window & observed atmospheric constitunets [Dikty et al., 2012]

The main calibrating system contains a white lamp (not available for GOME), a spectral lamp and a solar diffuser. It has a combination of four channels in UV/VIS. Figure 4.4 shows the schematics of the GOME-2 spectrometer.

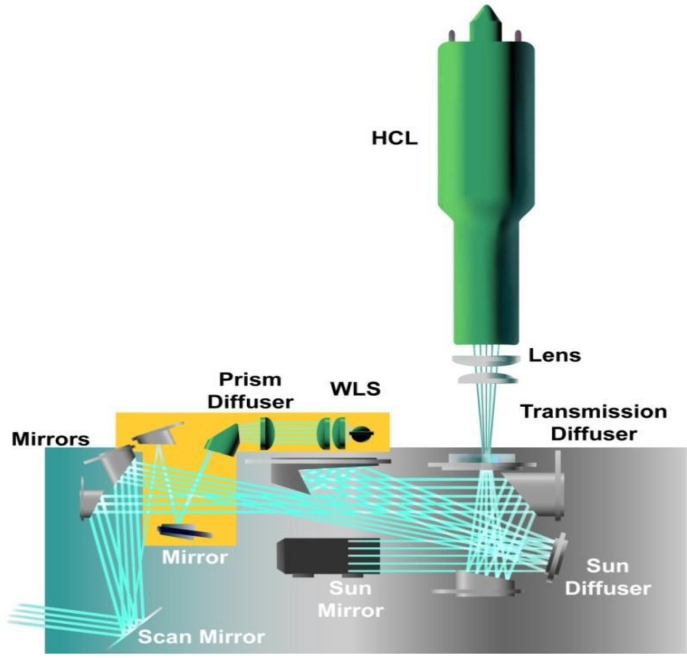

Figure 4.4: Schematics of GOME – 2 [Dikty et al., 2012]

GOME-2 spectrometer scans the sun once a day via a quartz volume diffuser. Figure 4.5 shows schematics of the spectrometer components of GOME and GOME-2, the yellow boxes highlight the new parts introduced to GOME-2.

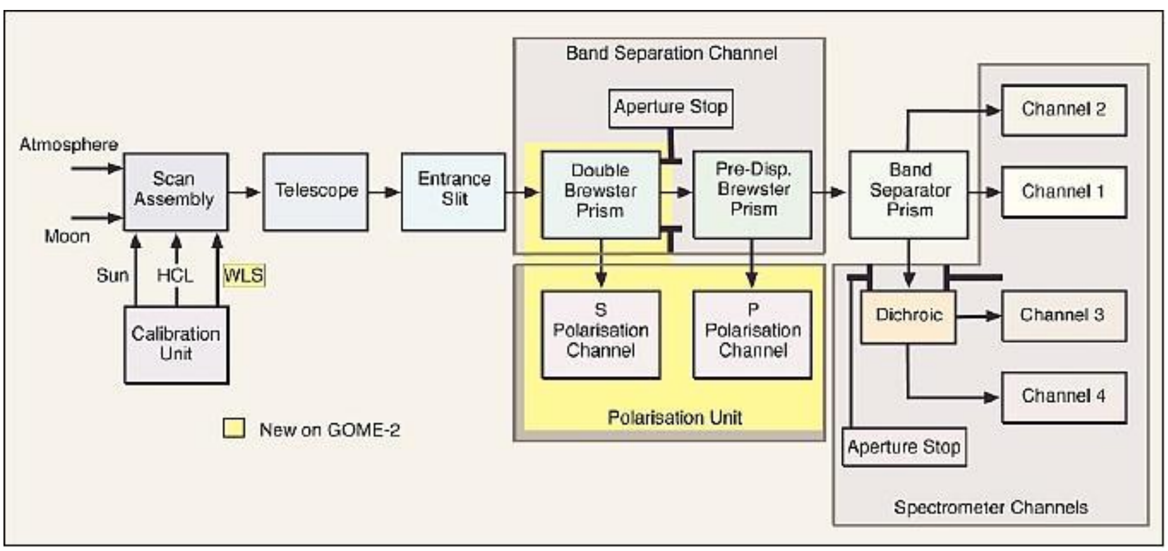

Figure 4.5: Schematics of GOME and GOME – 2 yellow boxes show new components on GOME – 2 [Kramer, 2013]

Chapter 5: The Scientific Method

5.1 Overview

The energy budget of Earth's atmosphere of the earth (especially the upper atmosphere) is influenced by the variability of solar irradiance on various time scales. Change in the level of solar UV radiation results in changes of atmospheric heating by absorption with a capability to effect the global distribution of ozone. This actually causes concerns to earth's environment and is a strong reason to monitor solar irradiance by using space borne instruments like GOME, SCIAMACHY and GOME-2. These instruments observed the solar spectral irradiance in the UV/VIS/NIR spectral region.

Measurements of the sun's spectrum are used to derive the solar proxies. These indices indicate the sun's activity specifically its 11 year solar cycle or its 22 year magnetic solar cycle. The Mg II has been derived from GOME, SCIAMACHY and GOME-2 instruments onboard different satellites in different time spans (but overlapping well to keep a good record) from 1995 until today.

Figure 5.1 shows absorption signatures of different elements, specifically the Mg II doublet at 280 nm measured by GOME (July 22, 1995). Some of the results on the chromosphere and the photosphere and their correlations with Mg II will be discussed in the upcoming section.

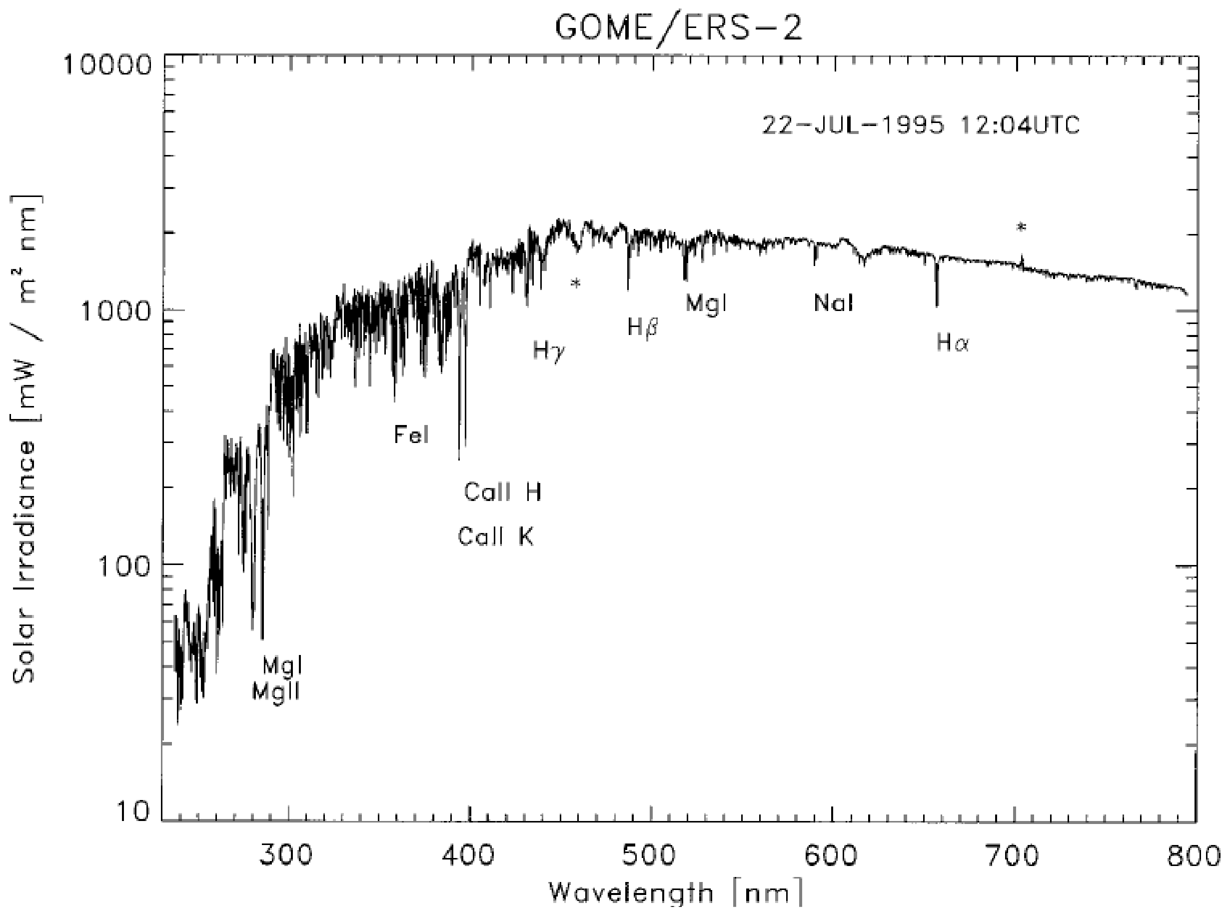

Figure 5.1: Solar irradiance spectrum measured by GOME on 22 July 1995 [Weber, 1999]

5.2 Solar spectral irradiance calibrations and corrections

The main advantages to derive a solar proxy for the sun activity instead of using direct measured solar flux variations are that these indices cancel out or at least take into account the instrumental drifts, while with solar flux it is not very easy to do so. Secondly, there might be some days when no solar measurements are conducted due to unfavorable conditions in space. By using statistical models from the record of the sun measurements (typically solar proxies) the solar spectrum can be reconstructed [e.g. Lean et al., 1997]. Moreover, these proxies are accessible easily and easy to handle in scientific work.

5.2.1 Solar spectrum calibrations

The solar irradiance spectra from GOME, SCIAMACHY and GOME-2 are corrected by applying similar calibration steps. GOME measurements are explained here for which every solar spectrum is normalized to 1 AU earth-sun distance. Data calibration at the ground comprises several steps e.g. the adjustment of the measured solar spectra and the earthshine spectra by GOME keeping a check on the leakage current, focal plane area (related to the voltage control of coolers), stray light control and finally pixel to pixel variability (by using on board LED measurements) [Weber 1999, Weber 1998].

5.2.2 Degradation correction

The Mg II index can be calculated after an etalon correction is carried out. The etalon corrections also provide a degradation correction similar to the m-factor approach used for SCIAMACHY. As the degradation increase is mostly a monotonic function with decreasing wavelengths, fitting a high order polynomial to solar ratios is sufficient to correct for degradation. Figure 5.2 shows the GOME UV degradation correction factor as a function of time obtained from a polynomial (solid curve) to the GOME/SSBUV low resolution ratio (dashed curve) for a solar spectrum measured on 22 December 1998. The degradation correction is applied to a small spectral range around 280 nm

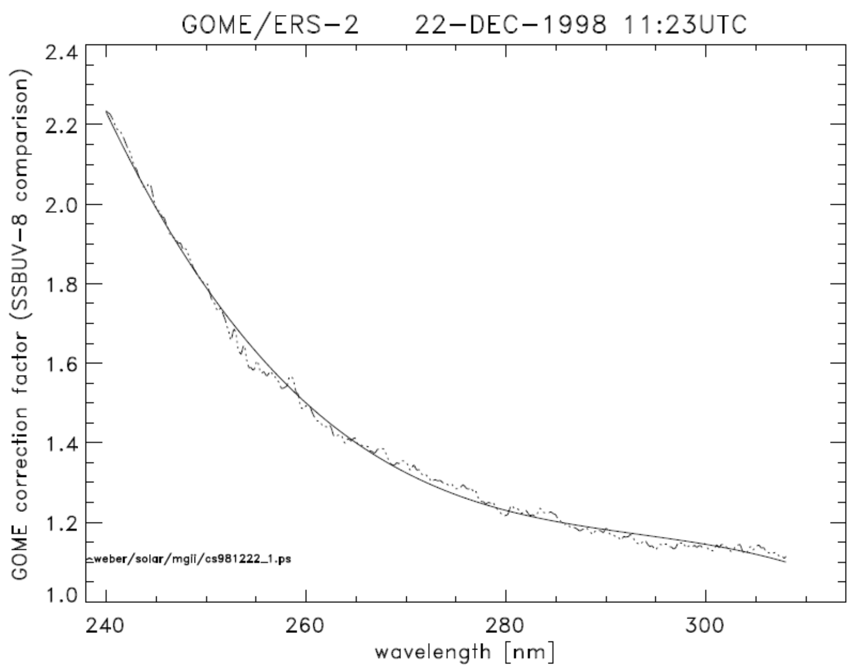

Figure 5.2: Degradation fiting on channel 1 of GOME, on 22 December, 1998 [Weber, 1999]

5.2.3 Etalon correction

The detector arrays in all channels of GOME contain a 3 µm thick layer of SiO_2 specifically on channel 1 (240-315) nm. Switching on the coolers of the detectors followed by an accidental or intended heating of detector causes a thin ice layer to reform on the surface of the SiO_2 protective layer. This ice layer changes the internal reflectivity of the layer that acts as an etalon and thus causes a shifting etalon pattern. The etalon patterns are also visible in solar irradiance ratios.

If the etalon correction is not taken into account in the retrieval of Mg II index there will be jumps and discontinuities after the coolers are switched on.

A simple etalon fit is shown in Fig. 5.3. The fitted polynomial is represented by the diamonds and the Mg II and Mg I emission peaks at 280 and 285 nm are excluded from the fit. F_{ref} is the spectrum of GOME on 14th of January 1997. This procedure helps to remove the jumps and discontinuity in the Mg II index [Weber, 1999, Weber, 1998].

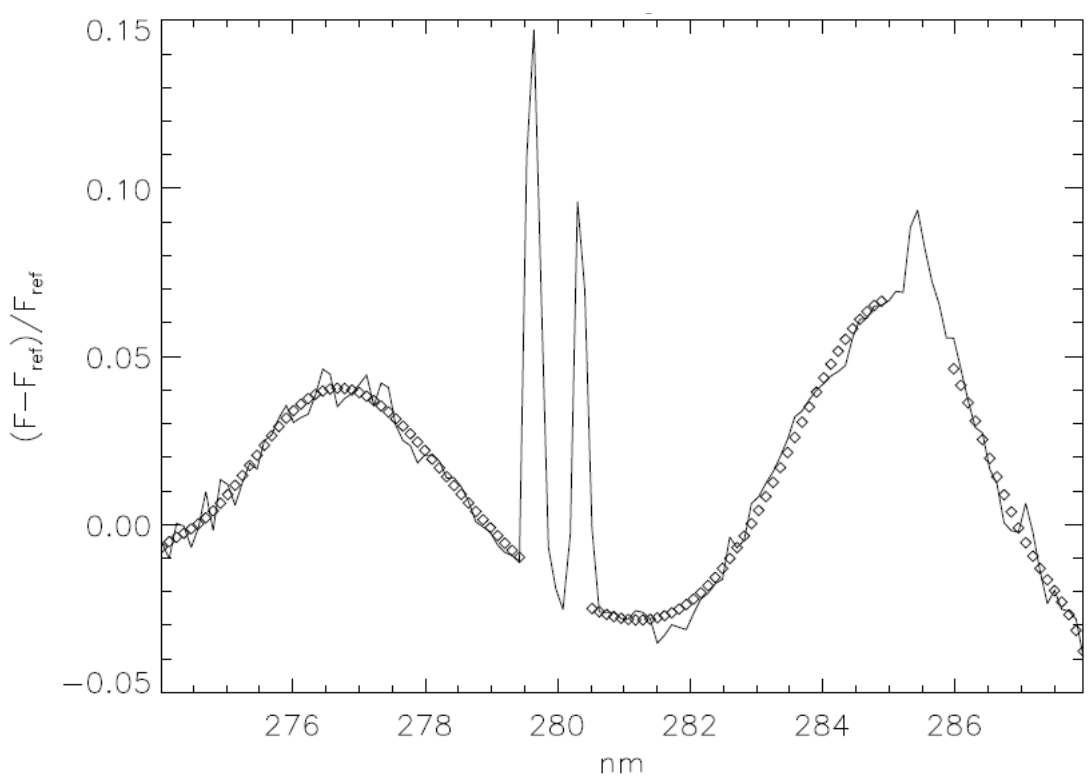

Figure 5. 3: Etalon fiting in channel 1 of GOME, on 1st December, 1998 [Weber, 1999]

5.3 Retrievals of Mg II index

Calibrated data from channel 1 of GOME instrument has been corrected the etalon patterns before calculating the Mg II index. There are two approaches that are used for calculating the Mg II index.

The first one is the classical approach introduced by Heath and Schlesinger in 1986. In this method 7 different points are used; three points at the core and four points at the wings after degrading the spectral resolution to 1.1 nm (similar to SBUV). Figure 5.4 shows the representation of classical approach used for GOME-2. The curved line is the measured solar spectral irradiance and the solid line is its average

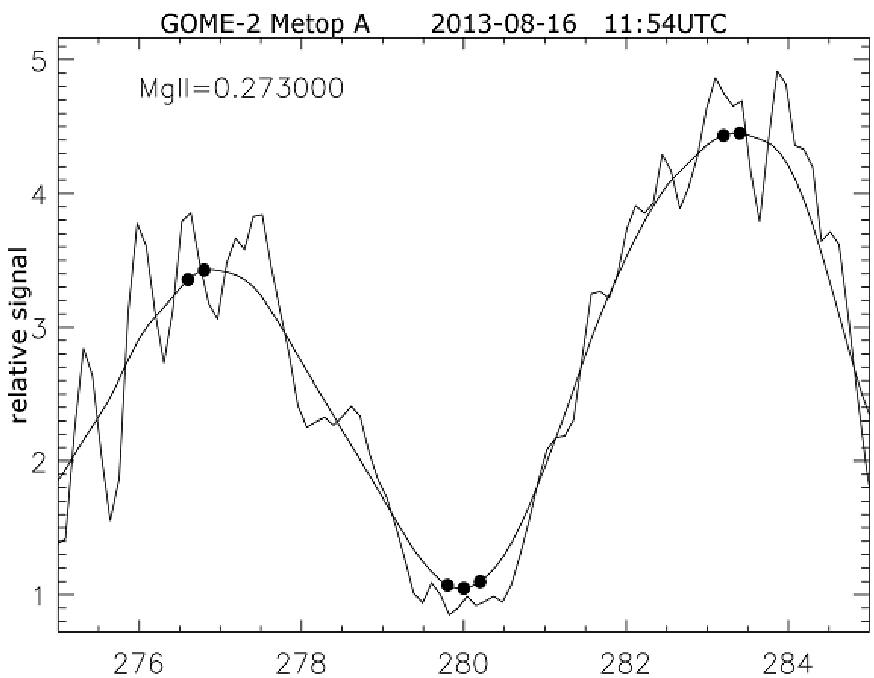

Figure 5.4: Classical approach for Mg II index calculation used for GOME − 2 [Weber, 2013]

For the high spectral resolution Mg II index (without degrading the spectral resolution) wing values are derived by taking the mean of maxima of four parabolas fitted through the following data pixels: 275.79 – 276.23 nm, 276.34 – 276.79 nm, 282.92 – 283.25 nm and 283.69 – 284.12 nm [Weber 1998, Weber, 1999].

The core values are obtained by integrating over a range of 0.2 nm over both emission cores which makes the emission perceptible. High resolution/integration definition is used for GOME and SCIAMACHY (resolved emission cores, no convolution) as shown in Fig. 5.5. It represents measurement while the solar activity was maximum for solar cycle 23, on 24th of September, 2001.

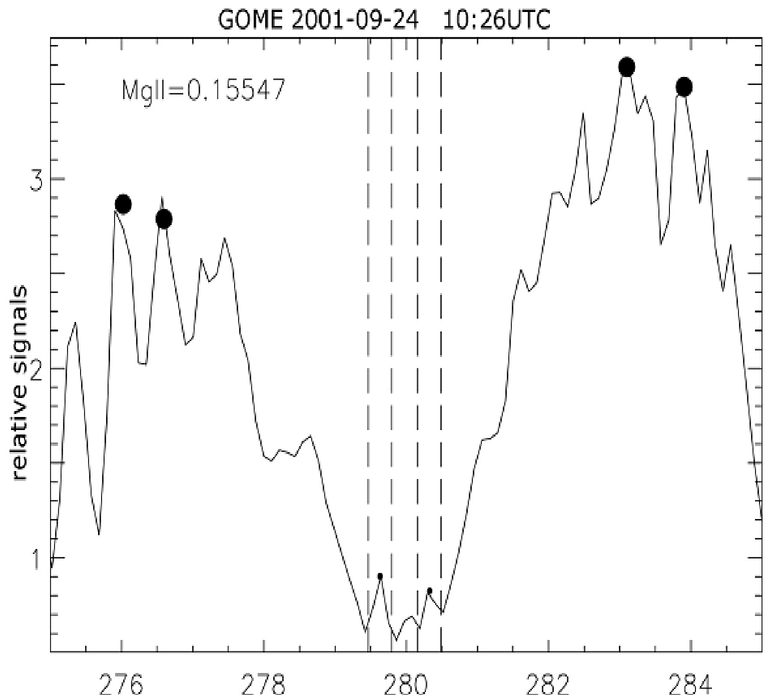

Figure 5. 5: Integration approach used for GOME and SCIAMACHY [Weber, 2013]

The core values are sensitive to the 11 year solar cycle. As discussed before the wing values stay almost constant throughout the 11 year solar cycle. This is shown in Fig. 5.6, where GOME measured the maxima and minima of solar activity in April 2000 and April 2009, respectively. This shows clearly shows the variability in the emission core over a solar cycle.

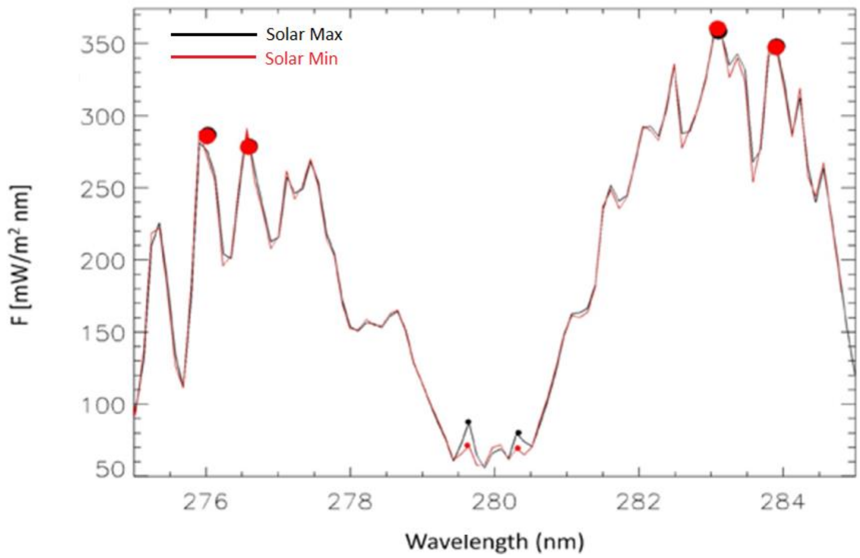

Figure 5.6: GOME observed solar maximum and minimum [IUP Bremen, 2013]

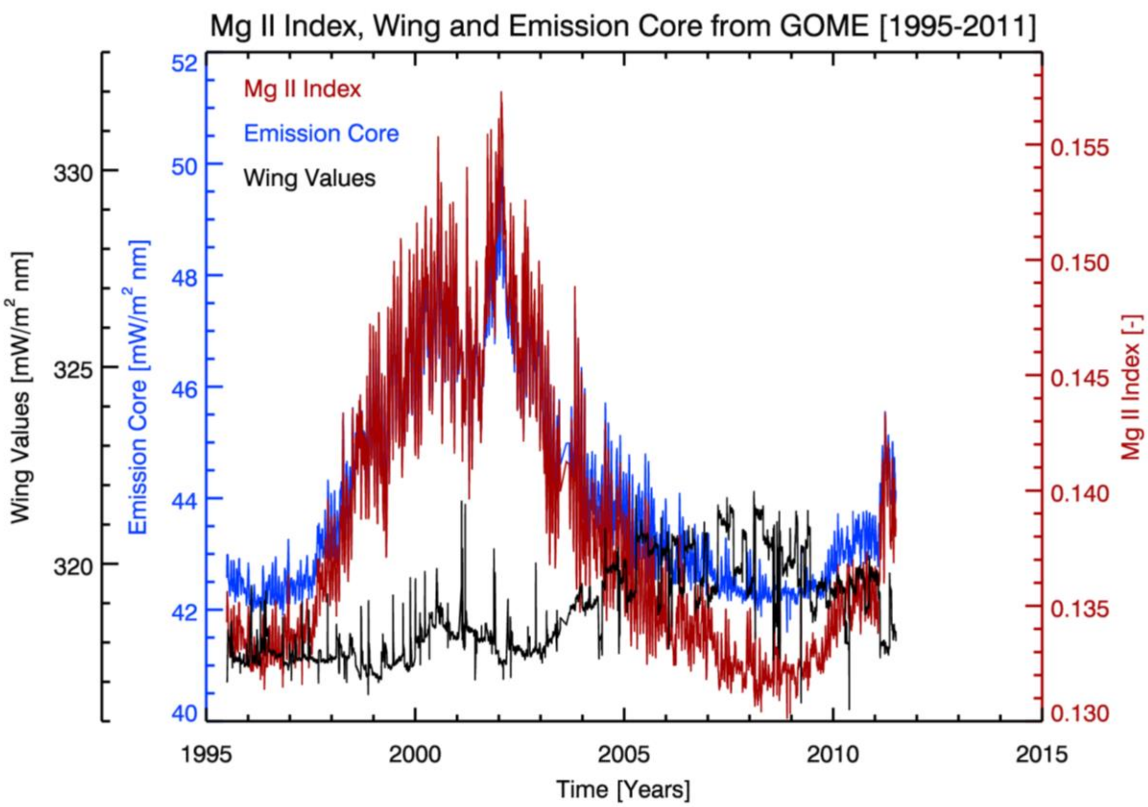

Figure 5.7: GOME Mg II index, wing values and emission core

Figure 5.7 shows the time series of the GOME Mg II index (red) along with the core (blue) and wing values (black). The etalon correction also acts as a degradation correction, where very little change in the wing value is observed. This shows that the variability in the emission core is directly related to the solar cycle. Wing values are supposed to be constant but variability can be sobserved. Changes in the wing values are prominent after 2003 until end of 2009. This is due to the fact that degradation has a significant impact on the wings.

The short term chromspheric emission is linked to sun's 27 day rotation on short time scales and 11 year solar cycle on longer time scales. The SCIAMACHY (2002-2012) and GOME-2 (2007-Present) Mg II index time series are illustrated in Fig. 5.8, changes in the wing values for SCIAMACHY are fairly stable decreasing downwards from the start until the end of the mission. For GOME-2 the wing value slightly increases, however, the changes are small (less than a per mil).

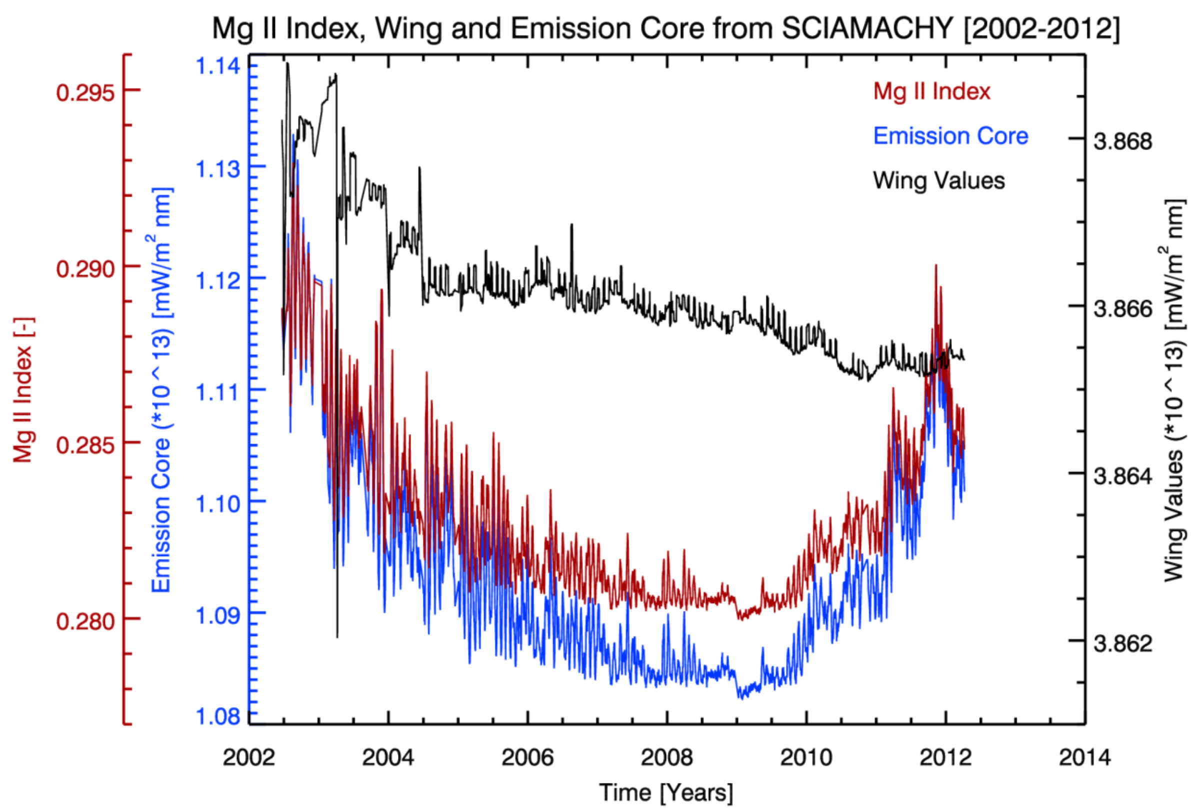

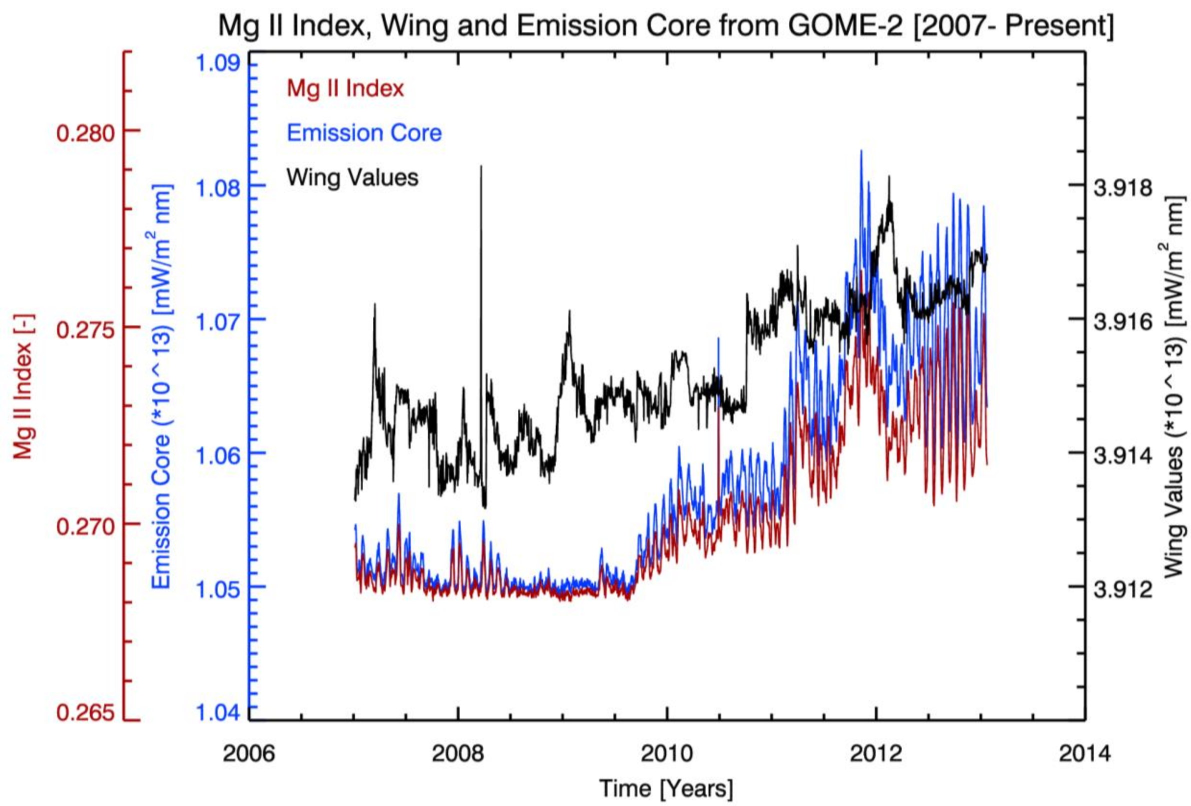

Figure 5.8: Mg II index, wing values and emission core from SCIAMACHY (upper panel) and GOME – 2 (lower panel)

5.4 Error model for the Mg II index

The Mg II index is a ratio of seven different points. The numerator consists of 3 emission core values and the denominator contains 4 wing values. Mathematically it is written as follows:

$$M = \left(\frac{4}{3}\right)\frac{C_{279.8}+C_{280.0}+C_{280.2}}{W_{276.6}+W_{276.8}+W_{283.2}+W_{283.4}} \qquad \text{(C = core values, W = wing values)}$$

$$M = \frac{C}{W} \quad \text{(core to wing ratio)} \qquad \text{------------------------------- (2)}$$

Here, “C” represents the average core emission while “W” the average wing value. The objective is to calculate the error “ΔM” caused by the degradation on the instrument. For this reason, we need to apply the error propagation as follows.

$$\Delta M = \sqrt{\left(\frac{dM}{dC}\right)^2(\Delta C)^2 + \left(\frac{dM}{dW}\right)^2(\Delta W)^2} \qquad \text{------------------------------- (3)}$$

$\frac{dM}{dC} = \frac{1}{W}$ and $\frac{dM}{dW} = -\frac{C}{W^2}$ -- (4)

The equation (3) then becomes:

$$\Delta M = \sqrt{\frac{1}{W^2}\ (\Delta C)^2 + \frac{C^2}{W^4}(\Delta W)^2} \quad \text{-- (5)}$$

$$\Delta M = \frac{1}{W}\sqrt{\ (\Delta C)^2 + \frac{C^2}{W^2}(\Delta W)^2} \quad \text{-- (6)}$$

$$\Delta M = \frac{1}{W}\sqrt{\ (\Delta C)^2 + M^2(\Delta W)^2} \quad \text{-- (7)}$$

Furthermore it is assumed that the noise in the emission core is similar to noise in the wing values.

$\Delta C = \Delta W = \Delta I$

I = signal ΔI = noise in the signal

Equation (7) becomes:

$$\Delta M = \frac{\Delta I}{I}\sqrt{1 + M^2} \quad \text{-- (8)}$$

$\frac{\Delta I}{I} = SNR^{-1}$(t)

As the SNR changes with time, SNR (t) can be expressed as a product of the SNR at the beginning of the mission (and characterized from pre-launch calibration) with a time dependent degradation factor d(t).

SNR (t) = SNR_0 * d(t) -- (9)

SNR_0 = signal to noise ratio at t = t_0

And

d(t) = $\frac{I_{uncorrected}\,(t)}{I_{(t_0)}}$

Equation 9 can be further modified by taking into account four wing values that have been used as background for the Mg II index retrievals, already corrected with etalon and degradation corrections. The square root of the number of points used in the wing values are used to normalize the SNR_0 , in order to enhance the estimation for signal to noise ratio at t = t_0.

SNR_0 (enhanced) = $\frac{\mathrm{SNR}_0}{\sqrt{\text{number of wing values used}}}$ -- (10)

Finally,

$$\mathrm{SNR}^{-1}(\mathrm{t}) = \frac{1}{\mathrm{SNR}_0\,(\text{enhanced}) \, * \, \mathrm{d(t)}}$$

$\Delta\mathrm{M} \ = \mathrm{SNR}^{-1}(\mathrm{t})\sqrt{1 + (\mathrm{M})^2}$ -- (11)

The main purpose here is to estimate the change in errors with time taking into account degradation effects.

Time dependent degradation d(t)

Time degradation d(t) is just a ratio of intensities $\mathrm{I_{uncorrected}}\,(\mathrm{t})/\mathrm{I_{uncorrected}}(\mathrm{t}_0)$ averaged over 276-284 nm . $\mathrm{I_{uncorrected}}(\mathrm{t}_0)$ is the reference intensity of signal at t = t_0. $\mathrm{I_{uncorrected}}\,(\mathrm{t})$ is the intensity t = t_0 (as instrument starts observations). $\mathrm{I_{uncorrected}}\,(\mathrm{t})$ is the time dependent intensity suffering from optical degradation. This ratio is basically identical to the mean etalon correction over the same wavelength interval.

Signal to noise ratio at t = t_0 (SNR_0)

When instrument's electronics are switched off, an electronic signal still exists within the system giving rise to black current. This is the primary reason that noise can be observed at t = t_0 (before launch). SNR_0 (signal to noise ratio at t = t_0) is important to be quantified, in order to estimate the errors present in the measurements. Calibration is implemented here which takes this background signal into account and helps to estimate the noise caused by black current.

The Mg II index is retrieved in the wavelength range of 276-284 nm. This spectral region corresponds to several detectors' pixels. Instrumental precision (as part of the calibration process) help us to calculate the noise linked to every individual pixel. This calculated noise is then averaged for all the pixels in the above mentioned wavelength range. This finally provides the mean SNR_0 (signal to noise ratio at t = t_0).

SNR_0 (enhanced) for GOME, SCIAMACHY and GOME-2

SNR_0 for GOME has been estimated by using GOME SNR precision data from July, 1995 P. Liebing (personal communication). The mean SNR_0 (signal to noise ratio at t = t_0) for GOME was determined to be $1/4.6 * 10^{-4}$. As SNR_0 (enhanced) = $\frac{\mathrm{SNR}_0}{\sqrt{\text{number of wing values used}}}$ is utilized in the simple error calculation model, finally SNR_0 (enhanced) = $\frac{4.6 * 10^{-4}}{\sqrt{4}}$ =$2.3 * 10^{-4}$.

SNR_0 for SCIAMACHY has been estimated by using SNR Errors data provided by P. Liebing (personal communication). The pixel numbers for SCIAMACHY starts from 508 to 560 in 276-284 nm wavelength range. The mean of noise of these pixels is $7.3 * 10^{-4}$. For sun diffuser state the noise is calculated for single read out, but originally there are 200 read outs. The mean of the noise is then normalized by the square root of the number of read outs. The mean SNR_0 (signal to noise ratio at t = t_0) for SCIAMACHY was determined to be $1/5.2 * 10^{-5}$. Using equation 10; SNR_0 (enhanced) = 2.6 $*10^{-5}$.

SNR_0 for GOME-2 has been provided by (R. Lang. personal communication). This estimation is computed while taking wavelength range of 276-284 nm, and pixels corresponding to it. The mean SNR_0 (signal to noise ratio at t = t_0) for GOME-2 was determined to be $1/7.0 * 10^{-4}$. Using equation 10; SNR_0 (enhanced) = 3.5$*\ 10^{-4}$. The simple error calculation model for the Mg II index has been validated with signal to noise ratio provided by the R. Lang (personal communication).

Chapter 6: Results

6.1 Mg II index, solar proxies and filtering

For the validation of the composite Mg II index, three different solar proxies are used in this study, as stated in chapter 3, namely Lyman Alpha, F10.7 cm solar flux and sunspot numbers. By using different techniques, their correlations with the Mg II index have been calculated and very good agreements are found confirming the authenticity and the quality of the Mg II composite index used in this research work. Figure 6.1 depicts the used solar indices spanning 1980 until 2012.

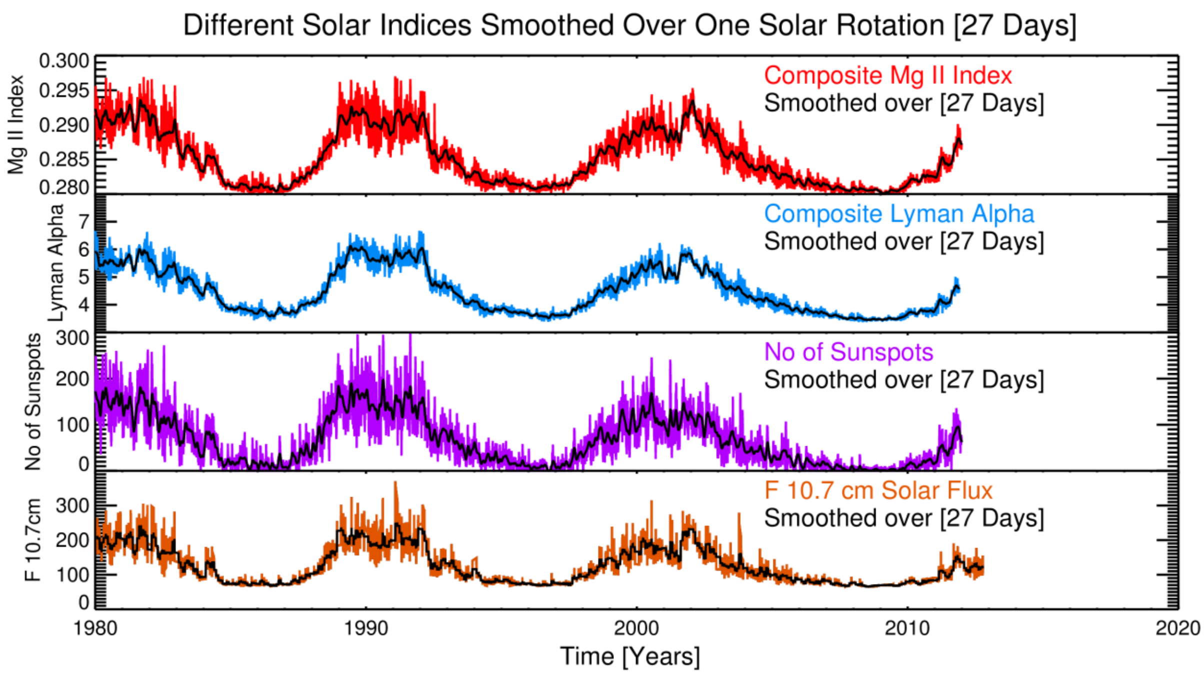

Figure 6. 1: Time series of Daily solar proxies from 1980 until 2012 depicted in different colors.

As clearly seen in the Fig. 6.1, the record of sunspot numbers is densily populated in comparison to the other solar indices because it is an indicator of strong solar photospheric activity. On the other hand all remaining three solar indices shown in the first, second and last panels demonstrate week solar chromospheric activity.

The 27 day rotation (and corresponding beat frequencies like 55 days) leaves a signature in the upper atmosphere as observed in the ozone vertical profile [Dikty et al., 2010]. The low frequency content of the solar proxies is shown in Fig. 6.2 after applying a 55 day triangular smoothing to the time series. Furthermore this simple technique helps to identify when exactly sun activity increases and after completing its duration when it decreases. This information is needed to estimate the length of solar cycle (as it differs from 9 to 12 year) and identify the exact date for solar maximum and minimum which is not possible with daily measurements.

The correlations between the Mg II index and the other solar proxies are very high, i.e., 0.99, 0.98, and 0.97 for F10.7 cm solar flux, Lyman alpha and sunspots, respectively.

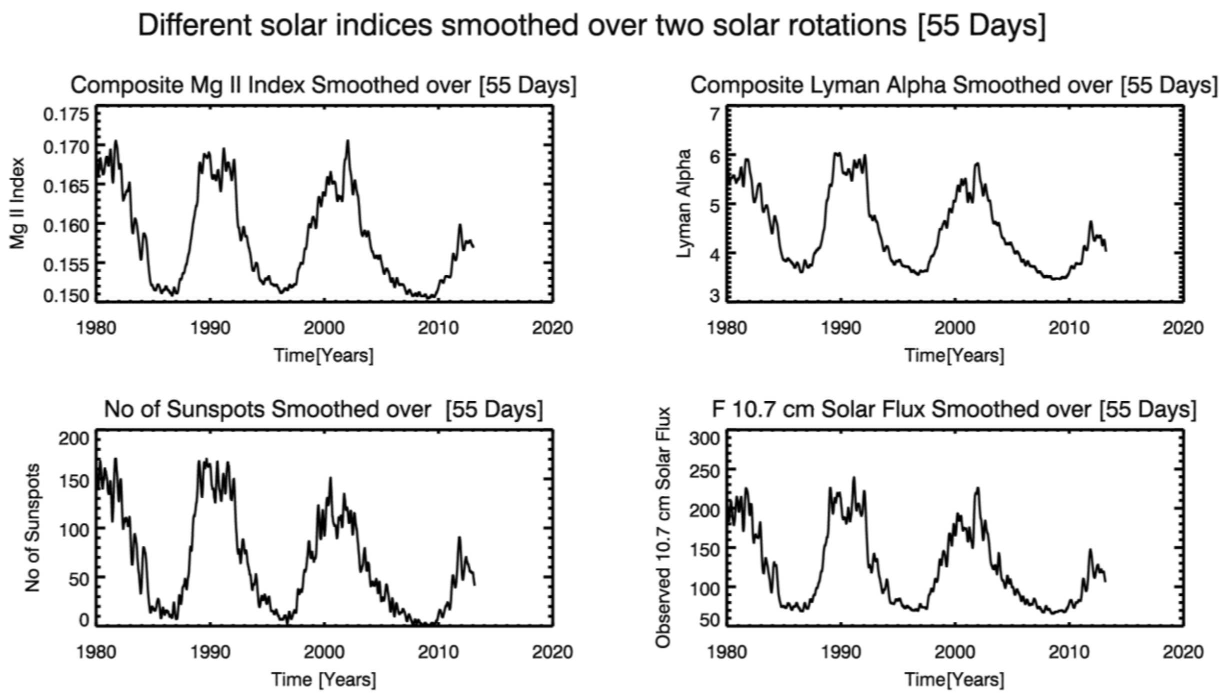

Figure 6. 2: Solar indices smoothed over 55 days (two solar rotations)

The unwanted features in the signals have to be filtered out. This process removes the background signals and places an emphasis on the desired frequency range contained in the time seires, e.g. the 27 day signal enhancing the efficiency of the datasets.

Filtering for all four solar indices has been applied with an emphasis on the short term trends. Figure 6.3 shows the various solar proxies after subtracting the 55 day triangular smoothed time series from the original and highlights the rotational variability dominated by the 27 day signal that is larger during solar maxima.

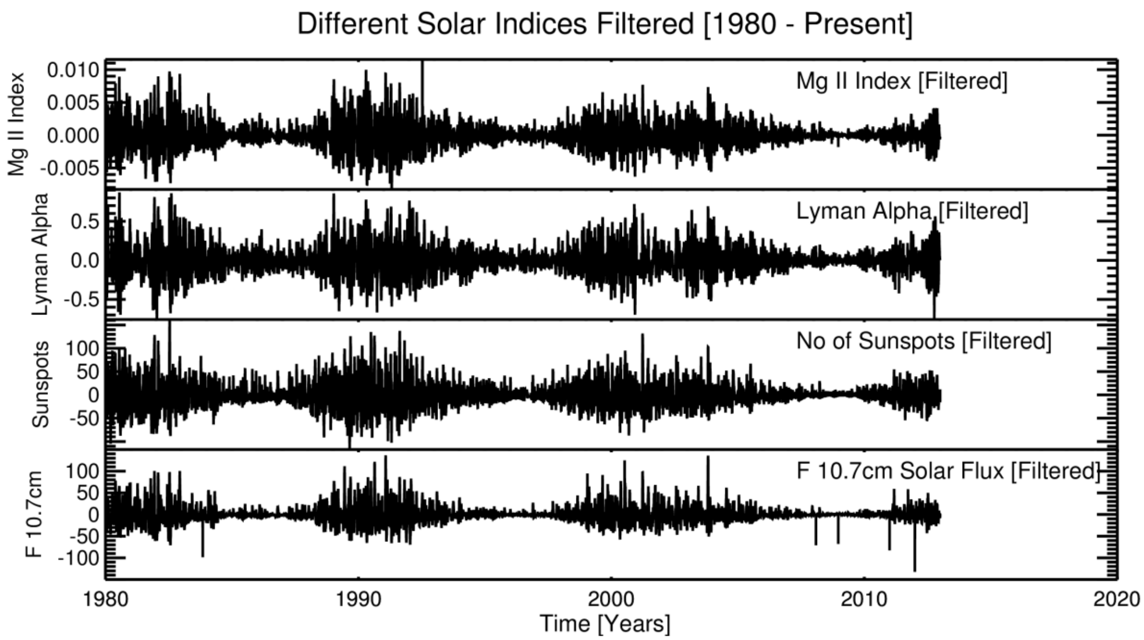

Figure 6. 3: Different solar proxies low frequency filtered

The correlations of the Mg II index with the other solar proxies are listed in Table 6.1. Ooverall the correlations are observed to be very high.

Solar Proxy VS another proxy	Daily measured	27 days averaged	55 days averaged	55 days filtered
Mg II & no of Sunspots	R = 0.925	R = 0.943	R = 0.978	R = 0.715
Mg II & Lyman Alpha	R = 0. 957	R = 0.973	R = 0.986	R = 0.872
Mg II & F 10.7 cm Solar Flux	R = 0.963	R = 0.979	R = 0.991	R = 0.789

Table 6. 1: Correlations between Mg II and various other solar indices

The scatter plots between Mg II index and F 10.7 cm data, the sunspot number and Lyman alpha for the time period 1980-2012 are displayed in Figs. 6.4 and 6.5, respectively.

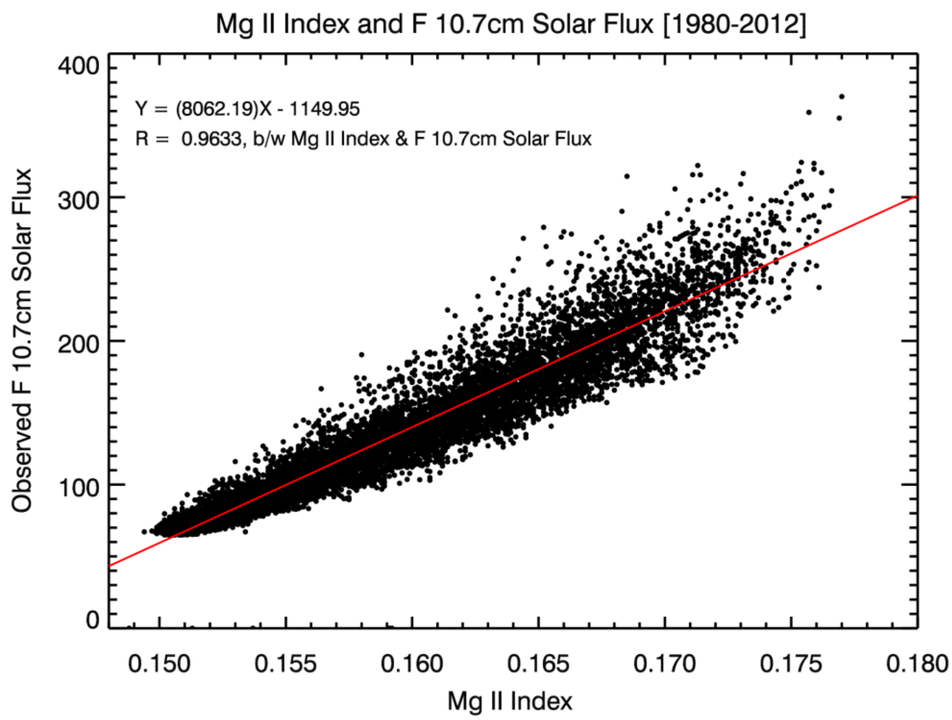

Figure 6.4: Scatter plot between Mg II index and F10.7 cm

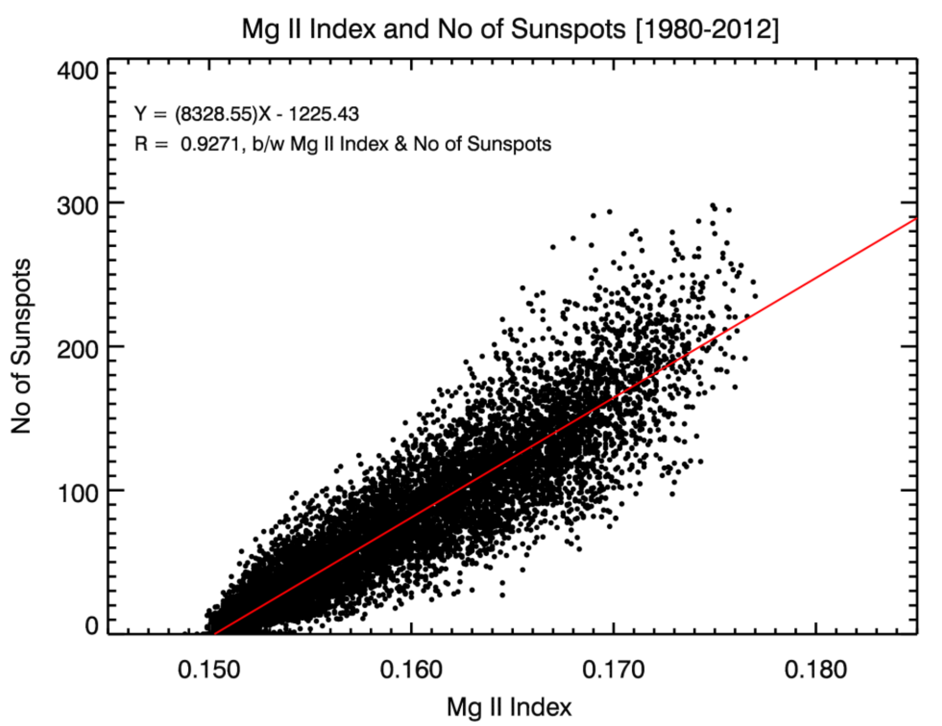

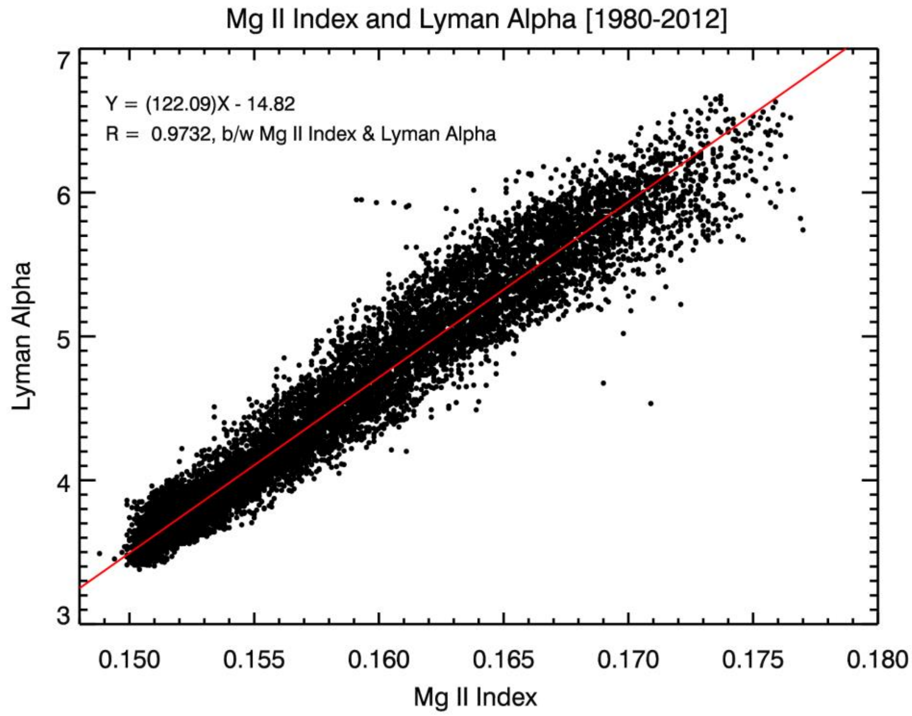

Figure 6. 5: Mg II index and sunspot numbers [above] and Mg II index and Lyman alpha [below]

6.2 Mg II index from GOME, SCIAMACHY and GOME-2

The GOME (1995-2011), SCIAMACHY (2002-2012) and GOME-2 (2007-until today) data provides the later part of composite Mg II index from 1995 until today. All three instruments overlap in time with each other very well enabling us to have a composite index. Figure 6.6 shows the time slots of the Mg II index from GOME, SCIAMACHY and GOME-2 from 1995 until 2013.

GOME started observations in 1995 at the end of solar cycle 22 and the beginning of cycle 23. From 1995 to 1997 the activity remained low and after 1997 it started increasing and the solar cycle 23 reached its maximum just after the start of 2002. Afterwards it reduced down until the end of 2010 and the solar cycle 23 finished, while cycle 24 started and approached the solar maximum. In 2011 GOME instrument stopped measurements after 16 years. In Fig. 6.6 the Mg II index from GOME is represented in the first panel in orange color and the black curve shows the 27 days smoothed signal. In comparison to panel 2 and 3 GOME has the longest time span (16 years).

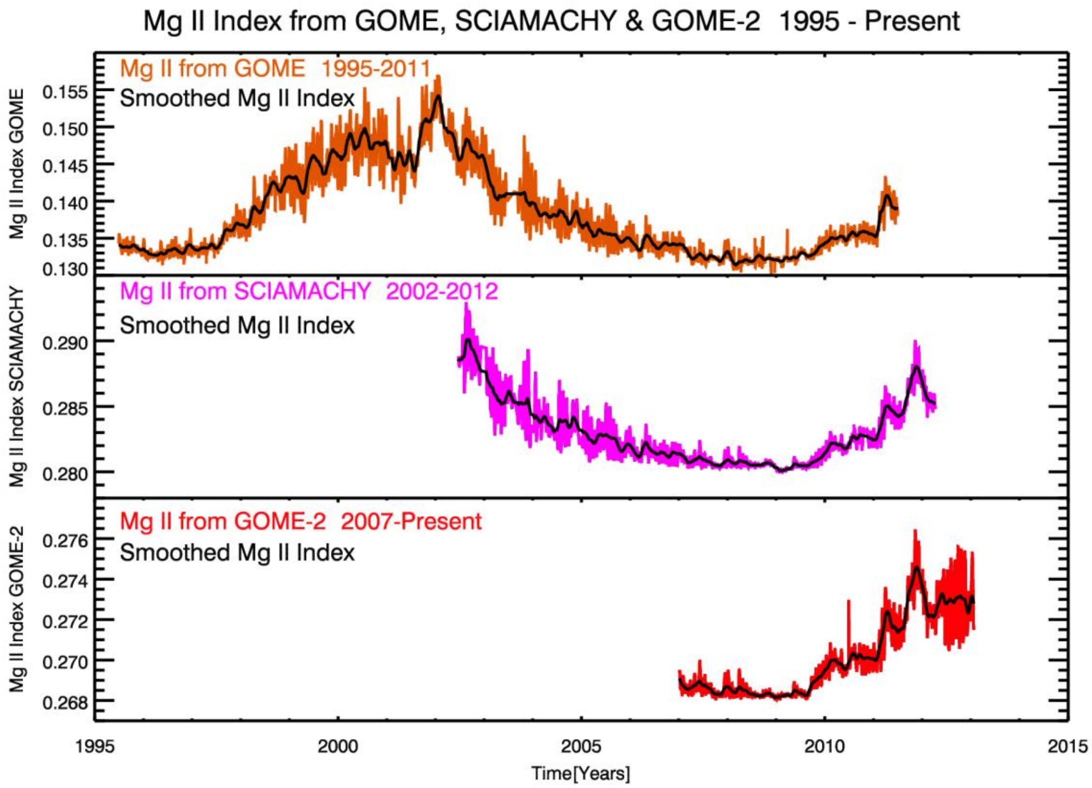

Figure 6.6: Mg II index from GOME, SCIAMACHY and GOME − 2

SCIAMACHY was launched, in 2002 during the maximum activity of solar cycle 23. SCIAMACHY was operational for ten years and there is almost nine years of overlap with GOME, very good agreement for Mg II index has been observed between both instruments for the overlapped years (2002-2011). In addition, some differences are observed towards the end of solar cycle 23; e.g., just after the start of 2009, a sharp spike is observed in Mg II index from GOME while no such sudden increase is witnessed in SCIAMACHY data product. The possible explanation for such a discrepancy is that GOME underwent more optical degradation in its last years.

GOME-2 started observations in 2007 during the minimum activity of solar cycle 23. This instrument is still operational and continuing observations. GOME-2 overlaps not only with GOME from 2007-2011 but also with SCIAMACHY from 2007-2012. Optical degradation apparently affected GOME-2 more in comparison to GOME and SCIAMACHY. The degradation rate for all three instruments will be discussed and compared in the next section. This will help us examining how degradation caused errors in the Mg II index.

6.3 Degradation rate of GOME, SCIAMACHY and GOME-2

The degradation rate d(t) as discussed in chapter 5, are shown in Fig. 6.7 for GOME, SCIAMACHY and GOME-2. Maximum degradation occurred to GOME and minimum occurred to SCIAMACHY. GOME-2 results show the fastest degradation rate. At the end of the GOME and SCIAMACHY missions, the degradation was close to 10% and 80% to the initial values, respectively. GOME-2 degraded up to 70% after six years in space.

This degradation curve varies over time and it quantifies the instrumental performance. In the first four years of GOME (1995-2011) degradation depicted in orange, three sharp spikes are observed due to accidental heating and subsequent cooling of the detector (the spikes after 2000 are due to pointing anomalies). Solar activity increased from 1999 to just before the end of 2001 and reached maxmium for solar cycle 23. Consequently a steep decline has been recorded in the degradation curve dropping from 90% to 50% within these two years. The slope stabalizes from 2001 until mid 2002 as the solar activity stayed at the maximum. From mid 2002 until the mid 2005, the solar activity declined, at this point, the degradation curve drops from 50% to 20% within three years. For the remaining operational time from mid 2005 until 2011, the degradation curve stayed stable and only dropped to 10% in six years.

SCIAMACHY (2002-2012) is an extended design of the GOME instrument. Eventhough SCIAMACHY started observations when solar cycle 23 was at its maximum, very low degradation was recorded (depicted in violet) in comparison to GOME for the same period. SCIAMACHY degraded only 5% from 2002 until 2005, while in the same time period GOME degraded up to 30%. After 2005, a continuous decline in the degradation curve is observed from 2005 to 2009, reducing from 95% to 85% in four years. Right at the beginning of 2009, a sharp decrease is recorded; the possible reason for this decrease is the decontamination of the instrument. Afterwards the degradation curve stabilizes. In early 2010 the degradation curve shows recovery. Possible explanation for this feature is that the power supply mounted on SCIAMACHY accidentally distributed power to all optical systems. This energy distribution helped to overcome the degradation through heating of the optical mirrors [K. Bramstedt personal communication]. This recovery started at the beginning of 2010 until the end of SCIAMACHY mission and recovered degradation from 78% to 83%.

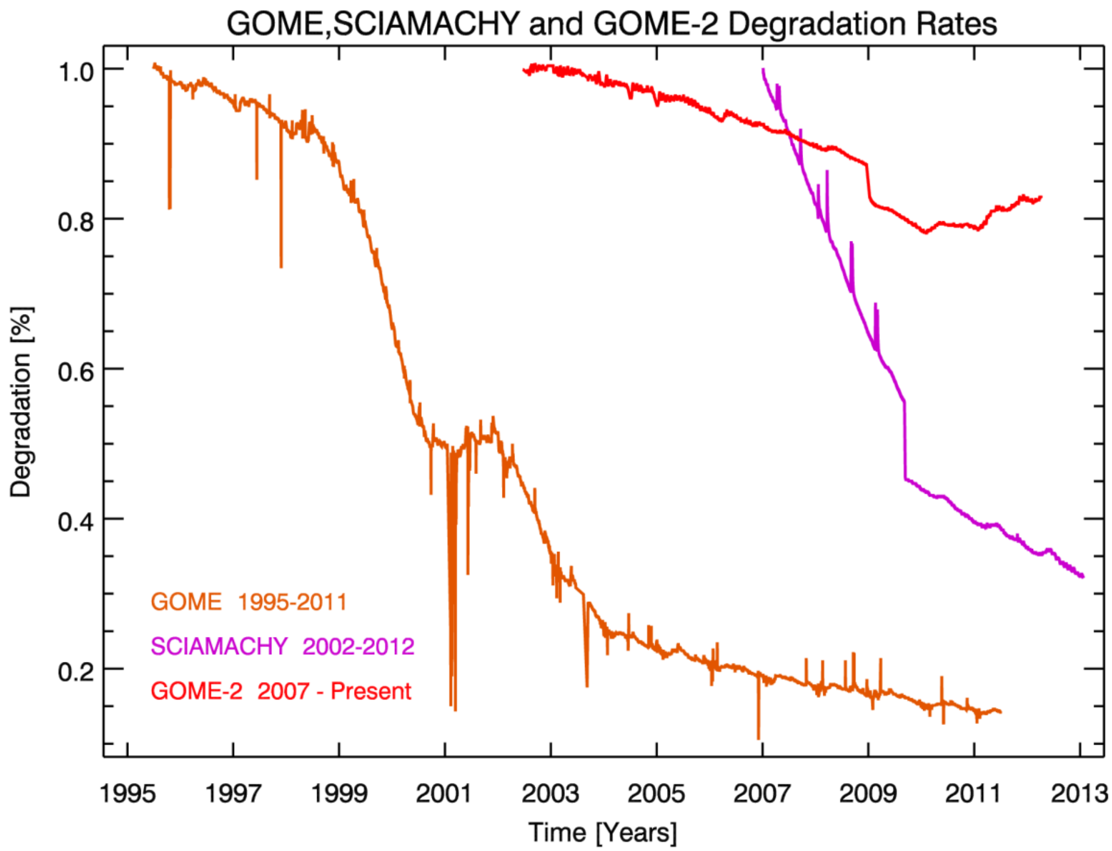

Figure 6.7: Degradation rate, GOME, SCIAMACHY, GOME − 2 in the spectral range of 276 − 284 nm

GOME-2 (2007 - until today) and SCIAMACHY had similar improvements in design. But the GOME-2 degradation curve (depicted in red) behaved strange right from the beginning. In the beginning of the GOME-2 mission, solar activity was minimum but degradation was as strong as for GOME at solar maximum. GOME-2 degradation curve (2007 to 2010) is even steeper than the GOME curve (1999 to 2001). There are no well known explanations available for such a steep decline. Measures were taken in 2010 to counteract the severe degradation which significantly slowed down the degradation rate. The sharp decrease in the curve observed around 2010 shows the technical operations taken to improve degradation. After 2010 degradation rate slowed down. From 2007 to 2010, 55% degradation was observed and from 2010 to 2013 only 13% additional degradation was observed. In the first three years (2007-2010) the degradation was four times stronger than the last three years (2010-2013).

6.4 Simple error model applied to Mg II index

In chapter 5, the error model was discussed. This error model will be now used to estimate the errors caused by optical degradation of GOME, SCIAMACHY and GOME-2.

Error associated to GOME Mg II index (1995 - 2011)

The Mg II index for GOME over the time span 1995-2011 is displayed in black in the upper panel of Fig. 6.8 together with the estimated error at 1-sigma confidence level in orange color, SNR_0 (enhanced) used in this study is $2.3*10^{-4}$, as discussed in Section 5.5. In the beginning (1995 until 1999) solar activity was minimum and correspondingly the Mg II index is fairly low and stable. Beginning of 1999, the increase in the solar activity is prominent. The activity increased until 2002 where the peak in the Mg II index is observed, this represents the maximum of solar cycle 23. Here the degradation is stabilized for a while then followed a decline from 2002 until the mid 2003. A gap in Mg II index can be seen after mid 2003 which recovered after a short time period. This gap was caused by the lost of the tape, which was used to store measurements. Afterwards, the measurements were possible but only when the instrument was exactly on the top of downlink station in the Northern Sweden. This decreased the amount of data received and imposed a possible impact on the quality of data. From mid 2003 until the end of 2008, the Mg II index reached the end of solar cycle 23. Solar cycle 24 started at the beginning of 2009, it stayed mostly stable from 2009 until 2010, moreover in the last year of GOME mission from 2010 until 2011 solar activity started increasing and a small peak is observed. In 2011 the instrument stopped working and an end of the mission was declared.

The estimated error is shown in the middle panel of Fig. 6.8, in the first four years of GOME mission estimated error curve increased linearly. As the solar activity approached the maximum, two prominent spikes are observed in the error curve just after the start of 2001. A small spike is seen at the time of recording tape loss (2003). After 2003, the increase in the slope of error curve is observed due to the fast decontamination to the instrument. The total error estimated is around 17% from 1995-2011.

The degradation rate is shown in the last panel of Fig. 6.8, from 1995 until 1999, only 10% degradation is observed as the solar activity was minimum. There is a deep decline from 1999 until 2001, dragging the bringing the curve from 90% to 50%. This curve stabilizes from 2002 until 2003. Moreover from the beginning of 2003 until the end of 2007, there is second deep decline observed bringing the degradation curve from 50% to 20%. The possible explanation for both declines is sudden decontamination to the instrument caused by the increase in the number of highly energetic particles coming from the sun, as solar activity increases. Last four years (2007 to 2011) degradation is fairly slow decreasing from 80% to 90%.

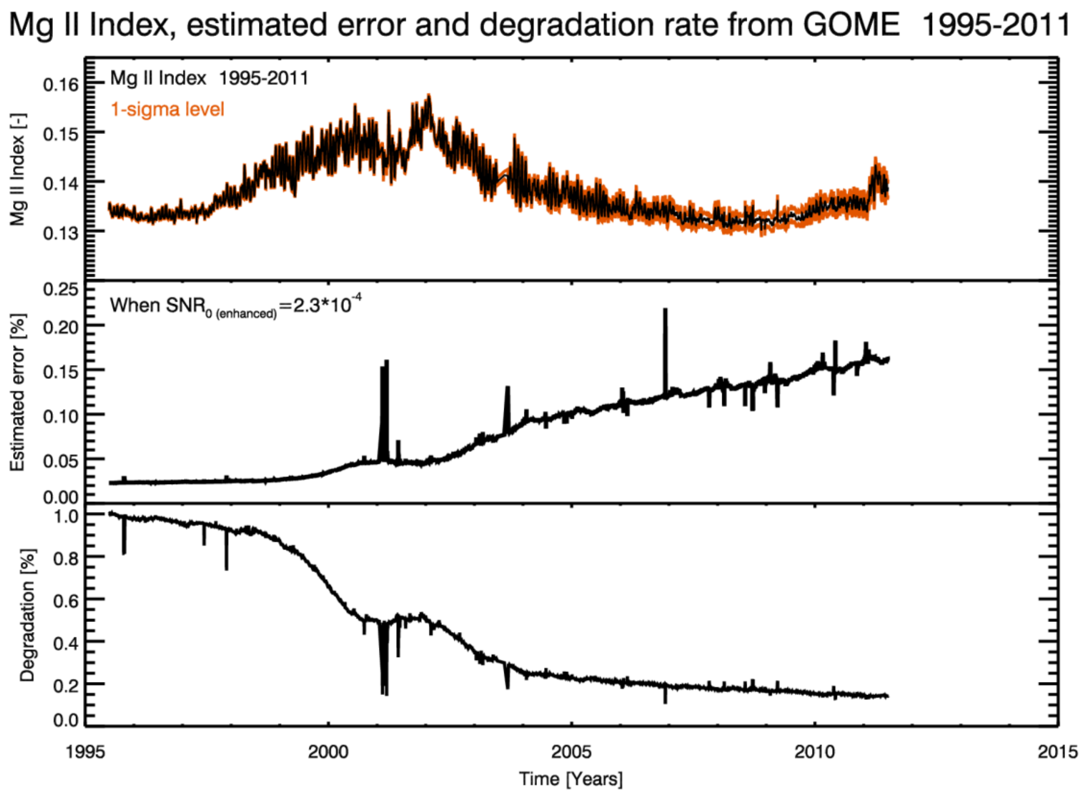

Figure 6.8: Mg II index from GOME, estimated error and degradation rate

GOME covered one and half solar cycles, complete solar cycle 23 and half of 24 from 1995 to 2011 (first panel). Estimated error associated to Mg II index is around 0.17% (middle panel). In 16 years the instrument degraded around 90% (last panel) in the spectral range of 276-284 nm.

Error associated to SCIAMACHY Mg II index (2002 - 2012)

Figure 6.9 shows the results for SCIAMACHY and has the same layout as discussed in Fig. 6.8 with SNR_0 (enhanced) as $2.6*10^{-5}$. In the first panel, it is evident that SCIAMACHY started observations when it was near the solar maximum of solar cycle 23. The peak in the Mg II index is observed after the mid 2002 as solar cycle 23 reaches it maximum. Afterwards the Mg II index descended linearly until the start of 2009. Just after the start of 2009 there is a sudden decline in the Mg II index, this is due to the fact that SCIAMACHY underwent decontamination at which the Mg II index reached its minimum in 10 years of SCIAMACHY mission. After the recovery from the decontamination, from 2009 until the beginning of 2010, the solar activity started to increase towards the maximum of solar cycle 24; this can be clearly seen in top panel of the Fig, 6.9. From 2010 until mid 2011, a peak is observed followed by a decline from mid 2011 until the end of SCIAMACHY mission.

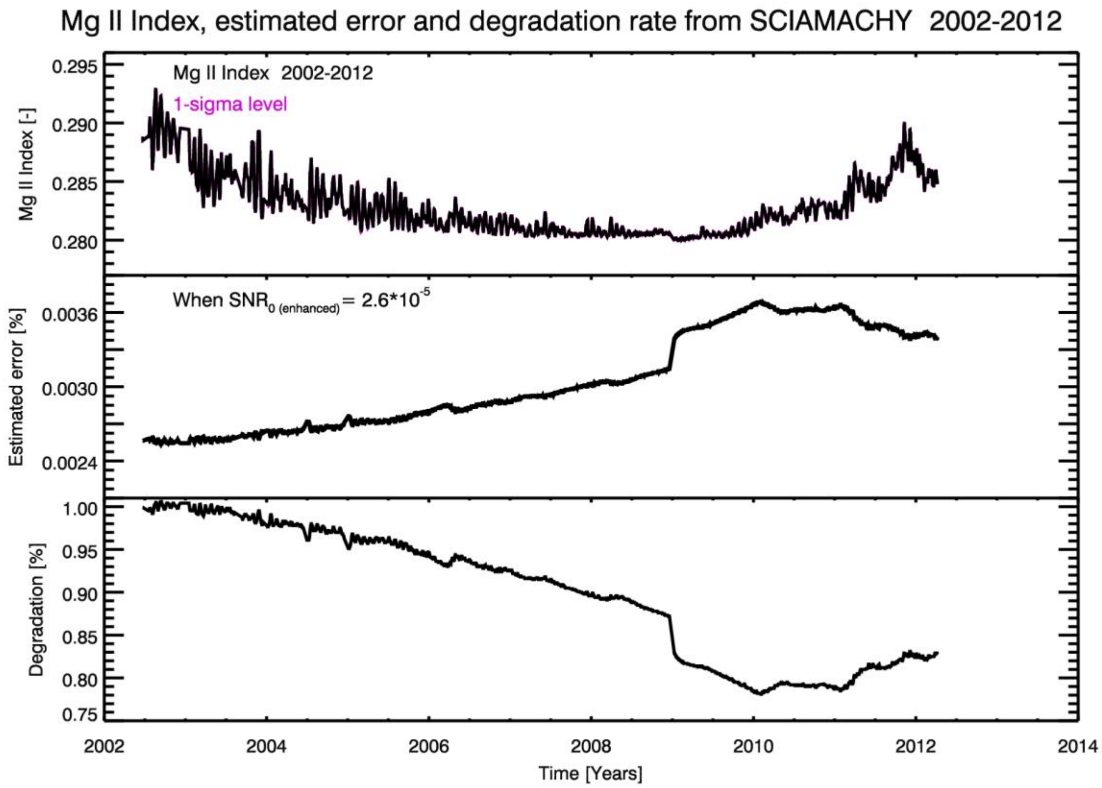

Figure 6.9: Mg II index from SCIAMACHY, estimated error and degradation rate

The estimated error is shown in the middle panel. From the beginning of SCIAMACHY mission until the start of 2009, a smooth increase is observed in the error curve. Just after the start of 2009 a sharp jump is clearly seen in the error curve, as a result of sudden decontamination (discussed in the paragraph above). After 2010 until the end of SCIAMACHY mission, an unusual behavior is observed in the estimated error curve (middle panel) i.e. the decrease in the error estimation curve regardless of increase in the solar activity. The possible explanation for this odd behavior is the energy distribution to the optical components of instrument by the power supply mounted on SCIAMACAHY as discussed in Sec 6.3. From 2002 until 2012, the estimated error for Mg II index is 0.0035%. In 2012 the communication with the instrument was lost and the end of mission was declared.

The degradation rate is displayed in the lower panel, it descends fairly linearly and only 13% of degradation is observed in 8 years from 2002 to 2009. Just after the start of 2009, a deep decline is observed in the degradation rate due to the fact that instrument underwent sudden decontamination, bringing the error curve from 87% down to 83%. Moreover, from the start of

2009 until the end of SCIAMACHY mission a significant recover is observed in the degradation curve as already discussed in Sec 6.3. During its operational years, SCIAMACHY covered half of solar cycle 23 and a little less than half of solar cycle 24 (see first panel), the estimated error associated to Mg II index is around 0.0035% (middle panel). The instrument degraded around 17% (last panel) in the spectral range of 276-284 nm.

Error associated to GOME-2 Mg II index (2007 – Present)

Figure 6.10 shows the results for GOME-2 and has the same layout as discussed in Fig. 6.8 with SNR_0 (enhanced) as $3.5*10^{-4}$. At the beginning of the GOME-2 mission in 2007, solar activity of solar cycle 23 was at the minimum, the corresponding Mg II index is low as can be seen in the first panel. From 2007 until the start of 2010, the Mg II curve is fairly constant. After 2010 changes are seen in the Mg II index and just before the start of 2012, it reached the highest peak in six operational years of GOME-2. From 2007 to 2013 (still operating), GOME-2 covered less than half of solar cycle 24.

In the middle panel, the estimated error is shown. Right after the launch, an inclination was observed in the error curve. From 2007 until mid 2009, the estimated error curve increased from 0.035% to 0.075% in just less than three years. This fast increase in the estimated error is due to the fact that the instrument suffered from severe degradation. After the degradation phase in late 2009, the estimated error sharply decreases (as the degradation enhances), however the increase of the error with time is slowed down (from 2010 until present the error increases from 0.080% to 0.12%).

Right after the launch, a sudden and deep decline is observed in the degradation curve (last panel) owing to the unexpected degradation. The slope of the degradation curve, from 2007 until mid of 2009 (before the sudden jump), shows the fastest degradation rate among all three instruments GOME, SCIAMACHY and GOME-2. From 2007 until mid 2009, 45% degradation was recorded and from mid 2009 until 2013 (after the degradation phase) only 25% was observed.

From 2007 to 2013, GOME-2 covered a little less than half of solar cycle 24 (first panel). Estimated error associated to Mg II index is observed to be around 0.12% (middle panel). The instrument degraded around 70% (last panel) in the spectral range of 276-284 nm.

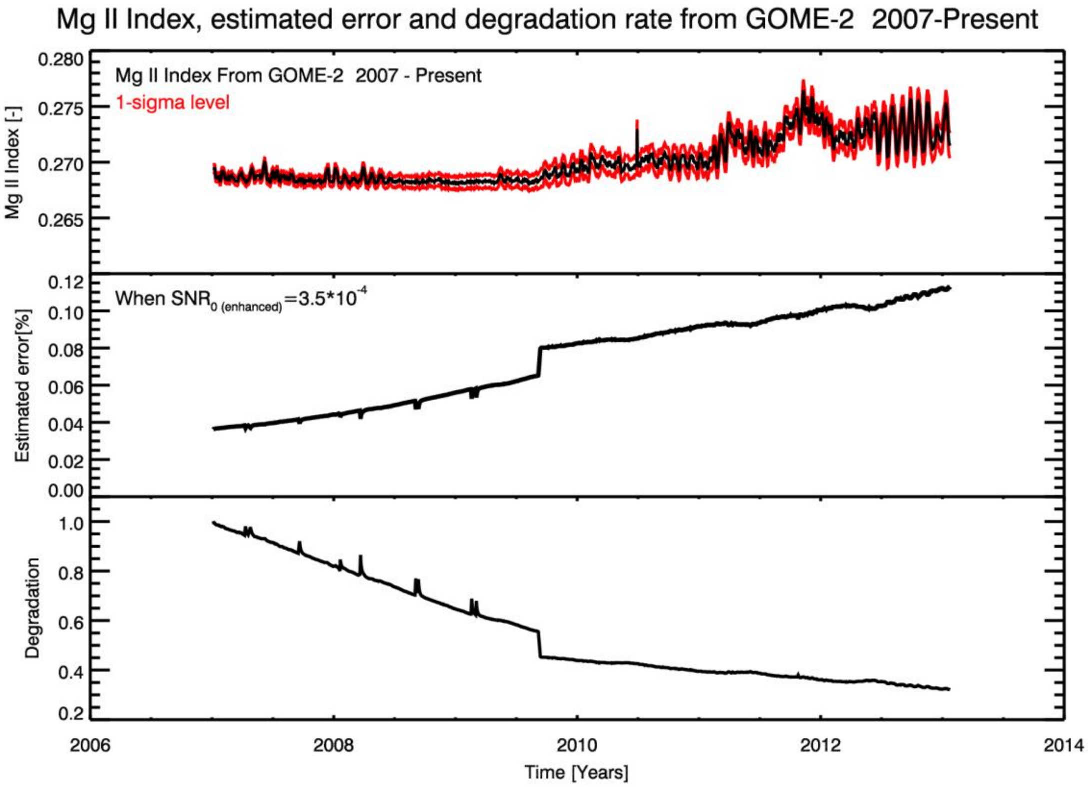

Figure 6.10: Mg II index from GOME − 2, estimated error and degradation rate

The summary plot of the Mg II indices of the three instruments and their associated errors are shown in Fig. 6.11.

The top, middle and lower panels in Fig 6.11 display the Mg II indices and 1 sigma confidence level, from GOME (1995 - 2011), SCIAMACHY (2002 - 2012) and GOME-2 (2007 – Present), respectively. All of the instruments operated in different time slots that overlapped each other quite well enabling us to compare the Mg II indices.

From 2002 until 2009, a very good agreement is observed between GOME and SCIAMACHY. At the start of 2009, a small isolated peak is observed in GOME Mg II index (first panel), whereas no such a peak exists at same time period in SCIAMACHY (middle panel). Similarly, for GOME-2 (lower panel) the Mg II index has no such peak.

When SCIAMACHY and GOME-2 (middle and lower panels) are compared, an isolated peak in the GOME-2 Mg II index seems to appear in the middle of 2010. Such a peak is not evident in

GOME and SCIAMACHY (first and middle panel). The observed differences may be due to the systematic errors which were not taken into account in our error estimates.

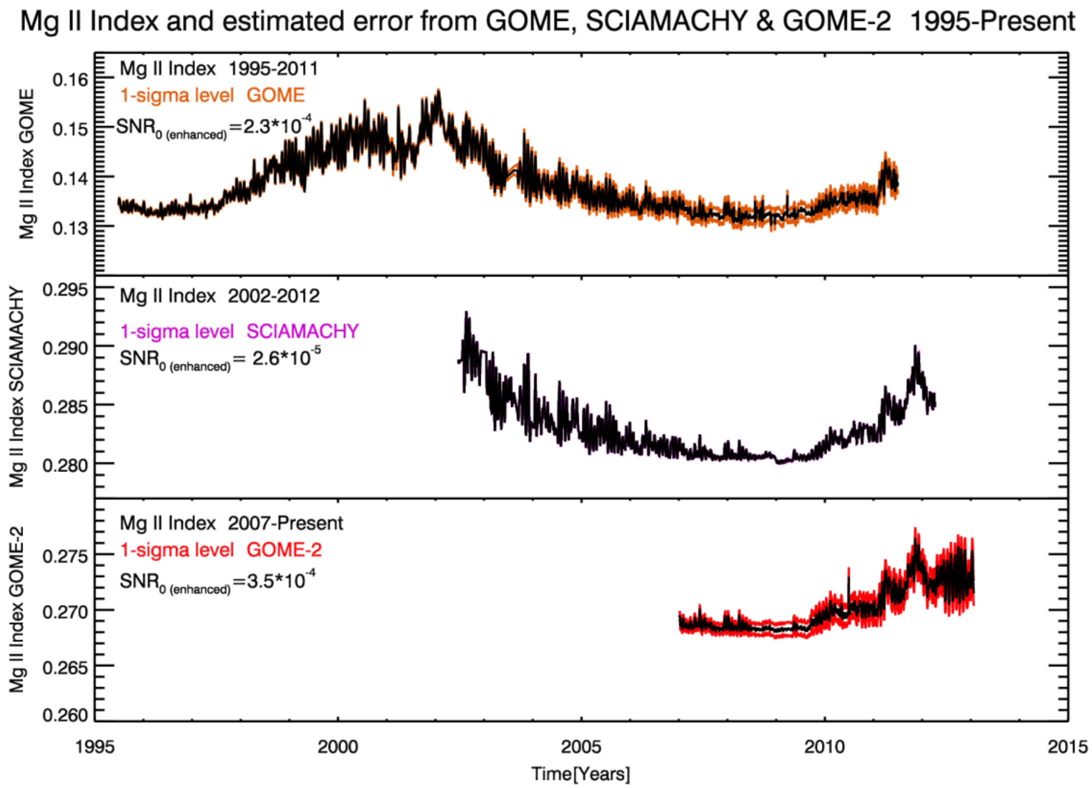

Figure 6.11: Composite of Mg II index obtained GOME, SCIAMACHY and GOME − 2 with the statistical error at 1-sigma confidence level

6.5 Validation of GOME-2 results

Figure 6.12 shows both the estimated error (in blue) and the calculated SNR (in red) for GOME-2. The SNR at the beginning of observation (t_0) for our model, used here is taken from the calculated SNR provided by EUMETSAT. The SNR_0 (enhanced) is not used here to keep the same starting point for both quantities. The SNR at t_0 is 7.0*10^{-4}. The spikes observed in calculated SNR is due to the fact that the change in the earth-sun distance is not taken into account. In general, the datasets are in good agreement. The correlation coefficient between the two is 0.95

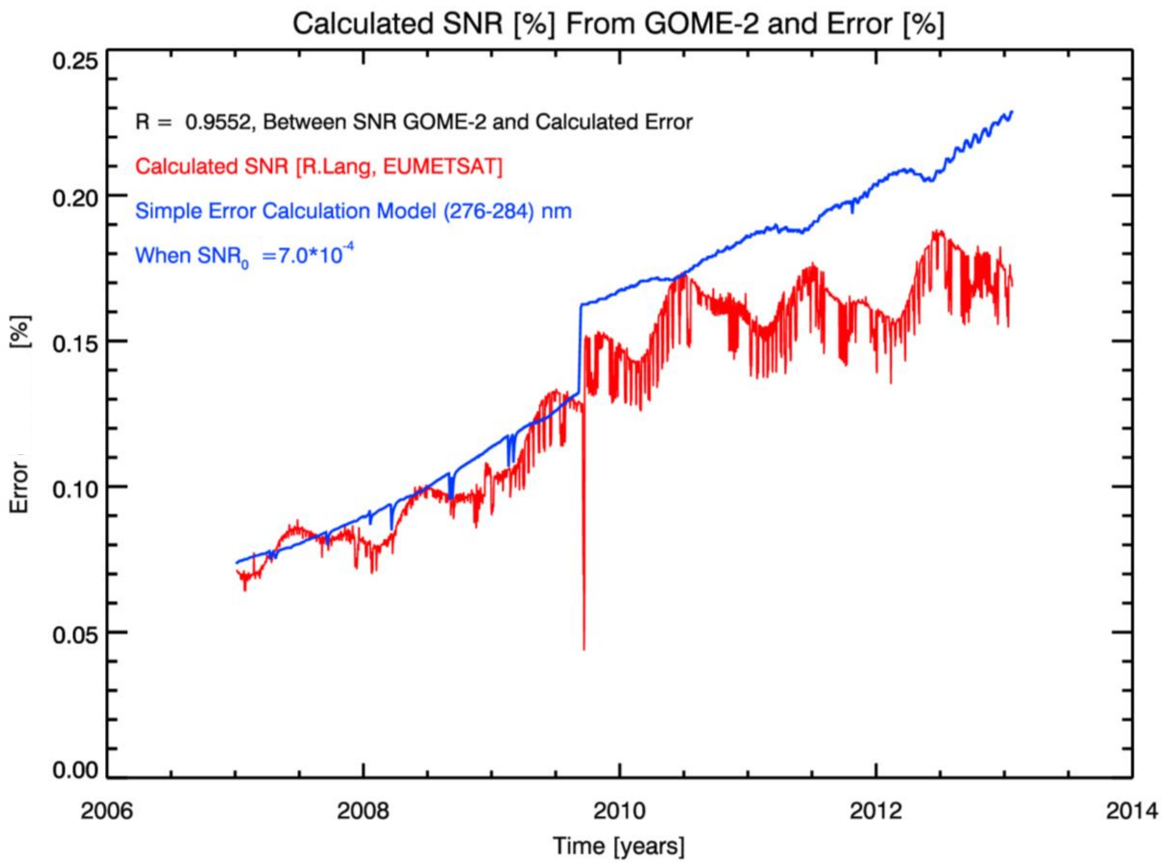

Figure 6. 12: Calculated degradation error by using our simple model and signal to nosie ratio provided by EUMESAT for GOME − 2

The presented validation authenticates the quality of the model used in this research work for GOME-2.

The GOME and SCIAMACHY results are not validated in this study because of lack of daily measured SNR that is a prerequisite for the validation process.

Chapter 7: Conclusions and Outlook:

7.1 Summary and Discussions

It is fundamentally important to enhance the knowledge about the solar terrestrial relation. The Mg II index is an important solar proxy that describes the 11 year solar cycle variability in UV solar irradiance. This work documents the error analysis of the Mg II index from GOME, SCIAMACHY and GOME-2 in the time span from 1995 to 2013.

To summarize, the simple error model that has been developed in this study and implemented on the Mg II indices from the above mentioned instruments. Mg II index retrievals (not part of this thesis work) were performed by using a combined etalon and degradation correction before calculating the index. These corrections were performed by fitting high order polynomials to intensity ratios. This optimal combination of fit parameters finally provides the Mg II index. From the three Mg Index time series (GOME, SCIAMACHY, and GOME-2) and by incorporating other satellite instruments a composite Mg II index can be derived. This composite Mg II index correlates very well with sunspot numbers, F10.7 cm solar flux and Lyman alpha (different correlation and filtering tests have been successfully applied). Very good agreements have been found: Mg II index and sunspot numbers have correlation coefficient of 0.92, Mg II index and F 10.7 cm with 0.96, Mg II index and Lyman alpha have 0.97.

A simple error model has been developed that takes into account the initial SNR at the start of the mission and the degradation of the instruments over time. This model has been applied to GOME Mg II index. GOME covered one and half solar cycles from 1995 until 2011. At the beginning of GOME mission, the SNR_0 (enhanced) with the value of $2.3*10^{-4}$ is used in the error model instead of the initial SNR. This yielded the maximum estimated error associated to Mg II index of 0.17%. The instrument degraded around 90%, which is the maximum degradation observed among all three instruments.

In the same way this model has been applied to SCIAMACHY Mg II index. SCIAMACHY covered 10 years from 2002 until 2012. For SCIAMACHY the SNR_0 (enhanced) of $2.6*10^{-5}$ has been used in the error model and gave the maximum estimated error associated to Mg II index of 0.0035%. The instrument degraded around 17%, which is the minimum degradation among all three instruments.

The model was applied on GOME-2 Mg II index. GOME-2 started observations in 2007 and it is still operational. For GOME-2 the SNR_0 (enhanced) with the value of $3.5*10^{-4}$ has been used in the error model and provided the maximum estimated error associated to Mg II index as 0.12%. The instrument degraded around 70% which is the fastest degradation rate among all three instruments.

The estimated error for GOME-2 Mg II index has been validated with the measured signal to noise time series from EUMESAT. Very good agreement was found between results of the simple error model, developed and implemented in this study, and the SNR time series. This confirms the good quality of tour results. Consequently, this error calculation model is shown to be adequate to address the degradation that is the main cause of uncertainties in the Mg II index retrievals.

7.2 Outlook

The presented study has given an error analysis for GOME, SCIAMACHY and GOME-2. The simple error calculation model has only taken in account the random errors (caused by degradation). This model can be further improved by evaluating and taking systematic errors into consideration. A systematic error which is constant in time is called a bias. A systematic error which changes over time is called the drift. Drift and bias quantification can help to further improve the error model. Nevertheless, the new error model introduced here provides a reasonable estimate of the long-term stability of the Mg II index time series.

The GOME and SCIAMACHY lack of daily measured SNR that is a prerequisite for the validation process. In order to validate their results, a detailed analysis of SNR should be performed as a first step for both spectrometers

References:

Anderson, G., and Hall, L., **Instrumental effects on a proposed Mg II index Solar Activity,** *Annales Geophysicae* ., 5, pp. 531-534, 1988.

Armstrong, W., **The Solar Spectrum,** retrieved March 11, 2013, from: http://dwarmstr.blogspot.de/2006/03/solar-spectrum-magnesium-green.html, 2006.

Bandyopadhyay, P., **Nuclear Data Center Japan atomic Energy Agency**, retrieved March 2, 2013, from Periodic Tables of the Elements: from: http://csrri.iit.edu/cgi-bin/period-form?ener=&name=Mg, 2013.

Barnes, J. E., **The Sun as a Star**, retrieved Feburary 22, 2013, from The Face of the Sun, from: http://www.ifa.hawaii.edu/~barnes/ast110_06/tsaas.html, 2006.

Benestad, R. E., **Solar Activity and Earth's Climate**, In R. E. Benestad, *Solar Activity and Earth's Climate* (pp. 27-95), Berlin: Praxis Publishing Ltd 2002.

Bovensmann, H., Burrows, J. P., Buchwitz, M., Frerick, J., Noel, S., Rozanov, V. V., Chance, K. V., and Goede, A. P. H., **SCIAMACHY: Mission Objectives and Measurement Modes**, *J. Atmos. Sci., 56,* 127–150, 1999.

Burrows, J. P., and K. V. Chance, **GOME and SCIAMACHY:The scientific objectives, optical methods in atmospheric chemistry.** *Proc. SPIE,*1715**,** 562–573, 1993.

Burrows, J. P., Holzle, E., Goede, A. P. H., Visser, H., and Fricke, W, **SCIAMACHY – Scanning Imaging Absorption Spectrometer for Atmospheric Chartography**, *Acta Astronautica, 35(7),*445–451, 1995.

Burrows, J.P., Weber, M., Buchwitz, M., Rozanov, V., Ladstätter-Weißenmayer, A., Richter, A., DeBeek, R., Hoogen, R., Bramstedt, R., Eichmann, K., Eisinger, M., Perner, D, **The Global Ozone Monitoring Experiment (GOME): Mission Concept and First Scientific Results,** J. Atmos. Sci. 56., PP 151-176, doi: 10.1175/1520-0469(1999)056<0151:TGOMEG>2.0.CO;2., 1999.

Catanzaro, E., Murphy, G.T., and William, R., **Absolute Isotopic Abundance Ratios and Atomic Weight of Magnesium,** J. Res. NBS. A Phys Ch., pp. 453-459, 1966.

Coffey, J., **Universe today,** retrieved March 2, 2013, from: http://www.universetoday.com/80696/fraunhofer-lines/, 2010.

Cebula, R. P., DeLand, M. T., and Schlesinger, B. M., **Estimates of Solar Variability Using the SBUV/2 Mg II Index from the NOAA-9 Satellite,** *J. Geophys. Res. 97,* 11613-11620, 1992.

Cebula, R. P., **COMPOSITE Mg II INDEX and SCALING FACTORS DATASETS**, retrieved March 12, 2013, from Brief Description: from ftp://ftp.ngdc.noaa.gov/STP/SOLAR_DATA/SOLAR_UV/UVCOMPOSITE/composit.txt, 1995.

Cersat, **ERS-2 Discription,** retrieved August 13, 2013, from Cersat fremer: from http://projets.ifremer.fr/cersat/Information/Satellites/Polar-orbiting-satellites/ERS-2, 2005.

DeLand, M. T., and Cebula, R. P., **Composite Mg II Solar Activity Index for Solar Cycles 21 and 22,** *J. Geophys. Res. 98,* 12809-12823, 1993.

De Toma, G., White, R., Knap, G., Rottman, B., and Thomas, N., **Mg II core-to-wing index Comparison of BUV2 and SOLSTICE time series,** J. Geophys. Res., pp. 2597-2610, 1997.

Dikpati, M. G., Toma, D., and Gilman, P., **Predicting the strength of solar cycle 24 using a flux-transport dynamo-based tool,** J. Geophys. Res., 33, L05102, doi:10.1029/2005GL025221, 2006.

Dikty, S., Weber, M., Savigny, C., Sonkaew, T., Rozanov A., and Burrows J. P., (2010), **Modulations of the 27-day solar cycle signal in stratospheric ozone from SCIAMACHY (2002-2008),** J. Geophys. Res., 115, D00I15, doi:10.1029/2009JD012379, 2010.

GOME Users Manual (1995) **- Users Manual, SP-1182,** Issue 1, September 1995.

Haigh, J. D., **The Sun and the Earth's Climate,** retrieved March 1, 2013, from solar cycle signal in stratospheric ozone: from : http://solarphysics.livingreviews.org/Articles/lrsp-2007-2/articlesu11.html, 2007.

Hathaway, D., Wilson, M., and Reichmann, J., **The Shape of the sunspot cycle**, *Sol Phys 151*, pp. 177-190, 1994.

Hathaway, D., **Solar Physics,** and retrieved March 4, 2013, from solar cycle predictions: from http://solarscience.msfc.nasa.gov/predict.shtml, 2013.

Hathaway, D., **Solar Physics,** retrieved January 24, 2013, from Marshall Space Flight Center: from: http://solarscience.msfc.nasa.gov/images/Dalsgaard1_density_vs_r.jpg, 2012.

Hathaway, D., **the Solar Cycle,** *Living Rev. Solar Phys.* 7, pp. 5-65, 2010.

Heath, D. F., and Schlesinger, B. M., **The Mg 280-nm Doublet as a Monitor of Changes in the Solar Ultraviolet Irradiance,** *J. Geophys. Res. 91*, 8672-8682, 1986.

Humlum, O., **Laboratory for Atmospheric and Space Physics,** retrieved February 28, 2013, from: Solar activity: http://www.climate4you.com/Sun.htm#Recent solar irradiance, 2007.

IPCC, **Working Group I Home,** retrieved January 12, 2013, from IPCC Fourth Report: Climate Change 2007: from: http://www.ipcc.ch/publications_and_data/ar4/wg1/en/ch1s1-4-3.html, 2007.

IUP Bremen., retrieved August 22, 2013, **IUP Bremen,** from: http://www.iup.uni-bremen.de/PEP_master_thesis/thesis_2010/thesis_shakeri.pdf, 2013.

Jefferson, T., **ORACLE ThinkQuest Education Foundation,** retrieved January 22, 2013, from Nuclear Fusion: http://library.thinkquest.org/3471/fusion.html, 2011.

Kramer, H.J., **eo Portal Directory,** retrieved February 28, 2013, from: https://directory.eoportal.org/web/eoportal/satellite-missions/m/metop, 2013.

Lean, J., David, R., **Climate Forcing by Changing Solar Radiation**, J CLIMATE, pp. 3069-3094, 1998.

Lean. J., **NASA Science,** retrieved March 1, 2013, from Science News: from: http://science.nasa.gov/science-news/science-at-nasa/images/sunbathing/sunspectrum/, 2010.

Liou., **An Introduction to Atmospheric Radiation**. London: Academic press, 2002.

Lockwood, M., **UV spectral solar irradiance lower, during the recent low sunspot minimum? ,** J. Geophys. Res., 116, D00I16, dOI: 10.1029/2010JD014746,, pp. 1-11, 2011.

Morsink, S., **Astronomy of Stars and Galaxies,** retrieved 2 February, 2013, from The Sun's Photosphere & Chromospheres from :http://www.ualberta.ca/~pogosyan/teaching/ASTRO_122/lect9/lecture9.html#limb, 2011.

Naoj Solar Observatory., **Solar Observatory NAOJ,** retrieved February 20, 2013, from Gallery of Solar Images & Movies: from : http://solarwww.mtk.nao.ac.jp/en/gallery.html, 2012.

NASA., **Astronomical Symbol for the Sun,** retrieved February 1, 2013, from The Sun: from http://www.uni.edu/morgans/astro/course/Notes/section2/new5.html, 2012.

NOAA., **National Oceanic and Atmospheric Administration**, retrieved August 27, 2013, from Accuracy VS Precision: from :http://celebrating200years.noaa.gov/magazine/tct/tct_side1.html, 2013.

Noël, S., retrieved August 15, 2013, from **IUP Bremen / SCIAMACHY,** from :http://www.iup.uni-bremen.de/sciamachy, 2001.

Noël, S., Mieruch, S., Bovensmann H., and Burrows, J.P., **Preliminary results of GOME-2 water vapour retrievals and first applications in polar regions,** *Atmos. Chem. Phys.*, 8, 1519-1529, 2008.

Pagaran, J., Weber, M., DeLand, M.T., Floyd, L.E., Burrows J.P., **Solar Spectral Irradiance Variations in 240 – 1600nm During the Recent Solar Cycles 21 – 23,** *Springer Science+Business Media B.V. 2011,* pp. 159-188, 2011.

Peeters, P., Simon, P.C., Rottman, G.J., and Woods, T.N., **UARS SOLSTICE Data as a calibration and validation of GOME, in GOME Geophysical Validation Campaign**, ESA WPP-108, pp. 75-83, 1996.

Peeters, P., Simon, P.C., White, O.R., Toma, G.D., Rottman G.J., Woods, T.N., and Knapp, B.G., **Mg II core-to-wing solar index from high resolution GOME data,** retrieved August 14, 2013, from ESA: http://earth.esa.int/workshops/ers97/papers/peeters3/, 1997.

Richter, A., and Wagner, T., **Diffuser Plate Spectral Structures and their Influence on GOME Slant Columns,** Technical Note, Institut für Umweltphysik Univ.Bremen and Institut für Umweltphysik Univ. Heidelberg, 2010.

Richter, A., Begoin, M., Hilboll, A., Burrows, J. P., **Improvements in GOME-2 retrievals of NO2,** ***Proceedings of the 2nd EPS/Metop*** *RAO Workshop,* 2009.

Rieke, G. H., **Light,** retrieved March 2013, from what are the key aspects of electromagneticradiation:http://ircamera.as.arizona.edu/NatSci102/NatSci102/lectures/light.htm, 2010.

Robinson, D. K., and Bevington. P.R., **Data Reduction and Error Analysis**, *chapter no 1,2, and 3* (pp. 1-46), New York: Published by McGraw-Hill, 2003.

Rottman, G. J., T. N. Woods, and T. P. Sparn., **Solar-Stellar Irradiance Comparison Experiments 1, 1. Instrument design and operation,** *J. Geophys. Res., 98,* 10667, 1993.

Schmitt, M, S., and Dieter, S., **Theoretical Models of Solar Magnetic Variabilty**, In J. M. Fox, *Solar Variabilty and Its Effects on Climate* (pp. 33-45). Washington: American Gepphysical Union, 2004.

Skumanich. A., Lemaire. P., **Magnesium II Doublet Profiles of Chromospheric Inhomogeneities at the Center of the Solar Disk,** *Astron. & Astrophys 22* , pp. 61-68, 1973.

Skupin, J., Noe¨l, S., Wuttke, M., Weber, M., Bovensmann, H., Burrows, J.P., ,Hoogeveen, R., Kleipool, Q., Lichtenberg, G., (2003). **In-flight calibrationof the SCIAMACHY solar irradiance spectrum.** *Adv. Space Res.32 (11),* 2129–2134, 2003.

Slijkhuis,S., **GOME instrument properties affecting the calibration of radiance and polarisation,** in GOME Geophysical Validation Campaign, ESA W PP-108,1996.

Slijkhuis, S., Wahl, S., Aberle, B., Loyola, D., **Re-analysis of GOME/ERS-2 Diffuser properties,** Proc. Envisat & ERS Symp. Salzburg, ESA SP-572, 2P03-25, 2004.

Stephen, L., retrieved August 27, 2013, from: http://www.chem1.com/acad/webtext/pre/mm2.html, 2013.

Tapia, A. O., **THE PLASMA UNIVERSE**, retrieved December 12, 2012, from Astrophysics Plasma Universe: http://www.aldebaran.cz/astrofyzika/plazma/index_en.html, 2005.

Thomson, H.J., Thomson **Higher Education,** retrieved August 28, 2013, from: http://www2.fiu.edu/~cai/index_files/CHAPTER%205%20-%20SIGNAL%20TO%20NOISE.ppt, 2013.

Viereck, R.A., Floyd, L.E., Crane,P.C., Woods, T.N., Knapp, B.G., Rottman, G., Weber, M., Puga, L.C., and DeLand, M.T., **A composite Mg II index spanning from 1978 to 2003**, Space Weather, 2, S10005, doi:10.1029/2004SW000084, 2004.

Watts, A., **WUWT,** retrieved March 1, 2013 , from NASA June 2012 Solar Cycle 24 Prediction: from http://wattsupwiththat.com/2012/06/08/nasa-june-2012-solar-cycle-24-prediction/ , 2012.

Weber, M., Burrows, J.P., and Cebula, R. P.. : **GOME solar UV/vis irradiance measurements between 1995 and 1997—First results on proxy solar activity studies**. *Sol. Phys.,***177,** 63–77, 1998.

Weber, M.,Lamsal, L.N., and Burrows, J.P., **Improved SCIAMACHY WFDOAS total ozone retrieval: Steps towards homogenising long-term total ozone datasets from GOME, SCIAMACHY, and GOME2,** *Proc. 'Envisat Symposium 2007', Montreux, Switzerland, 23-27 April 2007, ESA SP-636*, 2007.

Weber, M., Pagaran, J., Dikty. S., Savigny, C., Burrows, J.P., DeLand, M., Floyd, L. E., Harder, J. W., Mlynczak, M. G., Schmidt, H. ., **Investigation of solar irradiance variations and their impact on middle atmospheric ozone,** retrieved March 5, 2013, from IUP Bremen, from http://www.iup.unibremen.de/UVSAT_material/papers/2012/weber_chap03_cawsesbook_v3.pdf , 2013.

Weber, M., retrieved March 14, 2013, from **UVSAT Group**: from http://www.iup.uni-bremen.de/UVSAT/research/solarradiation, 2013.

Weber, M., **Solar Activity During Solar Cycle 23 Monitered by GOME,** ESAMS, Nordwijk pp. 18-22, 1999.

Woods, T. N., Rottman, G. J., and Ucker G., **SolarStellar Irradiance Comparison Experiments 1, 2. Instrument calibration,** *J. Geophys. Res., 98, 10679,* 1993.

World Meteorological Organization, **WMO report**, 1999.

Woods, T. N., **Validation of the UARS solar ultraviolet irradiances Comparison with ATLAS I and 2 measurements***, J. Geophys. Res., 101,* 9541, 1993.

Zabludoff, A., **Nuclear Reactions in the Sun,**retrieved January 2013, 26, from University of Arizona: http://atropos.as.arizona.edu/aiz/teaching/a250/pp.html, 2011.

Zell, H., **Nasa center and headquarters,** retrieved Feburary 4, 2013, from Sun-earth mission: from http://www.nasa.gov/mission_pages/sunearth/multimedia/solar-rotation.html, 2012.

Declaration

Herewith I declare that I wrote my Master Thesis without external support and that I did not use other than quoted sources and auxiliary means.

All statements which are literally or analogously taken from other publications have been identified as quotations.

After having handed in my Master Thesis, I am not allowed to make any modifications.

Bremen, November 17, 2013 ___________________________

Signature